Ph. D. Thesis

Spin Hall Effect Magnetic Field Sensor

22D18174

LIU MIN

Supervisor: Professor Pham Nam Hai

Department of Electrical and Electronic Engineering

Institute of Science Tokyo

Thesis Defense Committee:

Professor Pham Nam Hai (Chair)

Professor Shigeki Nakagawa

Professor Takaaki Manaka

Professor Akira Yamada

Professor Shinobu Ohya

Associate Professor Shinsuke Miyajima

Abstract

Magnetic field sensors are essential for advanced data storage, navigation, and industrial applications. Conventional GMR and TMR sensors face performance bottlenecks, whereas the recently proposed spin Hall sensors based on topological insulators offer better scalability. This dissertation investigates the direct spin Hall (DSH) magnetic field sensors and discuss their noise mechanisms in BiSb/CoFe heterostructures to guide the design of spin Hall magnetic field sensors.

Chapter 1 outlines the evolution of magnetic recording, the growing demand for advanced magnetic sensors in HDD, and the fundamentals of spintronics. The motivations and objectives of this research were also explained.

Chapter 2 details the thin-film fabrication, structural characterization, and electrical measurement systems that enable proof-of-concept DSH magnetic field sensors.

Chapter 3 focuses on experimental demonstration of DSH magnetic field sensors. By comparing second harmonic Hall, DSH, and ISH measurements, the spin Hall angle was extracted and cross-validated. The noise mechanisms in DSH magnetic field sensors were discussed.

Chapter 4 analyzes the difference between spin Hall angles measured by different methods, including spin accumulation (SA), spin-orbit torque (SOT), and spin Hall magnetoresistance (SMR), revealing the physical origin and meaning of the effective spin Hall angles measured by those methods.

This work establishes a systematic framework for understanding and optimizing spin Hall magnetic field sensors for HDD. Furthermore, the obtained insights on the methodologies of spin Hall angle measurements are useful for development of SOT-MRAM, spin Hall oscillators, and other spin Hall-based neuromorphic spintronic devices.

List of abbreviations

HDDs	hard disk drives
GMR	giant magnetoresistance
TMR	tunnel magnetoresistance
MTJ	magnetic tunnel junction
MgO	magnesium oxide
HAMR	heat-assisted magnetic recording
MAMR	microwave-assisted magnetic recording
PMR	perpendicular magnetic recording
BPM	bit-patterned media
SHE	spin Hall effect
ISHE	inverse spin Hall effect
TI	topological insulator
FM	ferromagnet
SA	spin accumulation
SOT	spin–orbit torque
SMR	spin Hall magnetoresistance
Cu	copper
NiO	nickel oxide
AHE	anomalous Hall effect
AC	alternating current
NM	non-magnetic metal
PHE	planar Hall effect
ANE	anomalous Nernst effect

FLT	Field-like torque
DLT	Damping-like torque
FMR	ferromagnetic resonance
SOC	spin–orbit coupling
QHE	quantum Hall effect
SHA	spin Hall angle
MBE	molecular beam epitaxy
MOKE	magneto-optical Kerr effect
YIG	yttrium iron garnet
TRS	time-reversal symmetry
STT	spin-transfer torque
MRAM	magnetoresistive random access memory
PVD	physical vapor deposition
XRR	X-ray reflectivity
XRD	X-ray diffraction
XRF	X-ray fluorescence
AFM	atomic force microscopy
AMR	anisotropic magnetoresistance
MR	magnetoresistance
DSH	direct spin Hall
MESO	magnetoelectric spin‐orbit
RMS	root-mean-square
ONE	ordinary Nernst effect
SSE	spin Seebeck effect

PMA	perpendicular magnetic anisotropy
SNR	signal-to-noise ratio
DFL	dual-free-layer
ST-FMR	spin-torque ferromagnetic resonance
SHT	spin Hall effect tunneling spectroscopy
WAL	weak antilocalization
LSV	lateral spin valve
IL	interlayer

List of symbols

$\hbar$	Dirac constant
ρ	resistivity
ρ_{yx}	Hall resistivity
V_H	Hall voltage
J_x	current density
σ_{xx}	longitudinal conductivity
R_{xx}	longitudinal resistance
ω_c	cyclotron frequency
σ_{xy}	Hall conductivity
τ	lifetime
τ_r	relaxation time
R_s	anomalous Hall coefficient
M	magnetization
H_{SOI}	spin-orbit interaction
H_E	transverse electric field
P	spin polarization
μ_s	the interfacial spin accumulation vector
ε_{nk}	energy of Bloch states for H_0
$\triangle$	averaged value of interband energy separation
$A_n(R)$	Berry connection
$B_n(R)$	Berry curvature
σ_{xy}^{A}	anomalous Hall conductivity
$f[\varepsilon_n(k)]$	Fermi-Dirac distribution function

λ_{SO}	spin–orbit coupling constant
k	wave number of electron
J_s	spin current density
J_c	charge current density
$\hat{\sigma}$	spin polarization direction
$\rho_{\parallel}$	resistivities when the current is parallel to the magnetization
$\rho_{\perp}$	resistivities when the current is perpendicular to the magnetization
H_{ex}	effective exchange field
L	orbital angular momentum operator
S	spin angular momentum operator
G_r	real part of the spin mixing conductance
M_s	saturation magnetization
e	elementary charge
R_0	the resistance when $M \parallel J_e$
ΔR	SMR amplitude
R_y^{XX}	resistances (the magnetization is oriented along the y-axis)
R_z^{XX}	resistances (the magnetization is oriented along z-axis)
λ_N	spin diffusion length of the heavy metal
ρ_N	the resistivities of the NM layer
ρ_F	the resistivities of the FM layer
t_N	the thicknesses of the NM layer
t_F	the thicknesses of the FM layer
θ_{SH}	spin Hall angle
θ_{SH}^{eff}	effective spin Hall angle

R_{xy}^{ω}	first harmonic resistance
$R_{H}^{2\omega}$	second harmonic resistance
V_{H}^{ω}	the first harmonic component
$V_{H}^{2\omega}$	the second harmonic component
n	an integer (order of diffraction)
λ_l	the X-ray wavelength
d	the spacing between crystallographic planes
θ_B	the angle of incidence (Bragg angle)
H_z	external magnetic fields along the z directions
H_y	external magnetic fields along the y directions
H_x	external magnetic fields along the x directions
V_{xx}	longitudinal voltage
V_{xy}	transverse Hall voltage
w_H	Hall bar has a width
R_{AHE}	anomalous Hall resistance
H_k	effective magnetic anisotropy field
$\widehat{\lambda_R}$	a quantity proportional to the Rashba SOC
R_{BiSb}^{sheet}	sheet resistance
I_{BiSb}	the current flowing into the BiSb layer
σ_{BiSb}	conductivity of the BiSb layer
R_{DSH}	DSH resistance
I_{DC}	DC current
V_{DSH}	DSH output voltage
R_{ISH}	ISH resistance

t_s	the thickness of the surface conduction layer
λ_{sf}	the spin diffusion length of BiSb
w	the width of the pillar
R_S^{Top}	the resistances of the top surface
R_B	the resistances of the bulk
R_S^{Bottom}	the resistances of the bottom surface states
V_n	Johnson - Nyquist noise
k_B	the Boltzmann constant
T	the absolute temperature
R	the sensor resistance
Δf	the measurement bandwidth
N_{th}	thermal noise
N_{mag}	magnetic noise
V_{vol}	the volume of the sensing layer
H_{stiff}	the stiffness field
t_{st}	the spin Hall layer thickness
I_{bias}	increase bias current
R_{pillar}	the pillar resistance
f	the measurement bandwidth
N_{mag}	the magnetic noise
θ_{SH}^{SOT}	spin Hall angle measured by second harmonic
θ_{SH}^{SA}	spin Hall angle measured by spin accumulation
θ_{SH}^{SMR}	spin Hall angle measured by spin Hall magnetoresistance
V_{SA}	spin accumulation voltage

$\triangle R_{xx}(yz)$ resistance measured under magnetic-field rotation in the yz-plane (SMR-dominant)

$\triangle R_{xx}(xz)$ resistance measured under magnetic-field rotation in the xz-plane (AMR dominant)

$\triangle R_{xx}(xy)$ resistance measured under magnetic-field rotation in the xy-plane (SMR dominant)

ρ_{BiSb} the resistivity of the BiSb layer

t_{BiSb} the thickness of the BiSb layer

ρ_{other} the resistivityof the other layers

t_{other} the thickness of the other layers

g_R the transverse spin absorption factors

g_F the longitudinal spin absorption factors

ξ the current shunting factor

T_{IST} the interlayer spin transparency.

τ_t the spin transport time

τ_{mix} spin mixing time

$g_{mix}^{\uparrow\downarrow}$ the mixing conductance at the interface

G_r the real parts of the interfacial spin-mixing conductance

G_i the imaginary parts of the interfacial spin-mixing conductance

λ_s^{IL} spin-diffusion length for interlayer

T_{int} spin transparency at the interlayer

Table of Contents

Chapter 1 Introduction

This chapter outlines the background and motivation of this thesis. It reviews the development of magnetic recording and the fundamentals of spintronics, introduces the topological insulator (TI)/ferromagnetic (FM) heterostructure platform, and discusses applications and prospects of spintronic devices. The chapter concludes with the research objectives and scope of this thesis.

1.1. Background and Significance

1.1.1. Evolution of High-Density Magnetic Recording

Hard disk drives (HDDs) have long been fundamental to digital storage, offering high capacity, cost efficiency, and reliable non-volatile storage. Information is written onto the spinning magnetic disks by the write head and read out with a magnetoresistive read head.[1-5] As illustrated in Fig. 1.1(a), writing employs an inductive write head: a current in the coil generates a localized magnetic field at the write pole, switching the magnetization of the medium. Reading in modern drives uses magnetoresistive sensors—giant magnetoresistance (GMR)[6,7] or tunneling magnetoresistance (TMR)[8] heads—which transduce local magnetization into resistance changes under bias. Because the heads can be repositioned quickly between tracks, HDDs provide random access, enabling efficient retrieval of data in arbitrary order.

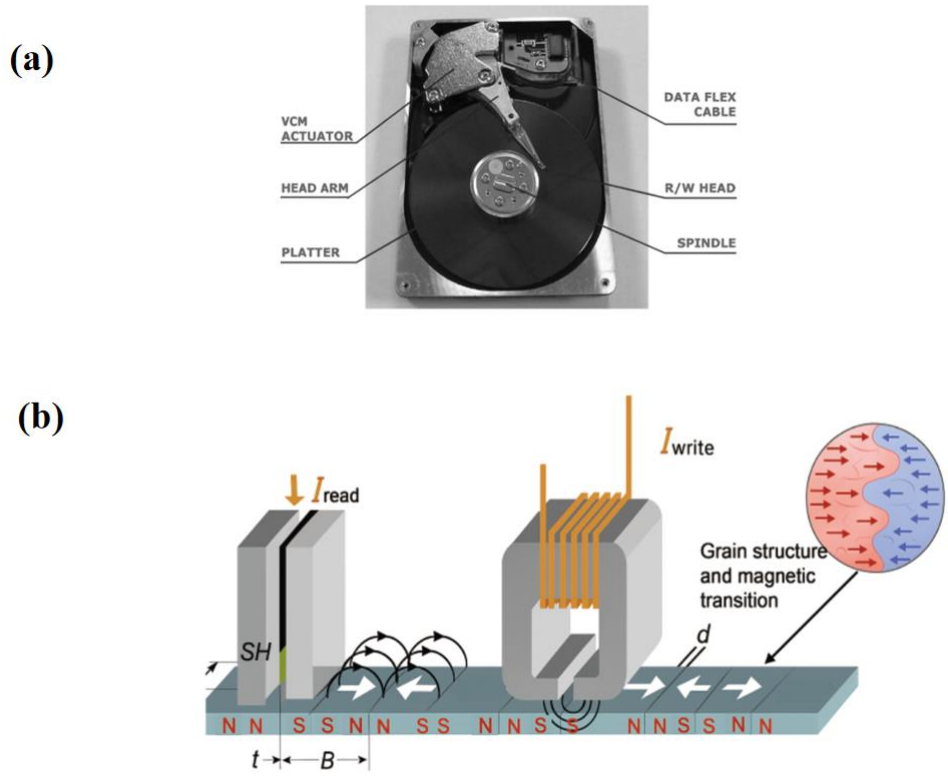

Figure 1.1. Typical structure and working principle of a HDD. (a) Key components, including the rotating platter and the read/write head. Reproduced from Ref. 4 with permission with permission from MRS Bull. (b) Schematic of data recording and reading based on magnetic domain writing and detection. Reproduced from Ref. 5 with permission from IEEE.

The history of HDDs began in 1956 with IBM's 305 RAMAC, which stored about 5 MB using aluminum platters and longitudinal magnetic recording. Since then, steady improvements in four key areas—media, read/write heads, servo positioning, and signal processing—have greatly increased storage capacity. Important milestones include the move to perpendicular magnetic media, the reduction of head flying height to the nanometer scale, the introduction of precise embedded-servo control, and the use of advanced read channels with strong error correction. A major breakthrough occurred in the 1990s with the GMR read head, as illustrated in Fig. 1.2, where the resistance of a multilayer structure depends on the relative orientation of magnetic layers, enabling much higher sensitivity and density.[3] The resulting improvement in readout sensitivity and signal-to-noise ratio (SNR) enabled further miniaturization of the reader and sustained scaling of HDD technology.

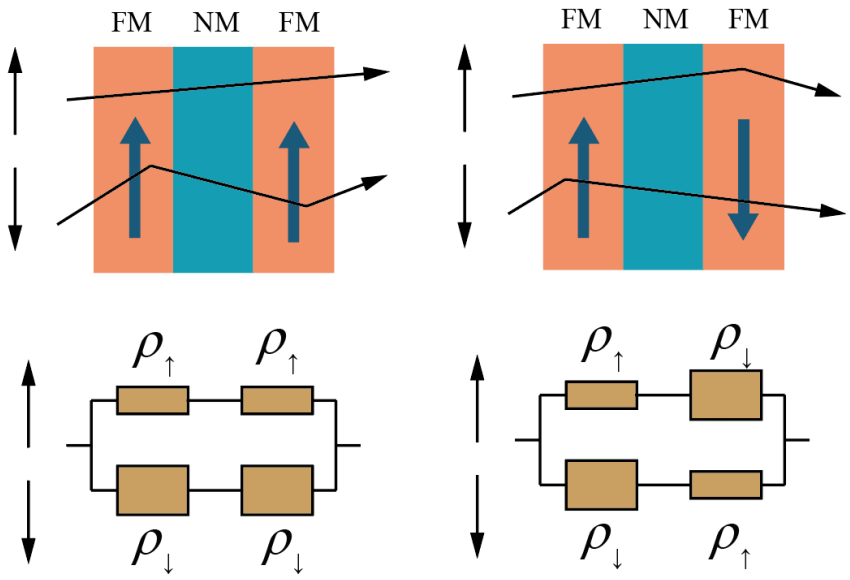

Figure 1.2. Schematic illustration of the GMR effect in a spin valve structure with parallel and antiparallel magnetization configurations. $\rho_\downarrow, \rho_\uparrow$: resistivity of ↑ and ↓ channel. Reproduced from Ref. 6 with permission from Elsevier.

In the early 2000s, TMR replaced GMR as the dominant readout mechanism in HDD technology. TMR devices are based on magnetic tunnel junctions (MTJ), which consist of two ferromagnetic layers separated by an ultrathin insulating barrier, typically magnesium oxide (MgO).[8] Electrons tunnel across the barrier via quantum tunneling, with the tunneling probability being strongly dependent on the relative alignment of the magnetizations in the two ferromagnetic layers. As illustrated in Fig. 1.3, the resistance is low when the magnetizations are parallel and high when they are antiparallel. This leads to a significantly higher magnetoresistance ratio compared to GMR, as well as improved thermal stability and better scalability. The adoption of TMR has played a crucial role in enabling the continued downscaling of read head dimensions while maintaining high sensitivity and reliability.

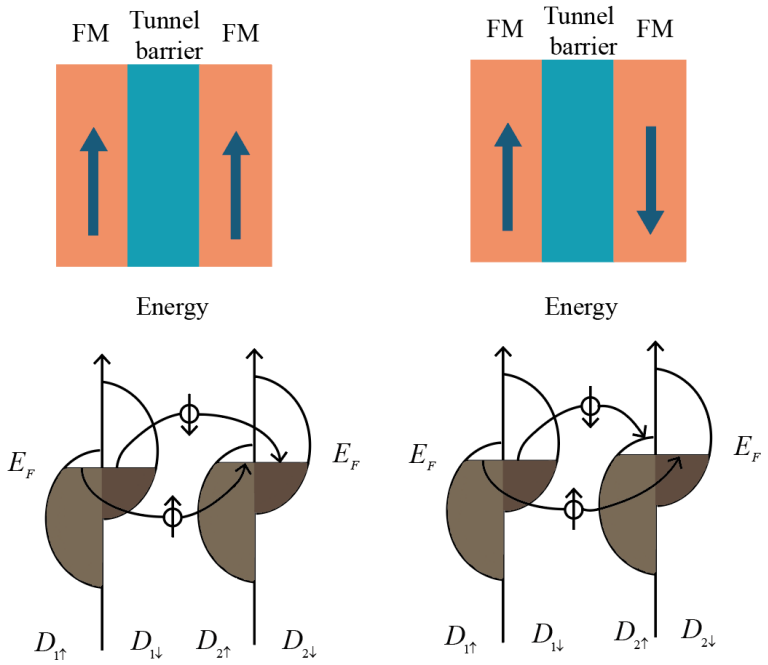

Fig. 1.3. Schematic illustration of the TMR effect in a MTJ. (a) In the parallel configuration, the density of states allows efficient tunneling for majority spins, resulting in low resistance. (b) In the antiparallel configuration, tunneling is suppressed due to spin mismatch, leading to high resistance. E_F: Fermi energy; $D_\uparrow/D_\downarrow$: spin-resolved density of states. Reproduced from Ref. 6 with permission from Elsevier.

As recording density approached and exceeded 1 Tb/in², several fundamental physical limitations began to emerge, including the superparamagnetic effect—where thermal fluctuations destabilize nanoscale magnetic bits—thermal instability of the recording medium, and limited signal-to-noise ratio (SNR) and spatial resolution of conventional read heads.[9] To overcome these challenges, next-generation recording paradigms such as heat-assisted magnetic recording (HAMR) and microwave-assisted magnetic recording (MAMR) have been proposed. HAMR employs localized laser heating to temporarily reduce the coercivity of the medium, thereby facilitating magnetization switching.[10] In contrast, MAMR utilizes high-frequency magnetic fields—often generated by spintronic nano-oscillators—to assist the writing process. These emerging technologies impose increasingly stringent requirements on magnetic sensors, including higher spatial resolution, faster dynamic response, and improved compatibility with nanoscale device architectures.[11]

A compact historical summary of these technological transitions is provided in Table 1.1. Data compiled from Refs. 9–16.

Period	Technology	Key Advancement	Read-Head Type	Areal Density
1956	IBM 305 RAMAC	First commercial HDD; longitudinal magnetic recording (LMR)	Inductive	~2 Kb/in^2
1970s–1980s	Longitudinal Recording	Thin-film heads and media; lower flying height	Thin-Film Inductive	10–100 Mb/in^2
1990s	GMR Spin-Valve	High sensitivity; improved SNR	GMR	>1 Gb/in^2
~2005	PMR (Perpendicular Magnetic Recording)	Transition from LMR to PMR; granular media	GMR → TMR	>100 Gb/in^2
2007–2010	TMR (MTJ) Readers	Higher MR ratio; continuous scaling	TMR	~300–500 Gb/in^2
2010–onward	HAMR/MAMR	Heat- or microwave-assisted recording; high-anisotropy media	TMR + NFT/STO	≥1–2 Tb/in^2
Future (Research)	BPM (Bit-Patterned Media)	Patterned islands; noise suppression	TMR + Spintronics	multi-Tb/in^2 (theoretical)

1.1.2. Increasing Demands for Magnetic Field Sensors

As discussed in the previous section, the evolution of HDD technologies is increasingly constrained by fundamental physical limits, particularly in the performance of magnetic sensors used for data readout. These limits primarily arise from thermal stability issues at ultrahigh recording densities and the limited sensitivity and spatial resolution of conventional read heads. To

overcome these limitations and support the demands of next-generation storage and sensing systems, the development of more advanced magnetic field sensors has become essential.

The continuous evolution of HDD technology has been strongly driven by advances in magnetic sensor performance. Traditional inductive read heads have been largely superseded by spintronic-based sensors—most notably GMR and TMR devices—which achieve markedly higher readout sensitivity by exploiting spin-dependent transport. These innovations have enabled successive increases in areal density by offering larger magnetoresistive ratios and improved signal-to-noise characteristics.

Beyond storage applications, emerging fields such as automotive electronics, biomedical diagnostics, and spintronic logic similarly necessitate compact, energy-efficient, and interference-resilient magnetic sensors. Addressing these converging requirements calls for the exploration of novel materials and device architectures capable of reliable and efficient operation at the nanoscale.

In response to these evolving requirements, spin-orbit-interaction-based sensing mechanisms have emerged as a promising direction in magnetic sensor development. In particular, devices utilizing the spin Hall effect (SHE) and inverse spin Hall effect (ISHE) offer several key advantages: they enable all-electrical detection of spin information without the need for magnetic reference layers, and they offer better scalability compared to conventional GMR or TMR sensors. These characteristics make SHE-and ISHE-based sensors highly attractive not only for next-generation high-density data storage but also for a broad spectrum of emerging spintronic and sensing applications requiring compact, scalable, and energy-efficient solutions.

1.1.3. Research Motivation

The development of magnetic sensors for next generation recording technologies requires high sensitivity, fast response, and compatibility with nanoscale device architectures. Conventional spin Hall materials, such as platinum (Pt), tantalum (Ta) and tungsten (W), exhibit limited spin–charge conversion efficiency and weak signal output under ambient and low-current conditions[17], restricting their applicability in HDDs.

To address these limitations, our first study employed a topological insulator (TI) as a spin current source in magnetic sensing devices. By integrating a TI layer with a FM, we realized a

TI/FM bilayer sensor that exhibited spin Hall and inverse spin Hall resistance signals more than 100 times larger than those of conventional heavy metals at room temperature. This demonstrated the potential of TI-based spintronic sensors for practical HDD applications.

Our second study shifted focus to the fundamental studies of spin Hall effect evaluation methods. Using spin accumulation (SA)[18], spin–orbit torque (SOT)[19], and spin Hall magnetoresistance (SMR)[20], we systematically examined SHE signal magnitudes and temperature dependences. We found that SA yielded a larger effective spin Hall angle with stronger temperature dependence, while SOT and SMR gave smaller values with weaker trends. These findings highlight the role of interfacial spin transmission and reflection in TI/FM heterostructures and confirm that SA is a useful method for evaluating the intrinsic spin Hall angle.

1.2. Fundamentals of Spintronics and Spin-Dependent Transport Phenomena

1.2.1. Spin Currents and Their Control Mechanisms

Just as the directional movement of electric charge gives rise to charge current, the directional flow of spin angular momentum constitutes a spin current. Spin, an intrinsic form of angular momentum carried by electrons, can be described in terms of two quantum states—spin-up and spin-down—commonly denoted as "↑" or "+" and "↓" or "−", respectively. In ferromagnetic metals, these states are typically defined with respect to the direction of the local magnetization: spin-up (↑) refers to carriers (typically electrons) with spins aligned parallel to the magnetization, while spin-down (↓) indicates antiparallel alignment. This also corresponds to majority and minority spin populations, respectively[18,21]. In semiconductors and optical systems, spin states are often defined with respect to the light propagation direction or an externally applied magnetic field, typically aligned along the z-axis[22]. For example, circularly polarized light can selectively excite spin-polarized carriers depending on its helicity.

In spintronics, spin information is transmitted predominantly in the form of spin currents. These can be classified into two main types:

(1) Spin-polarized charge current, where a net electric current also carries an imbalance in spin population (i.e., both charge and spin currents are non-zero); and

(2) Pure spin current, where equal numbers of spin-up and spin-down electrons flow in opposite

directions, resulting in zero net charge current but a finite spin current. These two types are schematically illustrated in Fig. 1.4.

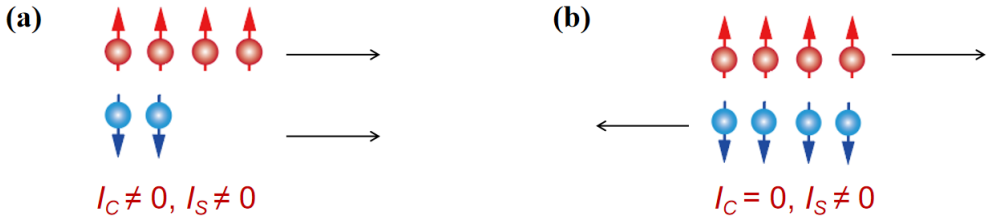

Figure 1.4. Conceptual illustration of spin current types. (a) Spin-polarized charge current, where spin-up and spin-down electrons flow in the same direction. (b) Pure spin current, where spin-up and spin-down electrons propagate in opposite directions.

Spin currents can be generated, modulated, and detected through a variety of mechanisms, each governed by distinct physical parameters. Understanding and controlling these factors is crucial for the effective implementation of spintronic devices.

(1) Generation: Material-dependent Charge-to-Spin conservation Efficiency

The efficiency of spin current generation is strongly determined by the intrinsic properties of the material, most notably its spin-orbit coupling strength. Materials such as Pt, W, and topological insulators (e.g., bismuth antimony (BiSb)) exhibit large spin Hall angles, thereby enabling highly efficient spin current generation through the spin Hall effect.[23-25] In magnetic heterostructures, the quality of the interface also plays a crucial role: well-engineered interfaces facilitate efficient spin transfer by minimizing spin loss and maximizing interfacial spin transparency.[26,27]

(2) Modulation: Structural and Magnetic Control of Spin Currents

Once generated, spin currents can be effectively modulated by a variety of structural and magnetic parameters. Structurally, device configuration, including the choice of spacer or interfacial layers, interface roughness, crystalline orientation, and interlayer thickness plays a decisive role in determining spin transport properties. [28-31] These structural factors influence key spin transport parameters such as spin diffusion length, spin dephasing, and interfacial transparency. Interface roughness introduces additional spin scattering and reduces spin coherence, thereby shortening effective spin diffusion lengths. The choice of interlayer materials modifies spin resistance and may induce spin filtering or spin loss depending on their electronic and magnetic properties. Crystalline orientation affects band structure

matching and spin-orbit coupling symmetry, while layer thickness determines the extent of spin relaxation due to spin-flip scattering. Careful engineering of these parameters is essential to minimize spin loss and to maximize spin injection and detection efficiency in multilayer spintronic devices.

For instance, the insertion of copper (Cu), MgO, or nickel oxide (NiO) interlayers can either enhance or suppress interfacial spin transparency, depending on their thickness and interfacial quality.[32,33] Similarly, reducing interface roughness and controlling crystalline orientation help suppress spin scattering and improve spin injection efficiency. The thickness of nonmagnetic layers is particularly critical: thinner layers help preserve spin coherence, whereas thicker ones introduce additional spin relaxation and diminish the transmitted spin signal.

From the magnetic perspective, the direction of spin polarization generated via the spin Hall effect is intrinsically determined by the direction of the applied charge current, enabling electrical steering of spin current flow. Moreover, the orientation of the magnetization vector in the ferromagnetic layer tunable via an external magnetic field-affects the relative alignment between spin polarization and magnetization. Although the external magnetic field does not affect the magnitude of spin current generation, it plays a crucial role in determining the efficiency of spin absorption at the interface. This spin-magnetization interaction governs the magnitude and angular dependence of spintronic phenomena such as SOT and SMR.

(3) Detection: Spin Signal Preservation and Measurement Optimization

Effective spin current detection relies on the preservation of spin information over sufficiently long spatial and temporal scales. Environmental factors, particularly temperature, have a direct impact on spin diffusion lengths.[34,35] Lower temperatures typically extend spin lifetimes and diffusion distances, thereby improving the detectability of spin signals in experimental measurements. Minimizing structural defects and impurities within the spin transport channel suppresses spin relaxation and dephasing, resulting in more robust and reproducible measurements.[36]

Through the combined optimization of material selection, device geometry, external fields, interlayer engineering, and environmental control, the generation, modulation, and detection of spin currents can be finely tuned paving the way toward efficient and scalable spintronic functionalities.

1.2.2. Anomalous Hall effect

With the discovery and theoretical research on the quantum Hall effect, the mathematical concept of topology began to merge with solid-state physics, giving rise to the emergence of a non-trivial topological quantity called the Berry phase, a gauge-invariant quantity within the topological space. Subsequently, many novel transport phenomena and materials were discovered using theoretical models based on this topological concept. Examples include topological insulators, topological superconductors, and magnetic skyrmions with nontrivial topological-spin structures. Additionally, models employing this topological concept have explained previously poorly explained phenomena, with the most representative being the intrinsic Anomalous Hall effect (AHE) in ferromagnets. Including the scattering-induced extrinsic mechanism, the AHE is one of the most powerful methods for investigating the magnetic and electronic transport properties of ferromagnetic metals. Furthermore, they offer advantages for potential spintronic applications.

In this section, we will introduce the basic knowledge related to AHE. First, we will introduce the ordinary Hall effect. Then, we will present the three mechanisms of the AHE, with a particular focus on the intrinsic AHE, which is associated with the topological properties of band structures.

Ordinary Hall effect

The Hall effect, as one of the most fundamental phenomena in solid-state physics, has not only helped researchers explore the transport properties of materials but also contributed significantly to various applications, such as the Hall sensor used for measuring magnetic field strength.

The Hall effect occurs when a current is applied in the x-direction of a metal (or semiconductor), and a magnetic field is applied in the z-direction. This causes the electrons, which would originally move longitudinally, to experience a lateral deviation due to the Lorentz force ($F = qv \times B$), resulting in the generation of a transverse electric field.[37] The relationship between the electric field vector and the current density vector in the Hall effect is as follows:

$$\begin{bmatrix} E_x \\ E_y \\ E_z \end{bmatrix} = \begin{bmatrix} \rho_{xx} & \rho_{xy} & \rho_{xz} \\ \rho_{yx} & \rho_{yy} & \rho_{yz} \\ \rho_{zx} & \rho_{zy} & \rho_{zz} \end{bmatrix} \begin{bmatrix} J_x \\ J_y \\ J_z \end{bmatrix} \tag{1.1}$$

Where ρ is the resistivity. In the steady state, there is no current in the y-direction or x-direction, and no voltage is generated in the z-direction, so the Hall electric field is:

$$E_y = \rho_{yx} J_x \tag{1.2}$$

Where ρ_{yx} is the Hall resistivity, and can be expressed as:

$$\rho_{yx} = \frac{E_y}{J_x} = \frac{V_H / W}{I_x / Wt} = \frac{V_H}{I_x} t \tag{1.3}$$

V_H is the Hall voltage, W is the length of the sample in the y-direction, and t is the thickness of the sample. Through the Hall resistance, physical quantities such as carrier density can be obtained. In the steady state, the Lorentz force experienced by carriers equals the Coulomb force under the Hall electric field:

$$qE_y = qv_x \times B_z \tag{1.4}$$

Substituting the expression for current density $J_x = nqv_x$ into Equation (1.3), one can obtain the relation between the Hall resistivity and the ordinary Hall coefficient R_H:

$$\rho_{yx} = \frac{E_y}{J_x} = \frac{v_x B_z}{nqv_x} = \frac{B_z}{nq} = R_H B_z \tag{1.5}$$

where n is carrier density. By measuring the Hall resistivity dependence of magnetic field, the sign of R_H and the carrier density can be determined. $R_H > 0$ indicates that the carriers are holes, while $R_H < 0$ indicates that the carriers are electrons. Once the carrier density is known, carrier mobility μ also can be calculated using the measured longitudinal conductivity σ_{xx} and the Drude formula $\sigma_{xx} = n|q|\mu$.

On the other hand, by solving the semiclassical electron motion equations, the relationship between electric field and current can be obtained as follows[37]:

$$\begin{pmatrix} j_x \\ j_y \end{pmatrix} = \frac{ne^2}{m^*} \begin{pmatrix} \frac{\tau}{1+(\omega_c\tau)^2} & \frac{\omega_c\tau^2}{1+(\omega_c\tau)^2} \\ \frac{-\omega_c\tau^2}{1+(\omega_c\tau)^2} & \frac{\tau}{1+(\omega_c\tau)^2} \end{pmatrix} \begin{pmatrix} E_x \\ E_y \end{pmatrix} = \begin{pmatrix} \sigma_{xx} & \sigma_{xy} \\ \sigma_{yx} & \sigma_{yy} \end{pmatrix} \begin{pmatrix} E_x \\ E_y \end{pmatrix} \tag{1.6}$$

where ω_c is the cyclotron frequency. From this formula, we can draw an important conclusion, which is that the Hall conductivity σ_{xy} is proportional to the square of the lifetime τ, while the longitudinal conductivity σ_{xx} is proportional to the lifetime τ.

Three mechanisms of the AHE

In non-magnetic metals and semiconductors, the Lorentz force induces a transverse voltage, resulting in a normal Hall resistance. In magnetic conductors, the spin-orbit interaction gives rise to an anomalous Hall resistance proportional to magnetization. The total Hall resistivity ρ_{yx} can be expressed as[38]:

$$\rho_{yx} = R_H B + 4\pi R_s M \tag{1.7}$$

where the R_s is anomalous Hall coefficient, M is the magnetization. R_s is the physical quantity that requires the knowledge of quantum mechanics for explanation. The theoretical explanations for R_s mainly fall into two types. One is the explanation of R_s by Karplus and Luttinger (KL theory) using band theory[39], and the other is the explanation of R_s by Kondo using the s-d interaction between conduction

electrons and d-bound state electrons[40]. The KL theory laid a solid foundation for establishing the relationship between Berry phase and AHE. Therefore, the anomalous Hall effect that is directly related to the electronic band structure is referred to as the intrinsic AHE, while the others are classified as extrinsic AHE.

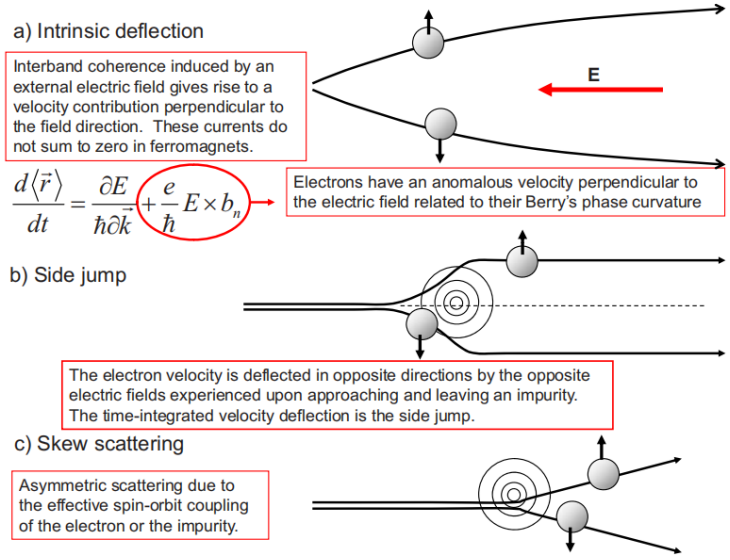

Figure 1.5. Schematic illustration of the three microscopic mechanisms responsible for the spin Hall effect: (a) intrinsic deflection due to Berry curvature, (b) side jump during impurity scattering, and (c) skew scattering arising from spin–orbit coupling. Reproduced from Ref. 38 with permission from APS.

The extrinsic AHE is primarily attributed to the asymmetric scattering of conduction electrons by magnetic impurities. Depending on the scattering mechanism, it can be classified into skew scattering and side-jump mechanisms:

Skew Scattering: This extrinsic mechanism arises from spin-dependent asymmetric scattering of conduction electrons by impurities in the presence of spin orbit coupling (SOC). Spin-up and spin-down electrons are deflected in opposite directions, resulting in a net transverse current. The skew scattering mechanism is characterized by the anomalous Hall coefficient R_s being proportional to the longitudinal resistivity ρ_{xx}.

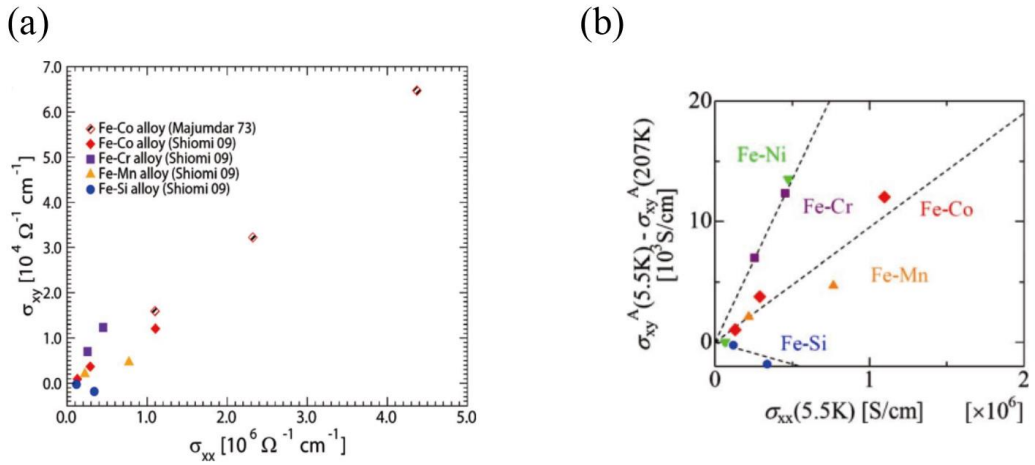

Figure 1.6. (a) and (b) Variation of longitudinal conductivity and Hall conductivity in Fe single crystals after doping with impurity atoms. Reproduced from Ref. 38 with permission from APS.

A specific example, as shown in Fig. 1.6 (a) and (b), is that in single crystals of 3d electron systems such as Fe and Mn, the introduction of impurity atoms leads to a proportional increase in the zero-field Hall conductivity $[\sigma_{xy}^{A}(0T) \approx \frac{R_s M}{\rho_{xx}^2}]$ with the longitudinal conductivity $(\sigma_{xx} = \frac{nq\tau}{m} \approx \frac{\rho_{xx}}{\rho_{xx}^2})$. This indicates that in ultra-clean metallic ferromagnets, the anomalous Hall effect is dominated by skew scattering.[38]

Side Jump: Also, an extrinsic mechanism, side jump arises from a lateral displacement of the electron trajectory during each scattering event. This displacement is independent of the relaxation time τ_r and results from the anomalous velocity acquired due to SOC during the scattering process. Although typically smaller than the skew scattering contribution, the side jump effect can become significant in materials with moderate impurity concentrations and intermediate conductivity. However, in the side-jump mechanism, since the Hall coefficient is independent of the electron scattering time, it is not possible to experimentally determine whether the AHE is dominated by the side-jump mechanism.

KL theory: KL theory assumes that the conduction electrons are the d electrons in ferromagnetic conductors. The total Hamiltonian of the system consists of the kinetic energy term for the d electrons moving in the periodic potential of the crystal, the spin-orbit interaction term H_{SOI}, and the transverse electric field term is written as:

$$H_E = -eE_b x_b \tag{1.8}$$

Upon diagonalizing, the matrix element of H_E can be written as[38,39]:

$$\langle nk|H_E|n'k'\rangle = -eE\left(i\delta_{n,n'}\frac{\partial}{\partial k_b}\delta_{k,k'} + i\delta_{k,k'}J_b^{nn'}(k)\right) \tag{1.9}$$

here (n, k) and (n', k') represent electron state of d band electron. $J_b^{nn'}(k)$ is current density of y direction, can be written as:

$$J_b^{nn'}(k) = \int_\Omega dr u_{n'k}^* \frac{\partial}{\partial k_b} u_{n'k} \tag{1.10}$$

where $u_{nk}^* \left(u_{n'k}\right)$ is the Bloch wave function of the d electrons. The KL theory assumes that the second term on the right-hand side of Equation (1.8) is treated as a perturbation term H_{E}^a and only contributes to the ordinary Hall conductivity, while the first term H_{E}^r, along with H_0 and H_{SOI}, collectively provides the anomalous Hall conductivity. From the first term, the average velocity of the electrons can be obtained:

$$\overline{v_a} = -ie \sum_{n,k} \rho_0' \left(E_{nk}^p\right) J_a^{nn'}(k) \tag{1.11}$$

When the energy of the spin-orbit interaction H_{SOI} is smaller than the Fermi energy and the bandwidth, the average velocity can be written as:

$$\bar{v} = -\frac{e}{m\Delta^2} H_{SOI} \frac{M \times E}{M_{\mathrm{s}}} \sum_{n,k} \rho_0 \left(\varepsilon_{nk}\right) v_{nk} \tag{1.12}$$

where ε_{nk} is the energy of Bloch states for H_0, ρ_0 density matrix (derivative of energy), Δ is the averaged value of interband energy separation, and M_{s} is the magnetization. This velocity is also called the anomalous velocity, which is perpendicular to both the electric field and the magnetization, and disappears in the absence of the spin-orbit interaction. Since the anomalous velocity is perpendicular to the electric field and magnetization, it only has a component in the y-direction. Therefore, the transverse current can be written as:

$$J_{\mathrm{y}} = n_{\mathrm{d}} e \overline{v_{\mathrm{y}}} = r M_{\mathrm{z}} E_{\mathrm{x}} \tag{1.13}$$

The relationship between the anomalous Hall coefficient and the longitudinal resistivity can be obtained:

$$r = -\frac{e}{m\Delta^2} H_{SOI} \frac{n_d}{M_s} \sum_{n,k} \rho_0 \left(\varepsilon_{nk}\right) v_{nk} \tag{1.14}$$

$$R_s = \frac{2e^2 H_{SOI}}{m\Delta^2} \delta \left\langle \frac{m}{m_*} \right\rangle \rho_{xx}^2 \tag{1.15}$$

$$-\sum_{n,k} \rho_0' \left(\varepsilon_{nk}\right) v_{nk} = \delta \left\langle \frac{m}{m_*} \right\rangle \tag{1.16}$$

Finally, it was concluded that R_{s} is proportional to the square of ρ_{xx}, a relationship later confirmed by experiments.

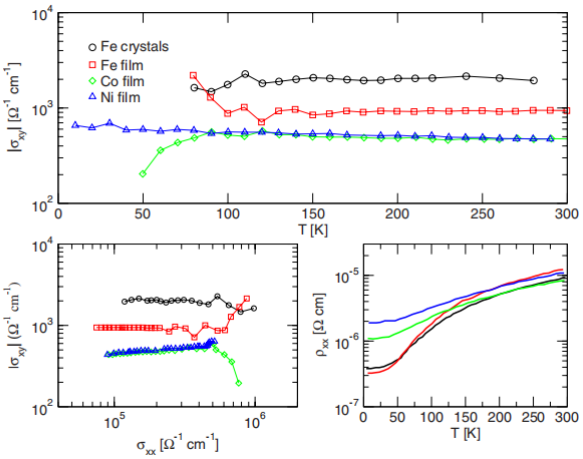

Figure 1.7. (a) and (b) Variation of longitudinal conductivity and Hall conductivity in some 3d metal thin films. Reproduced from Ref. 38 with permission from APS.

Experiments have shown that the intrinsic AHE essentially dominates the AHE in good metals (10^4 S/m < σ_{xx} < 10^6 S/m). For example, as shown in Fig. 1.7, in thin films and alloys of 3d metals, the Hall conductivity $[\sigma_{xy}^{A}(0T) \approx \frac{R_s M}{\rho_{xx}^2} \sim \frac{\rho_{xx}^2 M}{\rho_{xx}^2}]$ is independent of the longitudinal conductivity, indicating that the AHE is dominated by the intrinsic mechanism. The KL theory does not consider the scattering of conduction electrons by impurities; thus, the KL-type AHE is related solely to the band structure of ferromagnetic conductors, representing an intrinsic property of the material. Therefore, it is also referred to as intrinsic AHE.[38]

We have introduced the three mechanisms of the AHE. Regardless of the mechanism, its essence lies in magnetic transport in the presence of spin-orbit interaction. The symmetry underlying magnetic transport effects requires the breaking of time-reversal symmetry, which is also a prerequisite for the occurrence of the AHE. Remarkably, recent studies have revealed that even in materials without ferromagnetism but with broken time-reversal symmetry, such as Mn_3Sn, a large AHE signal has been observed.

Berry phase and Berry curvature: In quantum mechanics, the wave function is written in terms of linear combinations of orthogonal vectors forming a basis set. The abstract space spanned by these orthogonal bases is called Hilbert space. If in a crystal, the wave vector *k* describing the electron's wave function is a good quantum number, then this wave function can also be viewed as a mapping from the wave vector space to a manifold in the Hilbert space. The Berry phase, as an electron-specific gauge

invariant, serves as the link between the momentum space and the parameter space represented by the Hilbert space.[40]

To set a parameter group $R = (R_1(t), R_2(t), \ldots)$ is related to the Hamiltonian of electrons in solid. All $R_n(t)$ as time-dependent parameters are treated as a vector in the parameter space. In an adiabatic process, the time-dependent Schrödinger equation can be written as:

$$H[R(t)]|n,R(t)\rangle = E_n[R(t)]|n,R(t)\rangle \tag{1.17}$$

$$H[R(t)]|n,t\rangle = i\hbar\frac{\partial}{\partial t}|n,t\rangle \tag{1.18}$$

where |n, t > is state, and |n, $R(t)$> is the intrinsic state of system. The state of the system can be written in the following form:

$$|n,t\rangle = \exp\left(\frac{i}{\hbar}\int_0^t dt' L_n[R(t)]\right)|n,R(t)\rangle \tag{1.19}$$

by putting equation (1.18) in Equation (1.15), the Ln [R(t)] can be obtained as:

$$L_n[R(t)] = i\hbar\frac{dR(t)}{dt}\langle n,R(t)|\nabla_R|n,R(t)\rangle - E_n[R(t)] \tag{1.20}$$

In Equation (1.20), it can be noticed that the second term is a trivial term, while the first term is a nontrivial term. During the development process from t = 0 to t = T, if R traces a closed loop C in the parameter space, then the Berry phase along is closed loop C can be defined as:

$$r_n[C] = \int_0^T \frac{dR(t)}{dt}\cdot i\langle n,R(t)|\nabla_R|n,R(t)\rangle dt \tag{1.21}$$

$$r_n[C] = \oint_C dR\cdot i\langle n,R(t)|\nabla_R|n,R(t)\rangle \tag{1.22}$$

$$r_n[C] = -\oint_C dR\cdot A_n(R) \tag{1.23}$$

$$r_n[C] = \int_S dS\cdot B_n(R) \tag{1.24}$$

where $A_n(R)$ and $B_n(R)$ respectively represent the Berry connection and Berry curvature. Can be written as:

$$A_n(R) = -i\langle n,R(t)|\nabla_R|n,R(t)\rangle \tag{1.25}$$

$$B_n(R) = \nabla_R\times A_n(R) \tag{1.26}$$

Here, by replacing the parameter R with the wave vector k in the reciprocal lattice space, we find that the form of the Berry connection is the same as the integrand term in equation (1.9). This is also the origin of the connection between intrinsic anomalous Hall effect and nontrivial topological quantities. Because the KL theory does not consider electron scattering, this current is also a non-dissipative current. When

this current is introduced into the Hall conductivity, the anomalous Hall conductivity σ_{xy}^{A} can be written as[38]:

$$\sigma_{xy}^{A} = -\frac{e^2}{\hbar}\sum_n \int \frac{dk}{(2\pi)^d} f[\varepsilon_n(k)]B_n(k) \tag{1.27}$$

Where $f[\varepsilon_n(k)]$ represents the Fermi-Dirac distribution function. The Berry curvature is also regarded as an imaginary magnetic field in the momentum space, possessing the same symmetric properties as real magnetic field, including inversion symmetry but broken time-reversal symmetry. Therefore, by calculating the time-reversal symmetry in the Berry curvature using the wavevectors from the dispersion relation of electrons in a certain material, one can tell whether this material exhibits the intrinsic anomalous Hall effect or not.

1.2.3. Spin Hall Effect (SHE) and Inverse Spin Hall Effect (ISHE)

The SHE and its reciprocal counterpart, the ISHE, are fundamental phenomena in spintronics that enable the interconversion between charge and spin currents via SOC. These effects not only serve as the primary mechanisms for generating and detecting spin currents but also underpin a wide range of device concepts, including SOT memories, spin Hall nano-oscillators, and spin-based logic circuits.

(1) Physical Origin and Historical Context

The conceptual foundation of the SHE was inspired by the AHE, which arises in ferromagnetic materials due to SOC. In the AHE, when a longitudinal charge current is applied, SOC causes asymmetric scattering of spin-up and spin-down electrons, leading to a transverse voltage. This imbalance results from the unequal populations of majority and minority spins in the ferromagnet.

In contrast, the SHE manifests in nonmagnetic materials with strong SOC. When a longitudinal charge current flows through such a material, spin-up and spin-down electrons are deflected in opposite transverse directions due to spin-dependent scattering, giving rise to a transverse pure spin current-i.e., spin flow without an accompanying net charge current. This leads to spin accumulation with opposite polarizations at the lateral edges of the material, even in the absence of an external magnetic field. This feature makes SHE especially attractive for spintronic applications, as it enables spin current generation without requiring magnetic order.

The SHE was first theoretically proposed by Dyakonov and Perel in 1971 in the context of spin diffusion and spin relaxation. It was reintroduced and formalized under its modern name by Hirsch in

1999, who proposed the concept of spin accumulation at the edges of a conductor. Experimental verification came in 2004, when Kato et al. observed the effect in n-type GaAs using Kerr rotation microscopy, thus initiating a surge of experimental and theoretical research into spin-charge interconversion phenomena.

(2) Microscopic Mechanisms of SHE

The SHE originates from SOC, which facilitates the transverse deflection of spin carriers under the influence of an electric field. Microscopically, the SHE can arise from both intrinsic and extrinsic mechanisms, which are the same as AHE. Here, we mainly focus on the intrinsic SHE.

From a symmetry viewpoint, unlike the AHE, the SHE does not require broken time-reversal symmetry and can therefore occur even in nonmagnetic materials. With respect to spatial inversion symmetry, the SHE can exist both in centrosymmetric and non-centrosymmetric crystals. However, in Rashba-type two-dimensional electron gases, the structural inversion asymmetry along the growth direction is essential for generating the Rashba SOC term. In symmetric quantum wells, this Rashba contribution vanishes and the corresponding Rashba-type SHE disappears. Since the TI/FM heterostructures studied in this thesis inherently break structural inversion symmetry at the interface, the Rashba-type SHE is of particular relevance to the mechanisms discussed here.

In a two-dimensional n-type electron gas (2DEG) formed in a semiconductor heterostructure, the Hamiltonian can be written as:

$$H = \frac{\hbar^2 k^2}{2m} + \widehat{\lambda_R}(\vec{\sigma} \times \vec{k})_z \tag{1.28}$$

$$\vec{k} = (k_x + k_y) \tag{1.29}$$

Where $\widehat{\lambda_R}$ is a quantity proportional to the Rashba SOC, k is wave number of electron. In a heterostructure, due to the structural difference between the upper and lower layers of the thin films, the symmetry along the z-direction is broken [$H(z) \neq H(-z)$]. In this case, electrons are confined within the interface, leading to the appearance of $\widehat{\lambda_R}$. Moreover, the magnitude of SOC can be tuned, for example, by adjusting the gate voltage, thereby controlling the amplitude of the SHE signals. Here, we assume that the current flows along the x-direction. According to linear response theory, the spin current in the y-direction can be expressed as:

$$j_{s,y} = \int_{annulus} \frac{d^2 p}{(2\pi\hbar)^2} \frac{\hbar n_{z,p}}{2} \frac{p_y}{m} = \frac{-eE_x}{16\pi\lambda m}(p_{F+} - p_{F-}) \tag{1.30}$$

where p_{F+} and p_{F-} are the Fermi momenta of the majority and minority spin Rashba bands.[41] Substituting $j_{s,y}$ into the formula $\sigma_{xy}^{H\text{-}in} = -\frac{e}{\hbar} j_{s,y}/E_y$, and then applying the Kubo formula, the spin Hall conductivity can be obtained as:

$$\sigma_{xy}^{H-int} = \frac{e^2}{V}\sum_{k,n\neq n'}\left(f_{n',k} - f_{n,k}\right)\times\frac{\mathrm{Im}\left[\left\langle n'k\middle|\hat{j}_{spinx}^{z}\middle|nk\right\rangle\left\langle nk\middle|v_y\middle|n'k\right\rangle\right]}{\left(E_{nk}-E_{n'k}\right)\left(E_{nk}-E_{n'k}-\hbar\omega-i\eta\right)} \tag{1.31}$$

where n, n' are band indices, $\widehat{j_{spinx}^{z}}$ is the spin current operator, ω and η are set to zero in the dc clean limit, and the velocity operators at each p are given by $\hbar v_i = \hbar\partial H(p)/\partial p_i$. In terms of both mechanism and form, it is similar to the intrinsic AHE.

The effect was first observed in GaAs/AlGaAs semiconductor heterostructures[42] and was later observed in metallic heterostructures in 2008[43]. However, in structures with inversion symmetry, such as some quantum wells, SOC does not arise and no SHE signal is observed.

(3) Spin Hall Angle and Efficiency

The efficiency of charge-to-spin current conversion is characterized by the spin Hall angle θ_{SH}, defined as the ratio of spin current density J_s to charge current density J_c:

$$J_s = \theta_{SH}\frac{\hbar}{2e}(J_c\times\hat{\sigma}) \tag{1.32}$$

Here, $\hat{\sigma}$ denotes the spin polarization direction. $\hbar$ is the reduced Planck constant, and e is the elementary charge (taken as a positive quantity). A large θ_{SH} is desirable for spin current generation and is typically observed in materials with strong SOC, such as Pt, W, and topological insulators (TIs).

(4) Inverse Spin Hall Effect (ISHE)

The ISHE is the reciprocal of the spin Hall effect: when a pure spin current flows through a material with strong SOC, it induces a transverse charge current due to spin-dependent electron deflection. This results in a measurable electric field or voltage across the sample, thereby enabling electrical detection of spin currents.

As schematically illustrated in Fig. 1.8, spin-up and spin-down electrons experience opposite deflections due to SOC. Their spatial separation leads to net charge accumulation at the transverse edges of the material, generating an electric field E_{ISHE}:

$$E_{ISHE} = \theta_{SH}\frac{\hbar}{2e}(J_s\times\hat{\sigma}) \tag{1.33}$$

Here, J_s is the spin current density and σ is the spin polarization vector, $\hbar$ is the reduced Planck constant, and eee is the elementary charge (with $e > 0$). The direction of E_{ISHE} follows the right-hand rule relative to J_s and σ.

This electric field serves as a direct electrical readout of spin current, making ISHE a widely used detection method in experiments involving spin pumping, spin Seebeck effect, and SMR.

(5) Importance in Spintronics and Material Engineering

The practical realization of efficient SHE- and ISHE-based devices hinges on both material choice and structural engineering. For example, TIs such as BiSb exhibit extraordinarily large θ_{SH}, often exceeding unity, owing to their spin–momentum–locked surface states. These properties make TIs particularly attractive for spin current generation and detection at room temperature.

Beyond the intrinsic properties, extrinsic factors—including interface quality, crystalline orientation, and impurity scattering—significantly affect spin transparency and the magnitude of spin-to-charge conversion. Proper control of these structural features is essential to optimize spin injections, minimize spin loss, and enhance signal reliability.

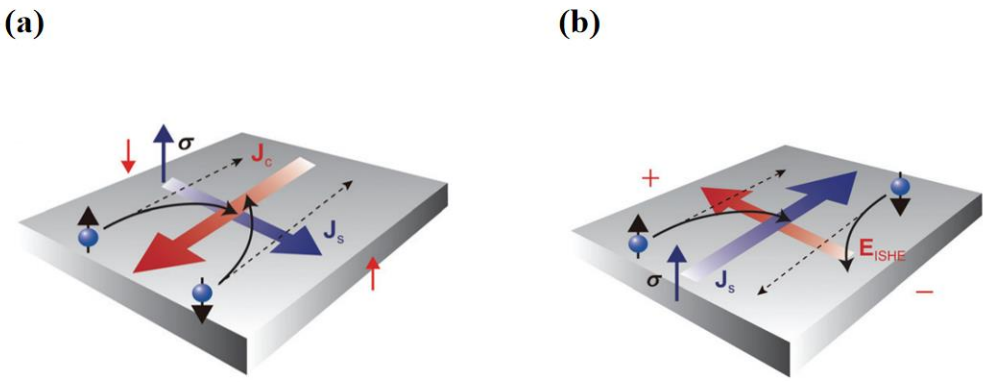

Figure 1.8. (a) Schematic illustration of the SHE, where spin-up and spin-down electrons are deflected transversely due to spin–orbit coupling. (b) ISHE, where a spin current is converted into a transverse charge current. Reproduced from Ref. 16 with permission from AIP.

In the context of this thesis, the utilization of SHE and ISHE in TI/FM heterostructures offers a unified platform for both spin injection and electrical detection, enabling a comprehensive study of spin transport phenomena across a wide temperature range. Together, the SHE and ISHE constitute the fundamental mechanism for charge–spin interconversion, serving as the basis for the all-electrical

manipulation of spin information and supporting the development of next-generation spintronic sensors and logic devices.

1.2.4. Physical Principles of Magnetoresistive Effects: AMR and SMR

(1) Anisotropic magnetoresistance (AMR)

The phenomenon of AMR was first discovered in 1857 by William Thomson, later known as Lord Kelvin, in Glasgow.[44] While Lord Kelvin is widely recognized for his contributions to fundamental physics, this discovery eventually laid the foundation for practical engineering applications in magnetic sensing and recording—more than a century later.

In ferromagnetic metals, three primary types of resistivity changes are typically considered:

① those arising from changes in magnetization at a fixed temperature,

② those driven by temperature-induced variations in magnetization, and

③ those dependent on the relative orientation between magnetization and the electric current.

The third category is referred to as the anisotropic magnetoresistance effect, or orientation-dependent resistivity, as originally termed by Smit.[45] It is now well established as a fundamental spintronic phenomenon arising from the interplay between magnetic and electronic transport properties.[46,47]

AMR manifests as a directional dependence of the electrical resistivity on the angle θ between the electric current J and the magnetization vector M. In most ferromagnetic metals, the resistivity is higher when the current is aligned parallel to magnetization than when it is perpendicular.[47] The AMR ratio is defined as:

$$\frac{\Delta\rho}{\rho} = \frac{\rho_{\parallel} - \rho_{\perp}}{\rho_{\perp}} \tag{1.34}$$

or equivalently,

$$\rho(\theta) = \rho_{\perp} + (\rho_{\parallel} - \rho_{\perp})\cos^2\theta = \rho_{\perp} + \Delta\rho\cos^2\theta \tag{1.35}$$

where $\rho_{\parallel}$ and $\rho_{\perp}$ represent the resistivities when the current is parallel and perpendicular to the magnetization, respectively. In ferromagnetic metals exhibiting positive AMR (such as Ni), the resistivity reaches its maximum when the magnetization is parallel to the current and minimum when they are perpendicular (Fig. 1.9). This angular dependence results in a characteristic $\cos^2\theta$ profile, which is commonly used to extract the AMR ratio experimentally.

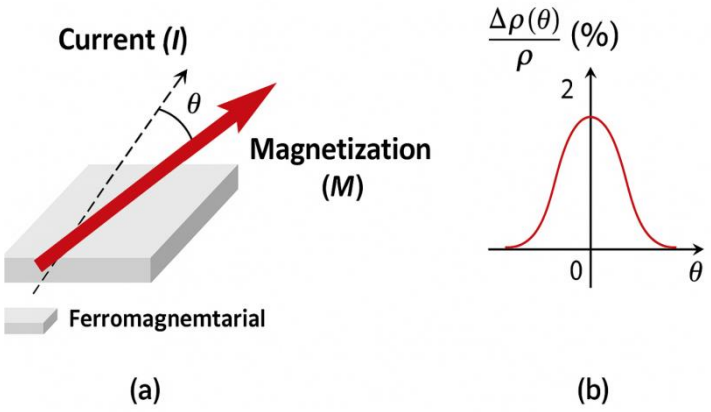

Figure 1.9. Schematic illustration of the AMR effect. (a) Definition of the angle θ between the current I and magnetization M. (b) Angular dependence of resistivity, showing a $\cos^2\theta$ behavior with maximum at $M \parallel I$ and minimum at $M \perp I$.

From a microscopic perspective, AMR arises due to spin–orbit interaction in the presence of exchange-split d-states. Within the framework of the s–d scattering model, conduction electrons are scattered by nonmagnetic impurities into localized d-orbitals. These orbitals are subject to an effective exchange field H_{ex}, and experience spin–orbit coupling described by the Hamiltonian:

$$H_{so} = \hat{\lambda}_{so} L \cdot S \tag{1.36}$$

where λ_{SO} is the spin-orbit coupling constant, L is the orbital angular momentum operator, and S is the spin angular momentum operator. The presence of spin–orbit coupling causes the localized d-states to become spin-mixed, leading to anisotropic scattering probabilities that depend on the current magnetization angle.[48]

AMR is not only of theoretical interest, but also of practical importance in magnetoresistive sensor technologies. It has been utilized in magnetic field detectors for digital storage and magnetic bubble memory systems. These sensors often fabricated using thin-film technology, benefit from AMR's sensitivity to magnetization orientation. However, it is noteworthy that the magnitude of the AMR effect in thin films is generally smaller than that observed in bulk materials.[47] This reduction is attributed to factors such as film thickness, grain size, and deposition conditions all of which influence the electron scattering environment and thus the AMR magnitude.

In this work, the AMR effect was measured as a baseline to evaluate the intrinsic magnetic properties of the ferromagnetic layer and to provide a point of comparison for other spin-dependent phenomena, such as SMR, which will be discussed in the following subsection.

While the AMR effect provides valuable insight into spin-dependent scattering in conducting ferromagnets, it becomes ineffective in systems where the magnetic layer is insulating. To address this limitation, the SMR has emerged as a complementary mechanism for detecting magnetization orientation and interfacial spin transport, as discussed in the following section.

(2) Spin Hall magnetoresistance

Magnetoresistance (MR) refers to the phenomenon where the electrical resistance of a material depends on its magnetization state. Classical examples include AMR, GMR, and TMR, which have been widely employed in magnetic memory and sensing technologies. Recent advances in spin–orbit coupling physics have unveiled SMR, a new form of magnetoresistance arising from the coupled dynamics of the SHE, ISHE, and interfacial spin current.[49]

SMR is typically observed in bilayer structures consisting of a non-magnetic heavy metal (e.g., Pt, Ta) and a ferromagnetic insulator (e.g., YIG).[49] When an electric current J_e flows through the heavy metal layer, the spin Hall effect generates a transverse pure spin current with spin polarization P orthogonal to both J_e and the film normal. This spin accumulation builds up at the interface with the magnetic layer.[27,49]

At the interface, part of this spin current is either reflected or absorbed, depending sensitively on the orientation of the magnetization vector M in the ferromagnet. When the magnetization is parallel to the spin polarization direction ($m \parallel \hat{\sigma}$), the spin-mixing interaction is minimized and most of the spin current is reflected. This reflected spin current then generates an opposite in-plane voltage via the inverse spin Hall effect and reduces the channel resistance. In contrast, when magnetization is perpendicular to the spin polarization direction ($m \perp \hat{\sigma}$), spin transfer becomes efficient, leading to enhanced spin-current absorption at the interface. The variation in reflected spin current modifies the ISHE-induced voltage in the metal layer, resulting in a magnetization-dependent resistance, this is the essence of SMR[49,50], as shown in figure 1.10.

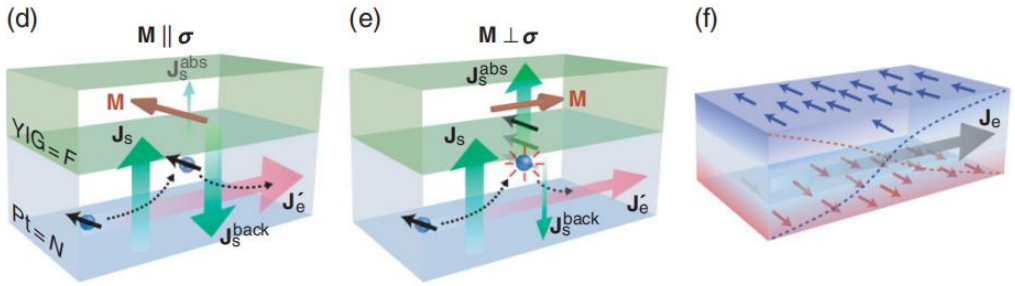

Figure 1.10. Schematic of spin Hall magnetoresistance: (d) M ∥ σ; (e) M ⊥ σ; (f) spin accumulation profile across the metal layer. Reproduced from Ref. 49 with permission from APS.

The interfacial spin current density j_s can be expressed as:

$$j_s = \frac{G_r}{e} m \times (m \times \mu_s) \tag{1.37}$$

where: G_r is the real part of the spin mixing conductance at the NM/FM interface, $m = M / |M|$ is the unit vector of the magnetization, μ_s is the interfacial spin accumulation vector, and e is the elementary charge.

As a result, the longitudinal resistance in the metal exhibits a characteristic angular dependence.[51] This dependence is typically measured by rotating the sample magnetization while monitoring the longitudinal resistance in the plane. The resistance follows the expression:

$$R(\theta) = R_0 - \Delta R \sin^2\theta \tag{1.38}$$

where: R_0 is the resistance when $M \parallel J_e$, ΔR is the SMR amplitude, θ is the angle between the magnetization direction and spin accumulation direction (usually the y-axis).

Thus, resistance is maximized when $M \parallel J_e$ and minimized when $M \perp J_e$. Although this angular behavior is similar to AMR, the underlying mechanisms differ substantially: AMR originates from intrinsic spin-dependent scattering in ferromagnetic conductors, whereas SMR results from interfacial spin reflection and absorption modulated by the FM layer.

To clarify these differences, Table 2 below compares the characteristics of AMR and SMR:

Feature	AMR	SMR
Effect origin	Spin-dependent scattering in FM	SHE + ISHE with spin current modulation at interface
Material system	Ferromagnetic metals	NM/FM bilayers(including metallic FMs and magnetic insulators)
Spin Hall effect required	No	Yes
Magnetic insulator required	No	Not required (typically FMI such as YIG, but also observed in metallic FM and AFM systems)
Angular dependence	$\cos^2\theta$ between M and J_e	$\sin^2\theta$ between M and μ_s
Current path	Through ferromagnet	Through non-magnetic layer
Sensitivity origin	Bulk scattering	Interfacial spin absorption/reflection

SMR provides a powerful tool for investigating spin transport across insulating ferromagnets and probing interfacial spin transparency.[52] It also complements other magnetoresistive effects by enabling all-electrical detection of magnetization direction even in insulating magnetic systems. Owing to its versatility and robustness, SMR has been applied in spintronic devices such as spin-current detectors, spin-torque oscillators, and magnetic insulator-based memory elements.

While the angular dependence resembles that of AMR, the physical origins are distinct: AMR is due to spin-dependent bulk scattering in ferromagnetic conductors, whereas SMR results from interfacial spin absorption/reflection modulated by the FM layer.

In practical experiments, SMR is often estimated from the longitudinal resistance difference when the magnetization is aligned along different axes. Specifically, SMR is defined as:

$$SMR = \frac{R_y^{xx} - R_z^{xx}}{R_z^{xx}} \tag{1.39}$$

where R_y^{XX} and R_z^{XX} are the resistances when the magnetization is oriented along the in-plane y-axis and out-of-plane z-axis, respectively. The coordinate system for these measurements is illustrated in Figure 1.11, where the x-axis corresponds to the current direction, y-axis lies in-plane and transverse to the current, and z-axis is normal to the film plane.

The coordinate system used in these measurements is shown in Figure 1.11, where the x-axis denotes the current direction, the y-axis is transverse in-plane, and the z-axis is normal to the film plane.

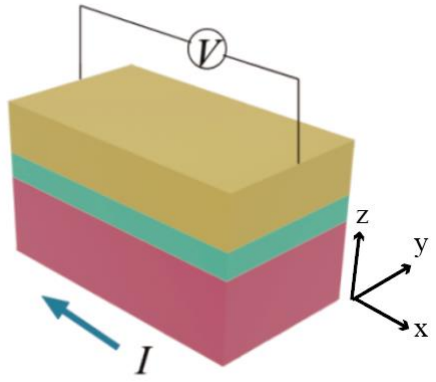

Figure 1.11. Schematic of the SMR measurement configuration. The current flows along x, and the voltage is measured longitudinally. The x, y, and z axes correspond to current, transverse, and out-of-plane directions.

To quantitatively analyze the SMR effect, we adopted the theoretical model proposed by Liu et al.[53], which accurately captures the dependence on spin Hall angle, spin diffusion length, and current shunting through the FM layer. The SMR ratio is given by:

$$\frac{\Delta R_{XX}}{R_{XX}^{z}} \propto \theta_{SH}^{2} \cdot \frac{2\lambda_N}{d} \cdot \frac{\tanh(\frac{d}{2\lambda_N})}{1+\xi}[1-\frac{1}{\cosh(\frac{d}{\lambda_N})}] \tag{1.40}$$

where θ_{SH} is the spin Hall angle, λ_N is the spin diffusion length of the heavy metal, $\xi \equiv (\rho_N t_F / \rho_F d)$ and ρ_N, ρ_F, t_N, t_F denote the resistivities and thicknesses of the NM and FM layers, respectively. This formulation captures the effect of spin current absorption and current shunting between layers.

1.2.5. Second Harmonic Response: Principle and Application in Spin Detection

The second harmonic Hall voltage (2ω) method has emerged as a powerful tool in spintronics[54-56] for separating and quantifying different spin–orbit-induced effects in magnetic heterostructures. Unlike

conventional magnetoresistive measurements that typically rely on linear (first harmonic) responses, this technique probes the nonlinear dynamic response of spin systems under alternating current excitation. It is particularly effective in distinguishing between SOT and thermoelectric contributions, as well as in detecting subtle spin interactions in systems where first-harmonic signals are weak or ambiguous.

(1) Principle of Second Harmonic Detection

When an alternating current (AC) $I = I_0 \sin(\omega t)$ is applied to a bilayer system such as a NM/FM, spin–orbit coupling—primarily via the spin Hall effect in the NM and possibly supplemented by interfacial Rashba effects—induces spin accumulation at the interface. This spin accumulation can exert a torque on the magnetization, known as SOT, which modulates the orientation of the magnetization vector *M*. The interaction between the current-induced spin polarization and magnetization leads to oscillatory changes in the effective magnetic field, which in turn affects the measured Hall voltage. The underlying physical picture of spin accumulation, effective fields, and torque-induced magnetization dynamics is illustrated in Figure 1.12.

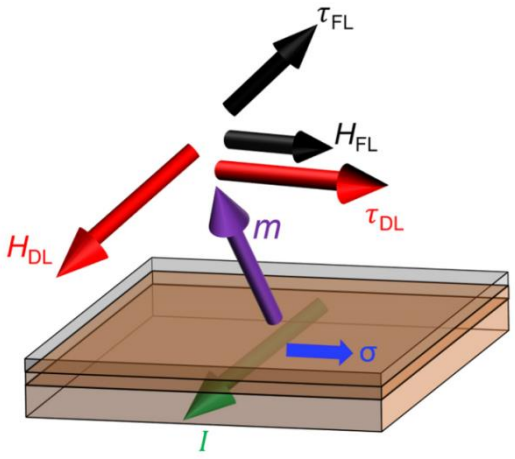

Figure 1.12. Schematic of spin–orbit torques in a NM/FM bilayer. Damping-like and field-like torques act on the magnetization due to spin accumulation generated by the spin Hall effect. Reproduced from Ref. 55 with permission from Elsevier.

The total Hall voltage measured under AC excitation can be decomposed as:

$$V_{\mathrm{H}}(t) = V_{\mathrm{H}}^{\omega} \sin(\omega t) + V_{\mathrm{H}}^{2\omega} \sin(2\omega t) + \ldots \tag{1.41}$$

Here, V_{H}^{ω} is the first harmonic component, mainly corresponding to AHE or planar Hall effect (PHE), and $V_{\mathrm{H}}^{2\omega}$ is the second harmonic component, which contains signatures of SOT, SMR, and anomalous Nernst effect (ANE).

(2) Physical Contributions to the Second Harmonic Signal

Several mechanisms contribute to the second harmonic Hall response[54,57]:

① Field-like torque (FLT): Originates from Rashba-type or interfacial SOC, generating an effective magnetic field transverse to the current direction. It appears as a symmetric contribution to $V_{\mathrm{H}}^{2\omega}$. Field-like term is negligible in BiSb (≈ two orders of magnitude smaller than Damping-like torque)[58].

② Damping-like torque (DLT): Induced by spin Hall effect in the NM layer, acting collinearly with the magnetization. It gives rise to an antisymmetric signature in $V_{\mathrm{H}}^{2\omega}$, which can be isolated via angle-dependent measurements.

③ ANE: Thermoelectric contribution due to vertical temperature gradients, particularly in thin-film structures under high current density. The ANE also modulates $V_{\mathrm{H}}^{2\omega}$ and must be subtracted for accurate torque quantification.

These components can be experimentally separated by sweeping the external magnetic field direction or magnitude while analyzing the angular dependence of the second harmonic signal.

(3) Application and Significance in Spin Detection

The second harmonic method offers several advantages for spintronic measurements[55,56,59]:

① Quantification of SOT efficiencies: The effective fields associated with FLT and DLT can be extracted from the angular and field-dependent $V_{\mathrm{H}}^{2\omega}$, enabling estimation of spin Hall angle and torque ratio.

② Non-invasive probing of spin–orbit interactions: Unlike ferromagnetic resonance (FMR), this technique requires no microwave equipment and can be performed using low-frequency electronics.

③ Evaluation of material interfaces: Differences in the second harmonic response provide insight into spin transparency, spin mixing conductance, and interfacial SOC strength across various NM/FM combinations.

In the present work, we employed the second harmonic Hall voltage method to analyze the spin–orbit torques in topological insulator/ferromagnet heterostructures. By applying an in-plane rotating magnetic field and recording the $V_{\mathrm{H}}^{2\omega}$ component, we quantitatively extracted the contributions from damping-like and field-like torques and confirmed their temperature-dependent behavior. This allowed us to decouple interfacial spin transport mechanisms from bulk magnetoresistive effects such as SMR and AMR.

1.3. Material Platform: Topological Insulators and Magnetic Heterostructures

1.3.1. Physical Properties and Advantages of TIs

TIs are a special class of materials that behave as electrical insulators in their interior (bulk) but conduct electricity on their surfaces. This unique behavior arises from a strong intrinsic property known as SOC, which modifies the electronic band structure and gives rise to protected surface states.[60-62]

In conventional insulators, the valence and conduction bands are separated by a bulk energy gap, and no states exist within this gap. In contrast, TIs exhibit a nontrivial band topology caused by SOC-induced band inversion, where the order of conduction and valence bands is reversed compared to ordinary insulators. This leads to the emergence of gapless surface states that traverse the band gap. These surface states are protected by time-reversal symmetry, making them robust against non-magnetic impurities and weak disorder.

Figure 1.13 schematically illustrates the emergence of topological surface states in topological insulators. As shown in Fig. 1.13(a), helical edge states appear at the boundary of a two-dimensional topological insulator, where counter-propagating electrons possess opposite spin orientations. Figure 1.13(b) presents the energy–momentum dispersion of surface states crossing the bulk band gap and forming a Dirac point as a consequence of strong spin–orbit coupling. Figure 1.13(c) depicts a real-space picture of a three-dimensional topological insulator, in which conducting surface states surround an insulating bulk.[40]

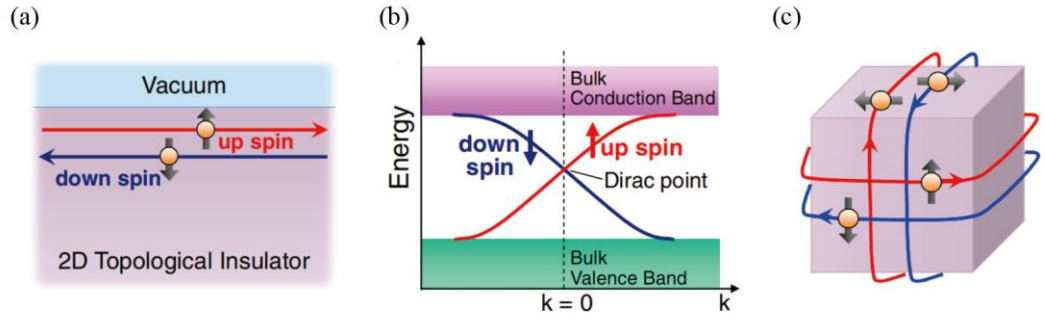

Figure 1.13. Schematic illustration of the emergence of topological surface states. (a) Helical edge states at the boundary of a two-dimensional topological insulator, where counter-propagating electrons possess opposite spin orientations. (b) Energy–momentum dispersion of topological surface states crossing the bulk band gap and forming a Dirac point due to spin–orbit coupling. (c) Real-space picture of a three-dimensional topological insulator, in which conducting surface states surround an insulating bulk. Reproduced from Ref. 40 with permission from JPS.

A key feature of these surface states is spin–momentum locking, where the spin direction of an electron is locked perpendicular to its momentum. As a result, electrons cannot be scattered backward without simultaneously flipping their spin, which is prohibited by time-reversal symmetry. This protection mechanism suppresses backscattering and enables efficient, low-dissipation electronic transport on the surfaces of TIs. Figure 1.14 illustrates the surface Dirac cone of a 3D TI, where the linear energy dispersion and helical spin texture manifest the spin–momentum locking of surface states.[62-66]

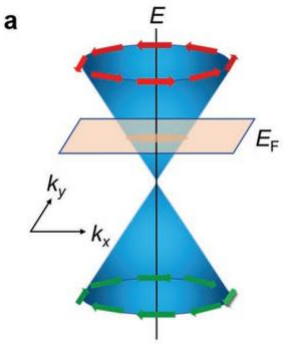

Figure 1.14. Illustration of spin-momentum locking in a 3D topological insulator. The tangential spin orientation around the Dirac cone indicates a helical spin texture. Reproduced from Ref. 63 with permission from Wiley.

The concept of TIs is rooted in earlier discoveries in topological physics, such as the quantum Hall effect (QHE). In the QHE, 2D electron systems subjected to strong magnetic fields exhibit edge states

that are topologically protected. However, in TIs, no external magnetic field is required—the strong intrinsic SOC alone induces a topological phase under time-reversal symmetry.

Well-known three-dimensional TIs such as Bi_2Se_3, Bi_2Te_3, and Sb_2Te_3 exhibit a single Dirac cone in their surface electronic structure. The energy-momentum relationship of these surface states is linear near the Dirac point, similar to relativistic particles, which enables high-mobility, spin-polarized surface conduction.

TIs have significantly deepened our understanding of quantum phases of matter and hold great promise for applications in low-power electronics, spintronics, and quantum computing. Their robust, spin-polarized surface states provide an excellent platform for investigating spin–orbit torques, topological magnetoelectric effects, and Majorana fermions, particularly when interfaced with magnetic or superconducting layers. Compared with conventional heavy metals such as Pt and Ta, TIs exhibit higher spin–orbit efficiency and lower energy dissipation, as will be further discussed in Section 1.3.2.

1.3.2. Spin Transport Mechanisms in TI/FM Heterostructures

To harness the unique spintronic properties of TIs, extensive research has focused on heterostructures formed by interfacing TIs with FM materials. In such bilayer systems, the interplay between the spin-momentum-locked surface states of the TI and the magnetization of the FM layer give rise to rich spin transport phenomena, including SOT, SA, and SMR. These three representative effects form the experimental foundation for evaluating the spin transport properties of TI/FM heterostructures under electrical excitation. These three transport mechanisms form the basis for evaluating interfacial spin dynamics in TI/FM heterostructures, and their experimental implementation will be discussed in detail in Chapters 3 and 4.

In addition to these DC transport-based mechanisms, previous studies have also employed microwave-driven techniques such as spin pumping to investigate spin–charge conversion in TI/FM systems. Here, we briefly introduce this representative method to provide broader context for experimental approaches reported in the literature.[24,67]

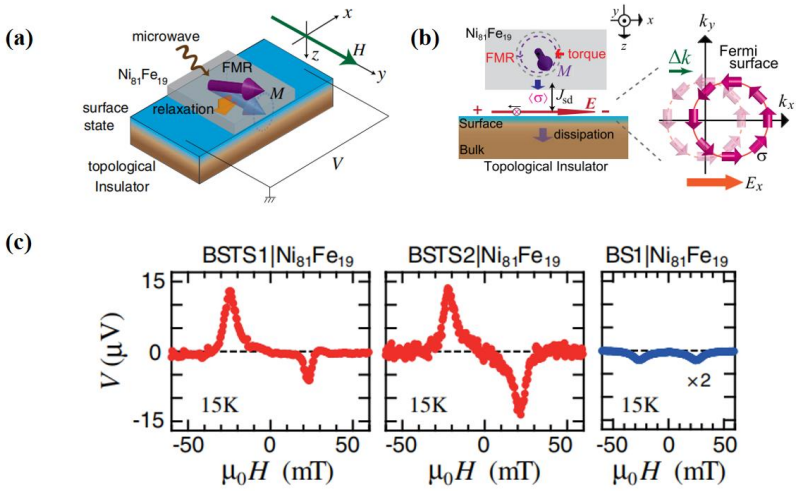

Figure 1.15. (a) A schematic illustration of the experiment of the spin-electricity conversion effects. (b) A schematic illustration of spin injection causes a shift of the Fermi surface, thereby generating a spin-polarized current. (c) The longitudinal voltage generated by the spin-polarized current. Reproduced from Ref. 67 with permission from APS.

Typically, through the FMR of a ferromagnet, spin angular momentum can be transferred into another material in contact with it; this method is known as spin pumping. As introduced above, the surface of a topological insulator possesses spin-momentum locking protected by time-reversal symmetry. When a spin current is injected into the TI, the populations of up spins and down spins change, generating a driven spin current. As shown in Fig. 1.15(a) and (b), microwave-induced ferromagnetic resonance in a NiFe alloy injects spins into the TI, causing a shift in the spin-momentum locking of the TI surface states and thereby producing a polarized spin current. This polarized spin current can then be detected either via the inverse spin Hall effect or through the longitudinal resistance measurement, as illustrated in Fig. 1.15(c).[67]

(1) Material Platforms for TI/FM Structures

Several topological insulator materials have been widely studied due to their strong spin–orbit coupling, well-defined surface states, and compatibility with FM layers. Common examples include:

Bi_2Se_3 and Bi_2Te_3: Prototypical 3D TIs with a single Dirac cone and a relatively large bulk band gap. These materials exhibit strong spin–momentum locking and have been widely used in spin pumping and SOT measurements.[24,67,68]

$(Bi,Sb)_2Te_3$ and BiSb: Alloyed TIs with tunable Fermi levels, allowing surface-state-dominated transport. BiSb, in particular, is notable for its exceptionally large spin Hall angle (SHA), making it highly suitable for spin–orbit torque applications.[69-71]

Sb_2Te_3 and α-Sn: Alternative materials with distinct electronic structures that offer different interfacial properties.[72,73]

In these heterostructures, the TI is typically grown by molecular beam epitaxy (MBE) or sputtering, and is coupled with FM layers such as CoFeB, YIG, or CoFe. The quality of the interface, especially its cleanliness and sharpness, plays a crucial role in determining spin transport efficiency.

(2) Comparison with Conventional Heavy Metals

Compared to heavy metals such as Pt, Ta, and W, TIs offer several distinct advantages:

Higher Spin Hall Angle: TIs like BiSb exhibit SHA values > 1, much larger than those of Pt (~0.08) or β-Ta (~0.15).

Surface-State Dominated Transport: Enables robust spin-polarized current generation with minimal scattering and low energy loss.

Lower Power Consumption: The dissipationless nature of topological surface states reduces Joule heating, making them ideal for energy-efficient devices.

These advantages highlight the superior spin conversion efficiency and energy-saving potential of TI-based heterostructures compared with conventional heavy metals. BiSb, in particular, combines a large spin Hall angle with moderate electrical conductivity, making it a leading candidate for next-generation, low-power spin–orbit torque applications.

1.3.3. Temperature Dependence of Spin Phenomena in TI/FM Structures

Spintronic devices are widely considered promising candidates for next-generation memory and logic technologies. While HM/FM heterostructures have been extensively studied, their relatively low charge-to-spin conversion efficiency remains a major bottleneck for practical applications. TIs, on the other hand, offer robust spin–momentum–locked surface states and strong spin–orbit coupling, positioning them as attractive alternatives to traditional spin Hall materials. Constructing TI/FM heterostructures has therefore become a key strategy for exploring novel and efficient spintronic

phenomena. Temperature plays a crucial role in governing these phenomena. Both surface-state contributions and interfacial spin transmission can vary significantly with thermal fluctuations.

At room temperature, Yi Wang et al. employed magneto-optical Kerr effect (MOKE) microscopy to directly observe current-induced magnetization switching in Bi_2Se_3/NiFe heterostructures. Their study revealed a high charge-to-spin conversion efficiency of approximately 1.0–1.75, predominantly attributed to the topological surface states of Bi_2Se_3. Remarkably, they achieved magnetization switching with a current density as low as 6×10^5 A/cm^2 , one to two orders of magnitude smaller than that required in conventional HM-based systems.[74] This room-temperature behavior serves as a reference point for subsequent investigations into how spin–charge conversion and interfacial effects evolve with temperature. These results confirm that topological surface states remain active contributors to spin‑charge conversion even at ambient conditions.

Extending beyond room temperature, Murong Lang et al. investigated Bi_2Se_3/YIG (yttrium iron garnet) heterostructures and demonstrated that magnetic interactions at the TI/ferromagnetic insulator (FMI) interface persist up to 130 K. Their analysis of magnetoresistance loops and MOKE signals provided direct evidence of interfacial magnetic ordering.[75] Moreover, they showed that YIG films with perpendicular magnetic anisotropy could effectively modulate the surface magnetism of Bi_2Se_3 even near room temperature. These findings highlight that proximity-induced magnetism and spin–orbit interactions in TIs can remain robust across a wide temperature range.

Together, these studies indicate that spin–orbit torque generation and interfacial magnetic coupling in TI/FM or TI/FMI systems remain effective over a broad temperature range. These findings emphasize that temperature is a critical parameter for evaluating both the practical stability of TI-based spintronic devices and the competition between surface-state–dominated and bulk-dominated spin transport in TI/FM heterostructures.

1.4. Spintronic Applications and Outlook

Spintronics, as a field leveraging the spin degree of freedom of electrons, has evolved from fundamental physical phenomena to practical device architectures. Among various spin-orbit-interaction-driven effects, such as SOT and SMR, the development of TI/FM heterostructures has opened new frontiers for efficient spin–charge conversion. These effects offer the potential for realizing high-

performance, low-power spintronic devices across a broad range of application domains. This section provides an overview of key application areas that motivate ongoing research into spin transport mechanisms and materials optimization in TI-based systems.

1.4.1. Spintronic Magnetic Sensors

Magnetic sensors play a crucial role in modern data storage technologies, particularly in HDDs, where they are responsible for detecting nanoscale magnetic field variations from recording media. Conventional technologies, such as GMR and TMR sensors, have reached performance saturation in terms of sensitivity, miniaturization, and energy efficiency. In this context, magnetic devices exploiting the direct spin Hall effect (DSHE) in TI/FM heterostructures have the potential to offer several engineering advantages over conventional magnetoresistive technologies. Their structure is remarkably simple, requiring only a single ferromagnetic layer to detect spin-dependent resistance changes. This simplicity facilitates further miniaturization and integration, which are essential for next-generation HDD read heads. Moreover, the absence of current flow through multilayer junctions eliminates local Joule heating within the sensor pillar, enabling thermally stable and energy-efficient operation.

In high-density HDD read-head applications, the linearity and noise performance of magnetic sensors are strongly affected by the magnetization reversal mechanism of the sensing layer. Square-like magnetization switching, typically involving domain wall motion, leads to large hysteresis, nonlinear response near zero field, and Barkhausen noise. In contrast, smooth magnetization rotation provides linear and reversible response with low coercivity, which is crucial for achieving low-noise, stable readout. Achieving smooth magnetization rotation remains a key design target for improving sensor linearity and noise performance.

1.4.2. Spin–Orbit Torque Devices

SOT provides an efficient mechanism for manipulating magnetization by converting a charge current into a transverse spin current through spin–orbit coupling. Compared with conventional STT, SOT enables faster magnetization switching and improved endurance due to the separation of read and write current paths. In TI/FM heterostructures, the strong spin–momentum locking of the TI surface states leads to exceptionally high charge-to-spin conversion efficiency, resulting in critical switching current densities one to two orders of magnitude lower than those observed in heavy-metal-based

systems.[74,76] These characteristics make topological insulators such as BiSb promising spin-current sources for energy-efficient non-volatile memories, oscillators, and logic devices.[77]

Although the primary focus of this thesis is spin-based magnetic sensing, the device-level SOT and SMR measurements offer quantitative insight into interfacial spin transport in TI/FM heterostructures, particularly into the efficiency of torque generation and its dependence on interface transparency and spin-memory loss. These sensor-oriented results deepen the understanding of spin–orbit-torque generation in TI/FM systems and may guide the future optimization of SOT-based device performance.

1.5. Research Objectives

Building on these motivations, this thesis pursues two directions: (1) application-driven magnetic field sensor development, and (2) mechanism-driven analysis of charge-to-spin conversion efficiency in TI/FM heterostructures.

Accordingly, the objectives of this thesis are:

1. Demonstrate the feasibility and advantages of TI/FM heterostructures as high-sensitivity spin Hall sensors for HDD technologies.

2. Provide a quantitative comparison of the spin Hall angle measured by SA, SOT, and SMR across a wide temperature range.

3. Elucidate the temperature-dependent behavior of spin transport and interfacial coupling phenomena.

These objectives ensure that the outcomes contribute both to the practical implementation of TI-based magnetic field sensors and to the fundamental understanding of the spin Hall effect evaluation methodology in complex TI/FM heterostructures.

1.6. Reference

1. R. Chaudhary, and A. Kansal, Int. J. Tech. Res. Appl. 3, 63 (2015).
2. R. Wood, J. Magn. Magn. Mater. 321, 555 (2009).
3. A. S. Hoagland, IEEE Trans. Magn. 39, 1871 (2003).
4. M. Taktak-Meziou, A. Chemori, J. Ghommam, and N. Derbel, Proc. IEEE/RSJ Int. Conf. Intell. Robots Syst., 4401 (2013).

5. I. R. McFadyen, E. E. Fullerton, and M. J. Carey, MRS Bull. 31, 379 (2006).
6. M. Taktak-Meziou, A. Chemori, J. Ghommam, and N. Derbel, Proc. IEEE/RSJ Int. Conf. Intell. Robots Syst., 4401 (2013).
7. I. Bakonyi, and L. Péter, Prog. Mater. Sci. 55, 107 (2010).
8. S. Yuasa, and D. D. Djayaprawira, J. Phys. D: Appl. Phys. 40, R337 (2007).
9. S. S. P. Parkin, C. Kaiser, A. Panchula, P. M. Rice, B. Hughes, M. Samant, and S.-H. Yang, Nat. Mater. 3, 862 (2004).
10. A. Moser, K. Takano, D. T. Margulies, M. Albrecht, Y. Sonobe, Y. Ikeda, S. Sun, and E. E. Fullerton, J. Phys. D: Appl. Phys. 35, R157 (2002).
11. D. Weller, G. Parker, O. Mosendz, E. Champion, B. Stipe, X. Wang, T. Klemmer, G. Ju, and A. Ajan, IEEE Trans. Magn. 50, 3100108 (2014).
12. M. T. Kief, MRS Bull. 43, 87 (2018).
13. M. H. Kryder, E. C. Gage, T. W. McDaniel, W. A. Challener, R. E. Rottmayer, G. Ju, Y.-T. Hsia, and M. Fatih Erden, Proc. IEEE 96, 1810 (2008).
14. M. N. Baibich, J. M. Broto, A. Fert, F. Nguyen Van Dau, F. Petroff, P. Etienne, G. Creuzet, A. Friederich, and J. Chazelas, Phys. Rev. Lett. 61, 2472 (1988).
15. J. S. Moodera, L. R. Kinder, T. M. Wong, and R. Meservey, Phys. Rev. Lett. 74, 3273 (1995).
16. T. Seki, T. Shimatsu, Y. Kawada, Y. Nagamine, K. Enomoto, T. Okamoto, and K. Saito, IEEE Trans. Magn. 53, 3200308 (2017).
17. K. Ando, S. Takahashi, J. Ieda, Y. Kajiwara, H. Nakayama, T. Yoshino, K. Harii, Y. Fujikawa, M. Matsuo, S. Maekawa, and E. Saitoh, J. Appl. Phys. 109, 103913 (2011).
18. L. Liu, T. Moriyama, D. C. Ralph, and R. A. Buhrman, Phys. Rev. Lett. 106, 036601 (2011).
19. M. Johnson and R. H. Silsbee, Phys. Rev. Lett. 55, 1790 (1985).
20. I. M. Miron, K. Garello, G. Gaudin, P.-J. Zermatten, M. V. Costache, S. Auffret, S. Bandiera, B. Rodmacq, A. Schuhl, and P. Gambardella, Nature 476, 189 (2011).
21. C. Hahn, G. Woltersdorf, R. Walser, M. Kläui, H. G. Bauer, and G. Schmidt, Phys. Rev. B 87, 174417 (2013).
22. S. A. Wolf, D. D. Awschalom, R. A. Buhrman, J. M. Daughton, S. von Molnár, M. L. Roukes, A. Y. Chtchelkanova, and D. M. Treger, Science 294, 1488 (2001).
23. J. M. Kikkawa and D. D. Awschalom, Phys. Rev. Lett. 80, 4313 (1998).

24. T. Kimura, Y. Otani, T. Sato, S. Takahashi, and S. Maekawa, Phys. Rev. Lett. 98, 156601 (2007).
25. A. R. Mellnik, J. S. Lee, A. Richardella, J. L. Grab, P. J. Mintun, M. H. Fischer, A. Vaezi, A. Manchon, E.-A. Kim, N. Samarth, and D. C. Ralph, Nature 511, 449 (2014).
26. Y. Fan, P. Upadhyaya, X. Kou, M. Lang, S. Takei, Z. Wang, J. Tang, L. He, L.-T. Chang, M. Montazeri, G. Yu, W. Jiang, T. Nie, R. N. Schwartz, Y. Tserkovnyak, and K. L. Wang, Nat. Mater. 13, 699 (2014).
27. J. C. Rojas-Sánchez, N. Reyren, P. Laczkowski, W. Savero, J.-P. Attané, C. Deranlot, M. Jamet, J.-M. George, L. Vila, and H. Jaffrès, Phys. Rev. Lett. 112, 106602 (2014).
28. Y.-T. Chen, S. Takahashi, H. Nakayama, M. Althammer, S. T. B. Goennenwein, E. Saitoh, and G. E. W. Bauer, Phys. Rev. B 87, 144411 (2013).
29. J. Bass and W. P. Pratt Jr., J. Phys. Condens. Matter 19, 183201 (2007).
30. M. Tran, H. Jaffrès, C. Deranlot, J.-M. George, A. Fert, A. Miard, and A. Lemaître, Phys. Rev. Lett. 102, 036601 (2009).
31. Y. Niimi and Y. Otani, Rep. Prog. Phys. 78, 124501 (2015).
32. G. E. W. Bauer, E. Saitoh, and B. J. van Wees, Nat. Mater. 11, 391 (2012).
33. M. Isasa, E. Villamor, L. E. Hueso, M. Gradhand, and F. Casanova, Phys. Rev. B 91, 024402 (2015).
34. L. Liu, O. J. Lee, T. J. Gudmundsen, D. C. Ralph, and R. A. Buhrman, Phys. Rev. Lett. 109, 096602 (2012).
35. N. Tombros, C. Jozsa, M. Popinciuc, H. T. Jonkman, and B. J. van Wees, Nature 448, 571 (2007).
36. T. Jedema, A. Filip, and B. J. van Wees, Nature 410, 345 (2001).
37. S. O. Valenzuela and M. Tinkham, Nature 442, 176 (2006).
38. N. W. Ashcroft and N. D. Mermin, Solid State Physics (Cengage Learning India Press, 2003).
39. N. Nagaosa, J. Sinova, S. Onoda, A. H. MacDonald, and N. P. Ong, Rev. Mod. Phys. 82, 1539 (2010).
40. R. Karplus and J. M. Luttinger, Phys. Rev. 95, 1154 (1954).
41. Y. Ando, J. Phys. Soc. Jpn. 82, 102001 (2013).
42. J. Sinova, D. Culcer, Q. Niu, N. A. Sinitsyn, T. Jungwirth, and A. H. MacDonald, Phys. Rev. Lett. 92, 126603 (2004).
43. Y. K. Kato, R. C. Myers, A. C. Gossard, and D. D. Awschalom, Science 306, 1910 (2004).
44. A. Manchon and S. Zhang, J. Appl. Phys. 104, 043914 (2008).

45. W. Thomson, Proc. R. Soc. Lond. 8, 546 (1857).

46. J. Smit, Physica 17, 612 (1951).

47. T. R. McGuire and R. I. Potter, IEEE Trans. Magn. 11, 1018 (1975).

48. M. Ziese, Rep. Prog. Phys. 65, 143 (2002).

49. J. Kondo, Prog. Theor. Phys. 27, 772 (1962).

50. H. Nakayama, M. Althammer, Y.-T. Chen, K. Uchida, Y. Kajiwara, D. Kikuchi, T. Ohtani, S. Geprägs, M. Opel, S. Takahashi, R. Gross, G. E. W. Bauer, S. T. B. Goennenwein, and E. Saitoh, Phys. Rev. Lett. 110, 206601 (2013).

51. M. Althammer, S. Meyer, H. Nakayama, M. Schreier, S. Altmannshofer, M. Weiler, H. Huebl, S. Geprägs, M. Opel, R. Gross, D. Meier, C. Klewe, T. Kuschel, J.-M. Schmalhorst, G. Reiss, L. Shen, A. Gupta, Y.-T. Chen, G. E. W. Bauer, E. Saitoh, and S. T. B. Goennenwein, Phys. Rev. B 87, 224401 (2013).

52. T. Fischer, J. Lotze, M. Bechtel, R. Huber, M. Opel, S. Geprägs, R. Gross, and S. T. B. Goennenwein, Appl. Phys. Lett. 102, 222402 (2013).

53. N. Vlietstra, J. Shan, V. Castel, B. J. van Wees, and J. Ben Youssef, Phys. Rev. B 87, 184421 (2013)

54. J. Liu, T. Ohkubo, S. Mitani, K. Hono, and M. Hayashi, Appl. Phys. Lett. 107, 232408 (2015).

55. K. Garello, I. M. Miron, C. O. Avci, F. Freimuth, Y. Mokrousov, S. Blügel, S. Auffret, O. Boulle, G. Gaudin, and P. Gambardella, Nat. Nanotechnol. 8, 587 (2013).

56. C. Song, R. Zhang, L. Liao, Y. Zhou, X. Zhou, R. Chen, Y. You, X. Chen, and F. Pan, Prog. Mater. Sci. 116, 100761 (2021).

57. C. O. Avci, K. Garello, I. M. Miron, G. Gaudin, S. Auffret, O. Boulle, and P. Gambardella, Phys. Rev. B 90, 224427 (2014).

58. T. Taniguchi, J. Grollier, and M. D. Stiles, Phys. Rev. Appl. 3, 044001 (2015).

59. K. Yasuda, A. Tsukazaki, R. Yoshimi, K. S. Takahashi, M. Kawasaki, and Y. Tokura, Nat. Phys. 12, 555 (2016).

60. M. Hayashi, J. Kim, M. Yamanouchi, and H. Ohno, Phys. Rev. B 89, 144425 (2014).

61. M. Z. Hasan and C. L. Kane, Rev. Mod. Phys. 82, 3045 (2010).

62. X.-L. Qi and S.-C. Zhang, Rev. Mod. Phys. 83, 1057 (2011).

63. J. E. Moore, Nature 464, 194 (2010).

64. J. Wu, J. Liu, K. Watanabe, T. Taniguchi, and P. Kim, Adv. Mater. 31, 1806410 (2019).

65. Y. Xia, D. Qian, D. Hsieh, L. Wray, A. Pal, H. Lin, A. Bansil, D. Grauer, Y. S. Hor, R. J. Cava, and M. Z. Hasan, Nat. Phys. 5, 398 (2009).

66. H. Zhang, C.-X. Liu, X.-L. Qi, X. Dai, Z. Fang, and S.-C. Zhang, Nat. Phys. 5, 438 (2009).

67. Y. L. Chen, J. G. Analytis, J.-H. Chu, Z. K. Liu, S.-K. Mo, X. L. Qi, H. J. Zhang, D. H. Lu, X. Dai, Z. Fang, S. C. Zhang, I. R. Fisher, Z. Hussain, and Z.-X. Shen, Science 325, 178 (2009).

68. Y. Shiomi, K. Nomura, Y. Kajiwara, K. Eto, M. Novak, K. Segawa, Y. Ando, and E. Saitoh, Phys. Rev. Lett. 113, 196601 (2014).

69. X. Wang, Y. Deorani, K. Banerjee, N. Koirala, M. Brahlek, S. Oh, and H. Yang, Phys. Rev. Lett. 113, 097202 (2014).

70. Y. Wang, D. Zhu, Y. Wu, Y. Yang, J. Yu, R. Ramaswamy, R. Mishra, S. Shi, M. Elyasi, K. L. Teo, Y. Wu, and H. Yang, Science 349, 948 (2015).

71. Y. Fan, X. Kou, P. Upadhyaya, Q. Shao, L. Pan, M. Lang, X. Che, J. Montazeri, K. Murata, L.-T. Chang, M. Akyol, G. Yu, T. Nie, K. L. Wong, J. Liu, Y. Wang, Y. Tserkovnyak, and K. L. Wang, Nat. Nanotechnol. 11, 352 (2016).

72. C. H. Li, O. M. J. van 't Erve, S. Rajput, L. Li, and B. T. Jonker, Nat. Nanotechnol. 9, 218 (2014).

73. M. Jamali, J. S. Lee, J. S. Jeong, F. Mahfouzi, Y. Lv, Z. Zhao, B. K. Nikolić, K. A. Mkhoyan, N. Samarth, and J.-P. Wang, Nano Lett. 15, 7126 (2015).

74. H. Zhang and S.-C. Zhang, Phys. Status Solidi RRL 7, 72 (2013).

75. Y. Wang, D. Zhu, Y. Wu, Y. Yang, J. Yu, R. Ramaswamy, R. Mishra, S. Shi, M. Elyasi, K.-L. Teo, Y. Wu, and H. Yang, Nat. Commun. 8, 1364 (2017).

76. M. Lang, M. Montazeri, M. C. Onbasli, X. Kou, Y. Fan, P. Upadhyaya, K. Yao, F. Liu, Y. Jiang, W. Jiang, K. L. Wong, G. Yu, J. Tang, T. Nie, L. He, R. N. Schwartz, Y. Wang, C. A. Ross, and K. L. Wang, Nano Lett. 14, 3459 (2014).

77. A. Manchon, J. Železný, I. M. Miron, T. Jungwirth, J. Sinova, A. Thiaville, K. Garello, and P. Gambardella, Rev. Mod. Phys. 91, 035004 (2019).

78. T. Safranski, N. Reynolds, S. K. Sinha, S. Fukami, and S. A. Wolf, J. Appl. Phys. 128, 210902 (2020).

Chapter 2 Experimental Methods and Measurement Principles

2.1. Thin Film Deposition

2.1.1. Magnetron Sputtering System

Figure 2.1 presents the schematic of the magnetron sputtering system used in this study. Magnetron sputtering is a physical vapor deposition (PVD) technique that enables the fabrication of thin films with high purity, uniformity, and reproducibility.[1-3] Owing to its scalability and versatility, it is widely employed for the deposition of multilayer thin-film structures in spintronic and magnetic devices.

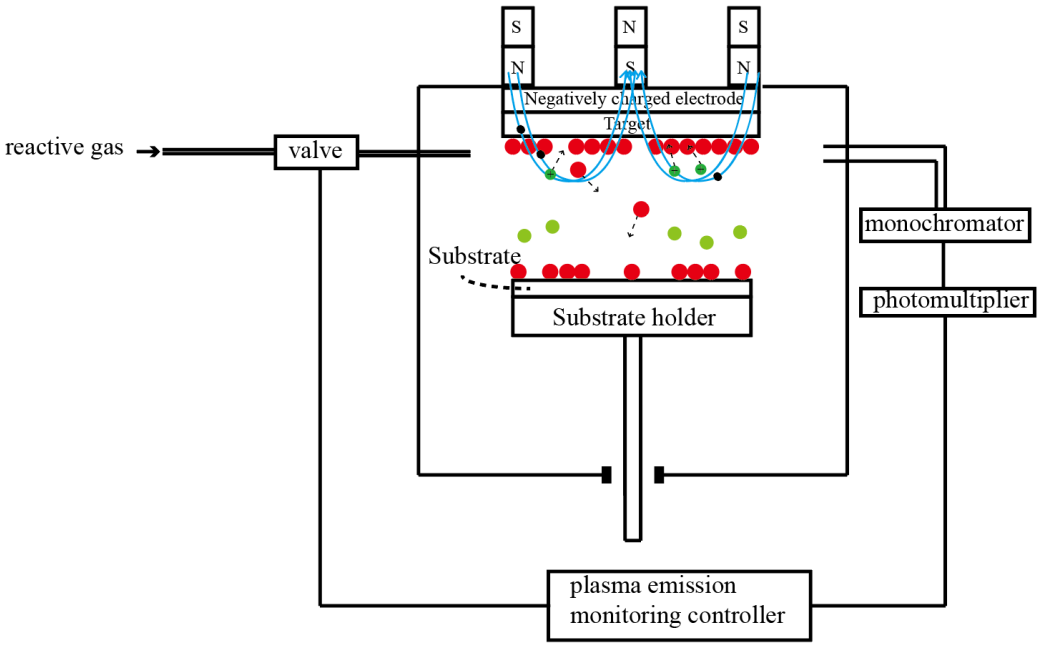

Figure 2.1. Schematic of the magnetron sputtering system used for thin-film deposition. Reproduced from Ref. 4 with permission from Elsevier.

In this system, argon gas (Ar) is introduced into a vacuum chamber, and a DC voltage is applied between the target (cathode) and the substrate (anode) to generate a plasma. The Ar^+ ions are accelerated toward the target surface and eject atoms through momentum transfer, which subsequently condense on the substrate to form a thin film. To enhance the sputtering rate and plasma confinement, a magnetic field is applied behind the target.[2,3] The magnetic field confines electrons near the target surface, thereby

increasing the ionization efficiency of the working gas and maintaining a dense plasma region close to the target.

The sputtering behavior depends strongly on the magnetic nature of the target material. For non-magnetic targets such as Bi, Sb, and BiSb, the external magnetic field penetrates the target efficiently, forming a stable plasma above the surface. In contrast, for magnetic targets such as Co, Fe, and CoFe, the magnetic flux is partially absorbed by the target, weakening the field near the surface. This so-called magnetic short-circuit effect reduces plasma confinement and causes the plasma to shift toward the edges, resulting in a lower sputtering rate and degraded film uniformity.[4,5] To compensate, stronger magnets, optimized magnetic yoke geometries, or RF-assisted power sources are often employed to stabilize the discharge.

In this work, both non-magnetic (BiSb) and ferromagnetic (CoFe) targets were used. Accordingly, sputtering parameters such as discharge power, Ar pressure, and target–substrate distance were optimized individually to ensure uniform thickness and sharp interfaces in the BiSb/CoFe heterostructures.

2.1.2. Deposition Conditions and Multilayer Stack Design

All thin films in this study were deposited using a multi-target magnetron sputtering system with a base pressure of approximately 10^{-7} Pa and a working pressure of about 10^{-4} Pa. High-purity argon was used as the sputtering gas, while oxygen was introduced as a reactive gas when required. The system enables sequential deposition of multiple layers without breaking vacuum, thereby ensuring sharp, contamination-free interfaces[6-8]

To fabricate multilayer structures such as $Bi_{0.85}Sb_{0.15}$/interlayer/$Co_{0.3}Fe_{0.7}$, we used high-purity metal targets including BiSb, CoFe, and Pt. The deposition was performed under typical working pressures of 0.3 - 1.0 Pa, with deposition rates pre-calibrated and film thicknesses confirmed by X-ray reflectivity (XRR).[8-10]

All samples were grown in-situ under vacuum to minimize surface oxidation and maintain interface integrity.

2.2. Structural and Surface Characterization

2.2.1. X-ray Diffraction (XRD): Crystallographic Analysis

XRD is a widely used analytical technique for determining the crystal structure and interatomic spacing of materials.[11-13] When a monochromatic X-ray beam interacts with a crystalline lattice, constructive interference occurs at specific incident angles that satisfy Bragg's law:

$$n\lambda_l = 2d * \sin\theta_B \quad (2.1)$$

Here, n is the diffraction order, λ_l the X-ray wavelength, d the spacing between crystallographic planes, and θ_B the Bragg angle. These diffraction conditions provide the fundamental basis for structural analysis in XRD and form the starting point for understanding the instrumentation and measurement geometries described in the following sections.

(1) X-ray Generation and Monochromatization

Having outlined the fundamental diffraction condition, we now describe the instrumentation used in laboratory XRD measurements. X-rays are generated in an X-ray tube, where a heated tungsten filament emits electrons by thermionic emission. These electrons then sped up using high voltage and hit a metal target (like copper, iron, molybdenum, or chromium), which produces X-rays. When these high-energy electrons strike the target, they eject inner-shell electrons of the target atoms, leading to the emission of characteristic X-ray radiation as outer electrons fall into lower energy states.

The most used X-ray lines are the Kα and Kβ lines. The Kα radiation consists of two components: Kα_1 (shorter wavelength, stronger intensity) and Kα_2 (weaker). Their wavelengths are specific to the target material. For example, Cu Kα radiation (λ_l = 1.5418 Å) is commonly used for diffraction analysis. Since Kα_1 and Kα_2 are very close in wavelength, a weighted average is often used. To obtain a quasi-monochromatic beam suitable for diffraction, unwanted wavelengths are filtered using metal foils or crystal monochromators.

(2) Instrumentation and Diffraction Geometry

A standard XRD system consists of three main components: X-ray tube (source), Sample stage, and X-ray detector.

As illustrated in Figure 2.2, a focused X-ray beam with a single wavelength is directed onto the sample. The sample is mounted on a rotating stage, and the detector is mounted on an arm that rotates simultaneously. The geometry typically follows a θ–2θ configuration, in which: the sample rotates by angle θ, and the detector moves by angle 2θ to capture diffracted rays.[13-15]

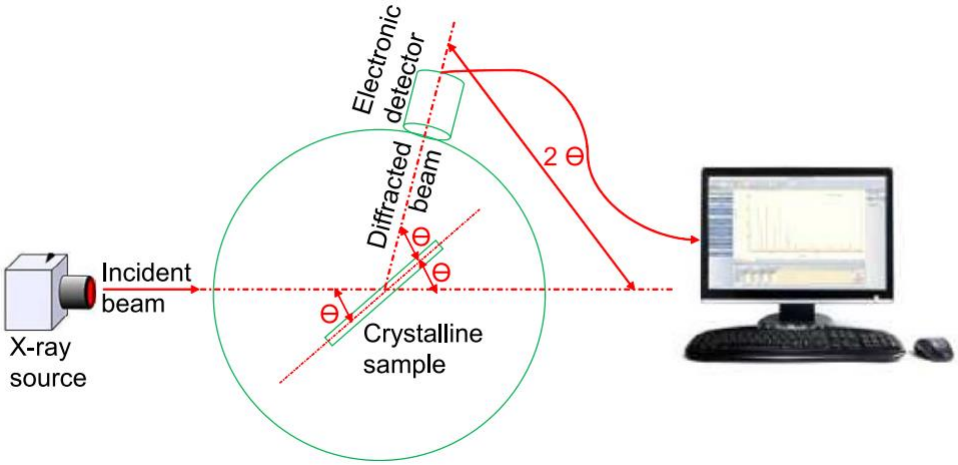

Figure 2.2. Schematic diagram of a typical XRD system in θ-2θ configuration, illustrating the incident beam, sample rotation, diffracted beam, and electronic detection. Reproduced from Ref. 14 with permission from Wiley.

The rotation and alignment of the sample and detector are controlled by a goniometer. When the geometric conditions satisfy Bragg's law, constructive interference occurs, producing distinct diffraction peaks that are detected by the X-ray detector. The detector records the intensity of the diffracted X-rays as a function of angle (2θ) and converts the incoming signal into digital counts for accurate measurement and subsequent data processing.

2.2.2. X-ray Reflectivity (XRR): Thickness and Interface Roughness Evaluation

XRR is a nondestructive method used to analyze the structure of thin films. It can determine key properties such as film thickness, density, surface roughness, and the quality of interfaces.[16-18] In this technique, the reflected X-ray intensity is measured while changing the angle at which the X-rays hit the surface at a shallow (grazing) angle.

When a collimated X-ray beam strikes a thin film at low incident angles, part of the beam is reflected at the surface, while the rest penetrates the film and reflects at internal interfaces, such as the film – substrate boundary. The interference between these reflected beams leads to periodic oscillations in the reflectivity curve, commonly referred to as Kiessig fringes. A schematic diagram illustrating this reflection and interference process is shown in Figure 2.3.

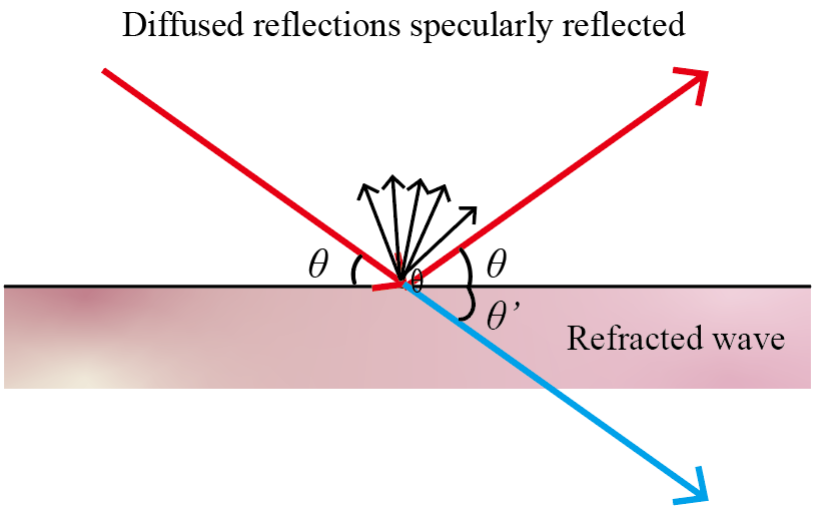

Figure 2.3. Schematic illustration of X-ray reflectivity at grazing incidence, showing specular reflection, diffuse scattering, and refraction into the film.

The shape and features of the XRR curve are strongly influenced by key film properties:

(1) Film thickness determines the oscillation period. Thicker films result in shorter fringe spacing.[16,19]

(2) Density contrast between adjacent layers governs the oscillation amplitude. A higher contrast leads to larger reflectivity modulation.

(3) Surface and interface roughness cause damping of the reflectivity signal. Increased roughness results in faster attenuation of oscillations.[17,20]

(4) Critical angle for total external reflection is related to electron density. Higher density materials exhibit larger critical angles.

XRR is applicable to crystalline, polycrystalline, and amorphous thin films. It enables precise determination of layer thicknesses ranging from a few nanometers to several hundred nanometers and provides essential structural information without damaging the sample.

2.2.3. X-ray Fluorescence (XRF): Elemental Composition Analysis

XRF is a widely used, non-destructive analytical technique for determining the elemental composition of various materials, including solids, powders, and liquids.[21-23] It enables qualitative, semi-quantitative, and quantitative analysis without altering or consuming the sample.

In XRF, a high-energy primary X-ray beam typically generated by an X-ray tube is directed at the sample surface. The incident radiation excites atoms in the material by ejecting electrons from their inner shells through the photoelectric effect. As the atoms return to their ground state, outer-shell electrons fill

the vacancies, emitting characteristic fluorescent X-rays. These emissions are element-specific, serving as unique "fingerprints" that allow for precise elemental identification.

The detected fluorescence provides two key types of information:

(1) The energy of the emitted X-rays identifies the elements present (qualitative analysis).

(2) The intensity of each emission correlates with its concentration (quantitative analysis).

XRF can detect elements ranging from fluorine to uranium, with detection limits of approximately 0.5 ppm for heavy elements (e.g., Mo) and around 100 ppm for lighter ones, depending on instrument configuration and matrix effects. A schematic diagram illustrating the XRF principle is shown in Fig. 2.4.

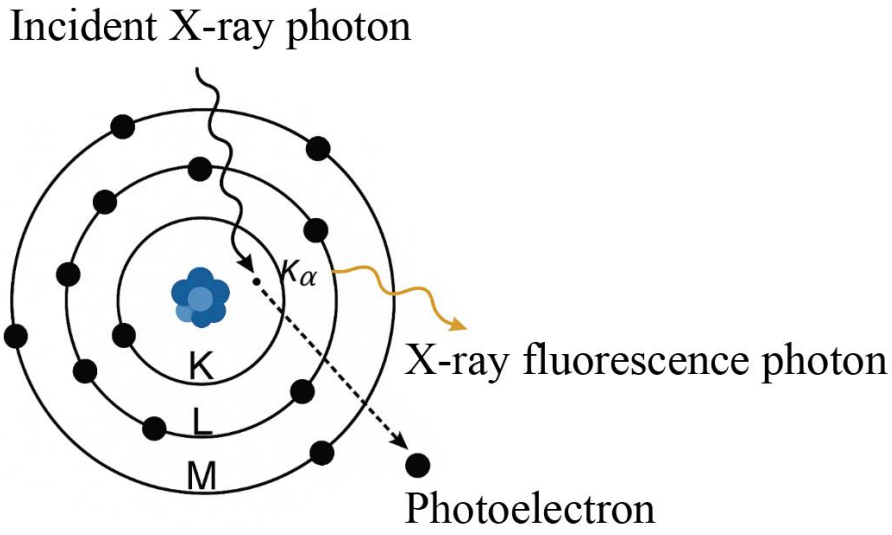

Figure 2.4. Schematic diagram of the XRF process. An incident X-ray photon ejects an inner-shell electron, and the resulting electronic transition emits a characteristic fluorescence photon.

Because of its broad elemental coverage, high sensitivity, and rapid measurement capability, XRF is used across a wide range of applications from trace element analysis in scientific research, to process control in industrial environments such as cement production, metallurgy, geology, and environmental monitoring.[23-25] Its ability to deliver reliable results without sample preparation or damage makes it an invaluable tool in both laboratory and field-based investigations.

2.2.4. Atomic Force Microscopy (AFM): Surface Topography and Roughness

AFM is a versatile surface characterization technique that has been extensively applied in materials science, biology, chemistry, and nanotechnology since its invention in the 1980s. It enables high-resolution imaging of both conductive and insulating surfaces, with spatial resolution down to the atomic scale.[26-30]

In a typical AFM system, the sample is mounted on a piezoelectric scanner stage, and a cantilever with a sharp probe tip scans across the surface. The cantilever deflection caused by interaction forces—such as van der Waals, electrostatic, or magnetic forces—is monitored by detecting the reflection of a laser beam onto a photodiode detector. From these deflection signals, a three-dimensional surface topography is reconstructed as schematically illustrated in Figure 2.5.

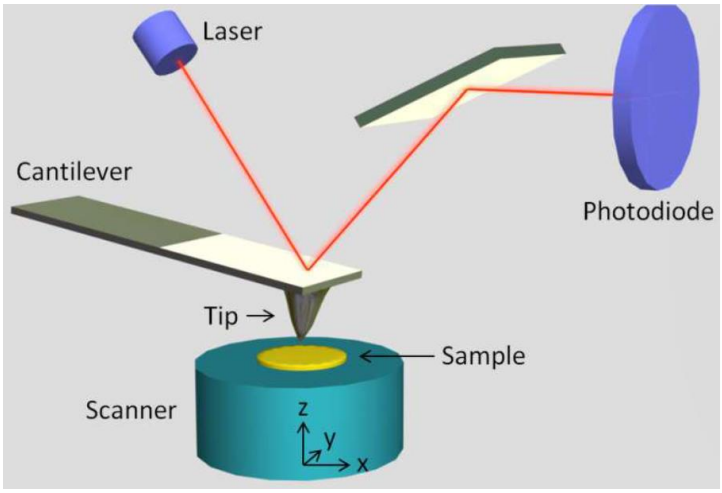

Figure 2.5. Schematic illustration of an AFM showing the laser detection system and tip-sample interaction. Reproduced from Ref. 29 with permission from Springer Nature.

AFM can operate mainly in two modes: contact mode and non-contact mode. In contact mode, the probe maintains continuous contact with the surface, and topographic information is obtained directly from the cantilever deflection. In non-contact mode, the cantilever oscillates near its resonance frequency at a small distance from the surface, and variations in the oscillation amplitude or frequency are used to sense surface topography. Non-contact mode is particularly advantageous for thin films or soft materials, as it minimizes tip-induced deformation, reduces shear forces, and prevents surface damage while preserving nanoscale resolution.

In this study, AFM was employed to analyze the surface morphology and roughness of the fabricated thin films, providing quantitative evaluation of surface roughness and nanoscale topographical features.

2.3. Device Fabrication Techniques

2.3.1. Photolithography for Pattern Transfer

To fabricate patterned spintronic devices, we employed a standard photolithography process following the deposition of continuous multilayer films onto insulating substrates (Si/SiO_2). The patterning process enables selective definition of device regions for subsequent etching.[31-33]

First, a layer of positive photoresist was spin-coated onto the film surface and soft-baked to remove solvent residues. The sample was then exposed to ultraviolet light using a maskless lithography system (PALLET DDB-701), which precisely defines the desired device geometry.[34,35]

After exposure, the resist was developed in a dedicated developer solution, removing the exposed areas and forming a patterned mask on top of the film. This resist mask protects the designated regions during the dry etching step (Section 2.3.2), where the unprotected areas are removed by ion milling. Finally, the remaining photoresist was stripped to complete the photolithographic pattern transfer.

A schematic diagram of the photolithography and etching sequence is shown in Figure 2.6.

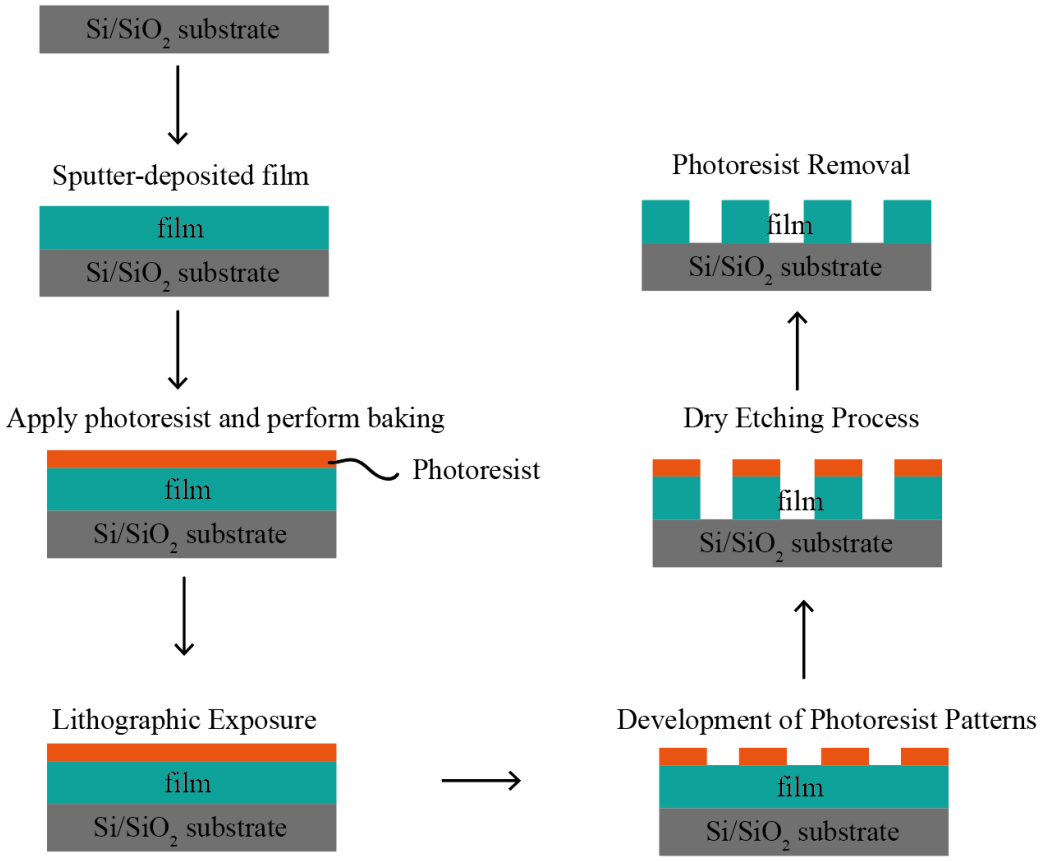

Figure 2.6. Schematic illustration of the standard photolithography process, including film deposition, photoresist coating, baking, exposure, development, dry etching, and photoresist removal.

2.3.2. Ion Milling: Pattern Transfer and Etching Depth Control

After photolithography, the resist-defined pattern was transferred into the underlying thin films by ion milling. This technique removes material through physical sputtering, in which energetic Ar^+ ions bombard the exposed film surface. When the incident ions strike the surface, their kinetic energy is transferred to surface atoms through a cascade of momentum-exchange collisions, ejecting atoms from the target layer and generating secondary electrons and other emitted particles, as illustrated in Figure 2.7. This sputtering mechanism has been extensively studied in classical ion–solid interaction models.[36-38]

Because ion milling is governed purely by physical interactions without chemical reactions, the etching rate depends primarily on the ion energy, incidence angle, and the material's surface binding energy.[39] Under optimized conditions, the process provides excellent control of etch depth and sidewall

definition, making it particularly suitable for patterning metallic and magnetic multilayers where structural precision is essential.[40]

During processing, the resist mask protects the covered regions, while the unmasked areas are gradually removed by continuous sputtering. After ion milling, the remaining resist is stripped to obtain well-defined device structures.

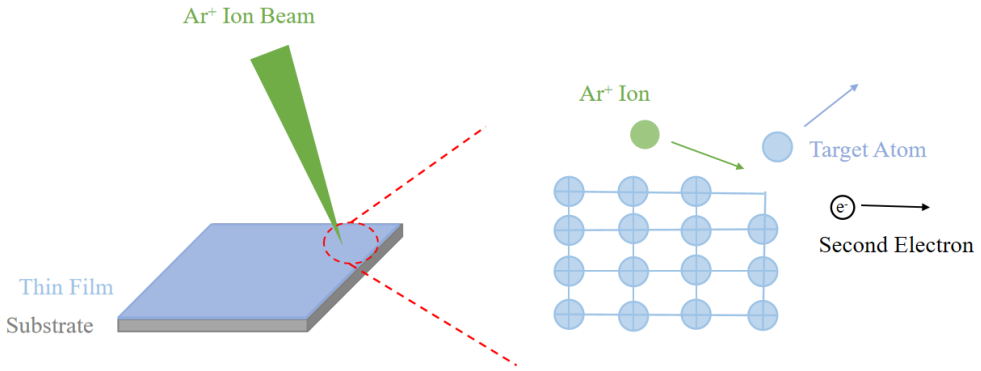

Figure 2.7 Schematic of the ion-milling process, where energetic Ar^+ ions bombard the film surface, sputtering surface atoms and generating secondary electrons. Continuous ion impact removes the exposed material and enables pattern transfer.

2.4. Electrical Measurement Systems

2.4.1. Magnetoresistance and Harmonic Signal Measurements (Including SMR, AMR, AHE, Second Harmonic Hall, and Spin Accumulation)

In order to investigate the spin transport and magnetoresistive properties of the fabricated TI/FM heterostructures, a series of electrical measurements were carried out, including AHE, AMR, SMR, second harmonic Hall voltage, and spin Hall resistance. These effects reflect distinct physical mechanisms involving spin-orbit coupling, magnetization orientation, and spin accumulation at interfaces. The physical principles underlying these effects have been described in Chapter 1.

All measurements were performed on photolithographically defined Hall bar structures, except for the direct spin Hall (DSH) measurement, which utilized a pillar-type geometry optimized for detecting transverse voltage signals. The experimental setup incorporated precision current sources, nanovoltmeters, a lock-in amplifier, and programmable magnetic-field control.

(1) AHE Measurement

AHE measurements were conducted using a standard four-probe configuration. A constant direct current was applied along the x-axis using a Keithley 2450 Source Meter, and an out-of-plane magnetic field (H_z) was swept using a high-current bipolar power supply (TM-PSBC 3070-234-S2, ±70 V / ±30 A) controlled via a GPIB interface module (Takasago AP-1 628T2). The longitudinal voltage (V_{xx}) and transverse Hall voltage (V_{xy}) were measured simultaneously using an ADCMT 7461A Digital Multimeter and converted into resistance values R_{xx} and R_{xy} by dividing by the applied current. This configuration enabled extraction of both the ordinary Hall effect and the anomalous contribution originating from spin-dependent scattering.

(2) Second Harmonic Hall Measurement

To evaluate spin-orbit torque-induced effects, we employed a low-frequency harmonic measurement technique. An alternating current of 259.68 Hz was sourced along the x-axis using a Keithley 6221 AC/DC current source, and the second harmonic voltage ($V_{2\omega}$) across the transverse direction was detected using a NF LI5650 Digital Lock-in Amplifier. A magnetic field was applied along the current direction to allow separation of damping-like and field-like torque contributions. This method enables quantitative analysis of spin-orbit torque efficiency through harmonic decomposition.

(3) AMR Measurement

AMR measurements were carried out by injecting a DC current along the x-axis with the Keithley 2450, while rotating the magnetic field in the x-z plane. The variation in longitudinal resistance R_{xx} as a function of the angle between the magnetization and the current direction was recorded using the ADCMT 7461A. This allowed evaluation of the AMR ratio and the angular dependence characteristic of the ferromagnetic layer.

(4) SMR Measurement

The SMR was measured using a similar configuration as AMR, but with the magnetic field rotated in the y-z plane. A DC current was applied along the x-axis, and the change in R_{xx} was recorded as the magnetization was swept from in-plane to out-of-plane directions. This measurement probes the modulation of spin absorption and spin-current reflection at the TI/FM interface, governed by spin mixing conductance and interfacial transparency, rather than by bulk magnetoresistive effects. Measurements were performed using the Keithley 2450 and ADCMT 7461A, with magnetic field control as described above.

(5) Spin accumulation (SA) Measurement

To further investigate spin current generation and detection, we fabricated a custom-designed pillar device structure in which a current was sourced along the x-axis while an in-plane magnetic field (H_y) was swept. The voltage between the FM layer and the SOT layer along the perpendicular (z) direction was recorded to detect the spin accumulation signal. A DC current from the Keithley 2450 was used, and the voltage was measured via high-impedance differential input on the ADCMT 7461A. The magnetic field was again supplied by the programmable bipolar power source.

All instruments were connected through a centralized GPIB communication bus and controlled using custom VB-based software for automated voltage-current sweeps, lock-in signal acquisition, and synchronized magnetic field scanning.

2.4.2. Temperature Control and Magnetic Field Configuration

To comprehensively investigate the magnetic and spin transport properties of the fabricated multilayer devices, AMR, SMR, second-harmonic resistance, and spin accumulation measurements were performed over a temperature range from 50 K to 300 K. Measurements at room temperature were carried out to evaluate the potential for practical applications such as spin-based memory and information storage devices. In contrast, low-temperature measurements were used to elucidate intrinsic scattering mechanisms, interfacial spin transmission, and the temperature dependence of spin–orbit–coupled transport.

Temperature control was achieved using a closed-cycle helium cryostat equipped with a resistive heater and calibrated temperature sensor, enabling stable and precise regulation across the entire temperature range. All measurements were conducted under high-vacuum conditions to suppress thermal noise and prevent sample degradation.

A single-axis vector magnet was employed to apply magnetic fields. The sample mount and electromagnet stage allowed magnetic field rotation in arbitrary planes, enabling detailed angular-dependent measurements. The magnetic field strength was selected according to the measurement type: an in-plane field of 2 kOe was applied for spin Hall resistance measurements to resolve subtle spin accumulation signals, while stronger fields of up to 9 kOe were used in second-harmonic, SMR, and AMR experiments to ensure magnetic saturation and clear angular modulation.

This combined temperature–field configuration enabled systematic analysis of the evolution of spintronic effects with respect to temperature and magnetic field direction, providing critical insights into the stability and physical origin of the observed signals.

2.5. Reference

1. J. A. Thornton, J. Vac. Sci. Technol. A 4, 3059 (1986).
2. D. M. Mattox, Handbook of Physical Vapor Deposition (PVD) Processing (William Andrew Publishing, Norwich, 2010).
3. W. D. Westwood, J. Vac. Sci. Technol. 15, 1 (1978).
4. Musil, J., Baroch, P., Vlček, J., Nam, K. H., & Han, J. G. Thin solid films, 475(1-2), 208-218 (2005).
5. R. L. Boxman, D. M. Sanders, and P. J. Martin (Eds.), Handbook of Vacuum Arc Science and Technology (Noyes Publications, Park Ridge, NJ, 1995).
6. R. F. Bunshah (Ed.), Handbook of Deposition Technologies for Films and Coatings: Science, Technology, and Applications, 2nd ed. (Noyes Publications, Park Ridge, NJ, 1994).
7. D. Manova, J. W. Gerlach, and S. Mändl, Materials 3, 4109 (2010).
8. J. E. Greene, J. Vac. Sci. Technol. A 26, 1105 (2008).
9. S. Mahieu and D. Depla, J. Phys. D: Appl. Phys. 42, 053002 (2009).
10. S. Berg and T. Nyberg, Thin Solid Films 476, 215 (2005).
11. B. D. Cullity and S. R. Stock, Elements of X-ray Diffraction, 3rd ed. (Prentice Hall, Upper Saddle River, NJ, 2001).
12. H. P. Klug and L. E. Alexander, X-ray Diffraction Procedures: For Polycrystalline and Amorphous Materials, 2nd ed. (Wiley, New York, 1974).
13. C. Suryanarayana and M. G. Norton, X-ray Diffraction: A Practical Approach (Springer, Boston, 1998).
14. H. Khan, A. S. Yerramilli, A. D'Oliveira, T. L. Alford, D. C. Boffito, and G. S. Patience, Can. J. Chem. Eng. 98, 1255 (2020).
15. B. E. Warren, X-ray Diffraction (Dover Publications, New York, 1990).
16. L. G. Parratt, Phys. Rev. 95, 359 (1954).

17. J. Daillant and A. Gibaud (Eds.), X-ray and Neutron Reflectivity: Principles and Applications (Springer, Berlin, 1999).
18. M. Tolan, X-ray Scattering from Soft-Matter Thin Films (Springer, Berlin, 1999).
19. P. H. Fuoss, J. Appl. Phys. 71, 548 (1992).
20. J. Als-Nielsen and D. McMorrow, Elements of Modern X-ray Physics (Wiley, New York, 2011).
21. R. Jenkins, X-ray Fluorescence Spectrometry, 2nd ed. (Wiley-Interscience, New York, 1999).
22. J. Mantler and M. Schreiner, X-ray Spectrom. 29, 3 (2000).
23. R. Van Grieken and A. Markowicz (Eds.), Handbook of X-ray Spectrometry, 2nd ed. (Marcel Dekker, New York, 2002).
24. C. Streli, P. Wobrauschek, and P. Kregsamer, Spectrochim. Acta B 56, 933 (2001).
25. B. Beckhoff, B. Kanngießer, N. Langhoff, R. Wedell, and H. Wolff (Eds.), Handbook of Practical X-ray Fluorescence Analysis (Springer, Berlin, 2006).
26. G. Binnig, C. F. Quate, and C. Gerber, Phys. Rev. Lett. 56, 930 (1986).
27. P. Eaton and P. West, Atomic Force Microscopy (Oxford University Press, Oxford, 2010).
28. B. Bhushan, Springer Handbook of Nanotechnology (Springer, Berlin, 2010).
29. Zeng G, Duan Y, Besenbacher F, et al. Atomic Force Microscopy Investigations into Biology-From Cell to Protein, 2012.
30. H.-J. Butt, B. Cappella, and M. Kappl, Surf. Sci. Rep. 59, 1 (2005).
31. S. Wolf and R. N. Tauber, Silicon Processing for the VLSI Era, Vol. 1: Process Technology (Lattice Press, Sunset Beach, 1986).
32. H. J. Levinson, Principles of Lithography, 3rd ed. (SPIE Press, Bellingham, 2010).
33. C. A. Mack, Fundamental Principles of Optical Lithography: The Science of Microfabrication (Wiley, Chichester, 2007).
34. A. Chuvilin, A. H. Tavabi, and U. Kaiser, Micron 43, 1243 (2012).
35. H. Fujita, Sens. Actuators A 200, 2 (2013).
36. J. W. Coburn and E. Kay, J. Appl. Phys. 43, 4965 (1972).
37. R. Behrisch and W. Eckstein (Eds.), Sputtering by Particle Bombardment (Springer, Berlin, 2007).
38. J. A. Thornton, J. Vac. Sci. Technol. 15, 171 (1978).
39. G. Carter and J. S. Colligon, Ion Bombardment of Solids (Elsevier, Amsterdam, 1968).
40. A. L. Thomann, P. Brault, J. Mathias, and J. Durand, Surf. Coat. Technol. 200, 535 (2005).

Chapter 3 Direct Spin Hall effect Magnetic Field Sensor: Demonstration of the Operating Principle and Noise Analysis

This chapter investigates the underlying mechanisms that contribute to the giant signal observed in the direct spin Hall (DSH) magnetic field sensor compared to second harmonic techniques, while analyzing the noise limitations inherent to DSH sensing. A comparative study with ISH sensing is conducted to evaluate signal-to-noise characteristics, scalability, and practical implications for next-generation magnetic read heads.

3.1. Introduction and Motivation

The manipulation and read-out of magnetization states in FM materials are two fundamental operations in spintronic devices. In high-density MRAM, magnetization is commonly manipulated via STT, while read-out is achieved through the TMR effect. Recently, the SHE in non-magnetic materials with strong spin-orbit coupling has emerged as a powerful alternative method for both writing and reading magnetic states.

Among the various manifestations of SHE, the DSH has been intensively studied in the context of SOT-MRAM, where it enables current-induced manipulation of magnetization without the need for direct current injection into magnetic layers.[1-3] Notably, DSH-based SOT has demonstrated the ability to manipulate magnetic insulators, which is unattainable via conventional STT approaches[4]. Conversely, its reciprocal phenomenon the ISH has attracted attention as a potential mechanism for reading magnetic states in magnetoelectric spin-orbit logic devices[5,6] and in magnetic read head sensors for HDDs[7].

Huy et al. recently demonstrated a proof-of-concept ISH magnetic field sensing device using a CoFe/MgO/BiSb heterostructure[8]. In this device, a spin-polarized current injected perpendicularly from the CoFe layer into the BiSb topological insulator is converted into a measurable voltage via the ISH effect. The device offers several advantages over TMR-based sensors: it requires only a single FM layer,

thus eliminating complex reference layer stacks, and avoids spin-transfer noise owing to the non-magnetic nature of BiSb. Moreover, thanks to the large spin Hall angle of BiSb, a SNR exceeding 28 dB has been achieved, which is suitable for HDD read head applications.

From a materials perspective, topological quantum materials particularly topological insulators such as BiSb are highly attractive for spin Hall applications due to their potentially enormous spin Hall angles[9-11], far exceeding those of conventional heavy metals (typically $\theta_{SH} < 1$). These materials have also demonstrated operation well above room temperature[12-14] and can be integrated into devices via industry-compatible sputtering techniques[15,16]. BiSb, in particular, exhibits an ultralarge spin Hall angle ≈ 52 when fabricated by molecular beam epitaxy[17], and similarly high performance has been achieved using sputtering a method more favorable for industrial-scale device integration.

In this work, we investigate an alternative magnetic field sensing device in which the DSH rather than the ISH is used to detect the magnetic state in a BiSb/interfacial layer/CoFe heterostructure. Our motivation is three-fold. First, by comparing the output signals of DSH and ISH under identical structural and material conditions, we aim to verify the reciprocity between these two effects in BiSb-based devices, assuming the interfacial layer is sufficiently transparent to both pure spin currents and spin-polarized charge currents. Second, the DSH configuration enables direct estimation of the θ_{SH} from the output signal, allowing for meaningful comparison with values obtained using conventional methods such as the second harmonic Hall technique[18]. Third, we seek to elucidate the differences in the origin of noise between DSH- and ISH-based devices, particularly focusing on the contribution of spin-transfer noise in DSH measurements.

3.2. Device Structures and Measurement Methods

3.2.1. Multilayer Stack Design and Structural Characterization

The sensor device investigated in this study is based on a multilayer heterostructure fabricated using magnetron sputtering. As illustrated in Figure 3.1, the stack consists of a 3.8 nm buffer layer, a 9.7 nm BiSb layer, a 1.1 nm interfacial layer, a 0.8 nm CoFe FM layer, and a 5.5 nm capping layer.

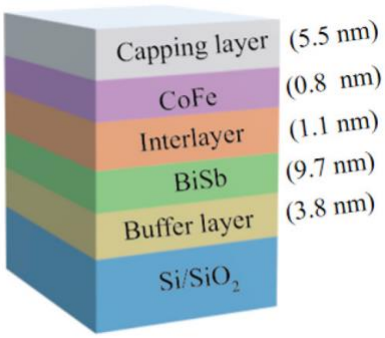

Figure 3.1. Schematic diagram of the multilayer stack used in this work.

The thicknesses of the individual layers were determined from XRR measurements, as shown in Figure 3.2. A good agreement between the experimental data (black curve) and the fitting result (red curve) was obtained, yielding the following layer thicknesses: 3.8 nm (buffer), 9.7 nm (BiSb), 1.1 nm (interfacial), 0.8 nm (CoFe), and 5.5 nm (capping). The root-mean-square surface roughness of the capping layer was estimated to be 5.4 Å.

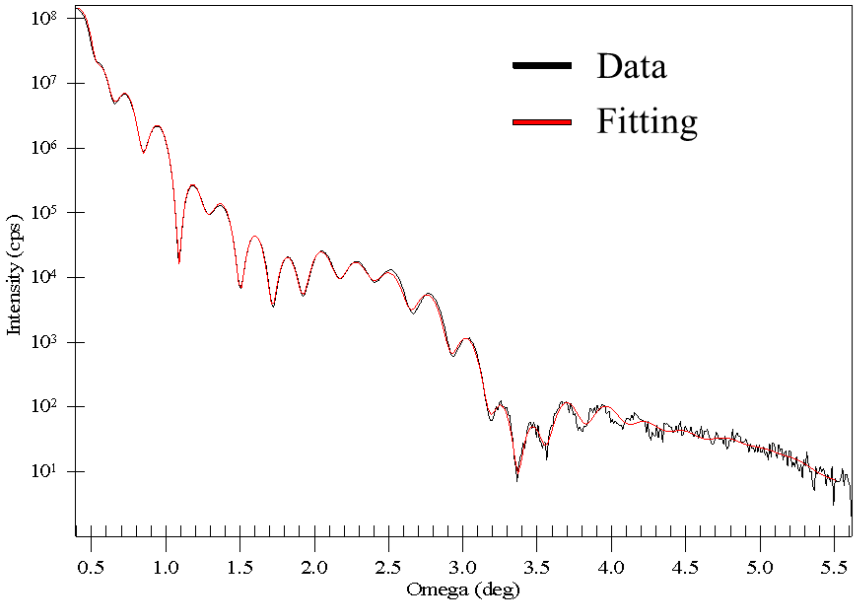

Figure 3.2. XRR spectrum of the full stack. The black curve represents the experimental data, while the red curve corresponds to the best-fit simulation.

To further verify the surface morphology and validate the XRR-derived roughness, AFM was performed on the as-deposited multilayer surface. As shown in Figure 3.3, the measured root-mean-square (RMS) roughness was approximately 3.9 ± 0.3 Å, which is in good agreement with the XRR fitting result. This indicates the surface is sufficiently smooth and free of significant contamination, ensuring high interface quality throughout the stack.

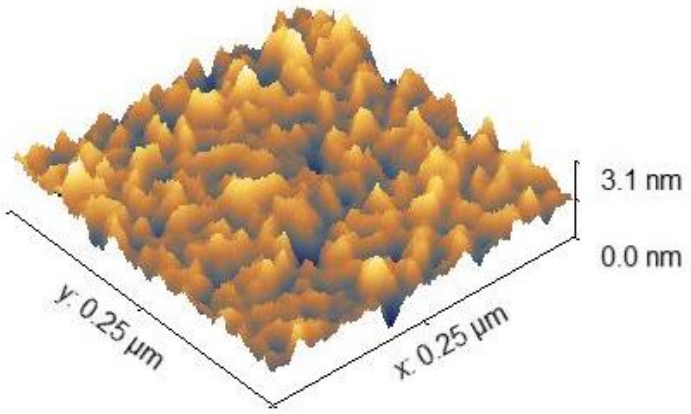

Figure 3.3. Representative AFM scan of the as-deposited multilayer surface. The RMS roughness was measured to be 3.9 ± 0.3 Å over a 0.25 µm × 0.25 µm area.

The buffer layer is designed to promote the growth of BiSb with (012) orientation. According to the structural scheme disclosed in Ref. 19, it comprises three sublayers: a pre-seed layer to ensure adhesion to the Si/SiO_2 substrate, a seed layer, and a crystalline layer made of face-centered cubic materials with (111) orientation and in-plane lattice constants ranging from 3.52 to 3.71 Å. The BiSb alloy has a nominal composition of $Bi_{85}Sb_{15}$. As shown in Figure 3.4, XRD analysis confirms that the BiSb layer crystallizes primarily in the (012) orientation, with a minor (001) component. The presence of clear fringes around the BiSb (012) peaks indicates excellent wafer-scale thickness, uniformity and interfacial flatness.

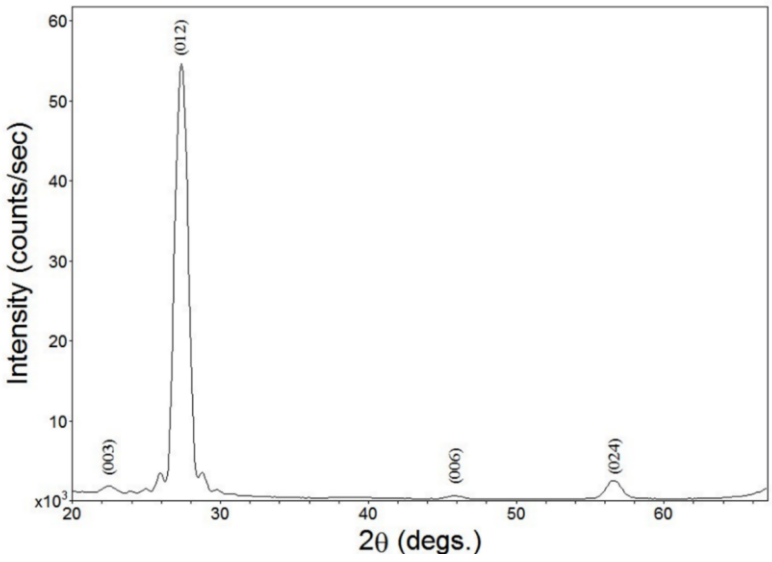

Figure 3.4. XRD pattern of the multilayer structure. The dominant BiSb (012) peak confirms the intended crystal orientation, with weak (001) components also observed.

The interfacial layer serves as a diffusion barrier to prevent Sb out-diffusion from the BiSb layer into the FM layer, while remaining sufficiently thin to maintain transparency to both pure spin currents and spin-polarized charge currents. The CoFe layer, with a nominal composition of $Co_{30}Fe_{70}$, is kept intentionally thin to enable reliable second harmonic Hall effect (2ω Hall) measurements of spin–orbit torque. The capping layer, composed of high-resistivity materials, protects the CoFe from oxidation and suppresses shunting of the in-plane bias current.

3.2.2. Fabrication and Operation of the Hall Bar Device for AHE and Second Harmonic Measurements

To evaluate the SHE in the BiSb-based heterostructure, we fabricated a Hall bar device suitable for both AHE and second harmonic Hall measurements. The fabrication followed the process flow described in Section 2.3.1. The device consists of a full multilayer stack with a thin CoFe layer (0.8 nm), optimized to enhance the sensitivity to spin-orbit torque signals. A six-terminal Hall bar pattern with a size of 10 × 25 μm^2 was defined using optical lithography and ion milling. The contact electrodes were formed by sputtering Ta (20 nm)/Pt (10 nm) and patterned by lift-off.

An optical image of the fabricated Hall bar and the coordinate system used in harmonic measurements are shown later in Figure 3.10. During the measurements, an alternating current was applied along the x-axis, and the Hall voltages were measured between the transverse terminals while sweeping external magnetic fields along the x or z directions (denoted as H_x and H_z).

This device allows us to extract the spin Hall angle by analyzing the second harmonic Hall resistance $R_H^{2\omega}$, which reflects the damping-like spin-orbit torque induced by the SHE in the BiSb layer. The detailed measurement results, data fitting procedure, and estimation of the effective spin Hall angle are discussed in Section 3.3.

3.2.3. Fabrication and Operation of the DSH Sensing Device

To fabricate the DSH sensing device, we first patterned a Hall bar structure across the full multilayer stack using optical lithography and ion milling. Figure 3.5 illustrates the overall fabrication process flow, including lithography, etching, and electrode formation, which are described in detail below. The Hall bar has a width of w_H = 50 μm and includes two Hall terminals. The lithography process began by spin-coating a PMGI positive photoresist, followed by a soft bake at 150 °C for 5 minutes. A second layer of

OFPR positive photoresist was then applied and baked at 110 °C for 90 seconds. After exposure and development, ion milling was used to etch through the full multilayer stack down to the substrate, thereby defining the Hall bar pattern.

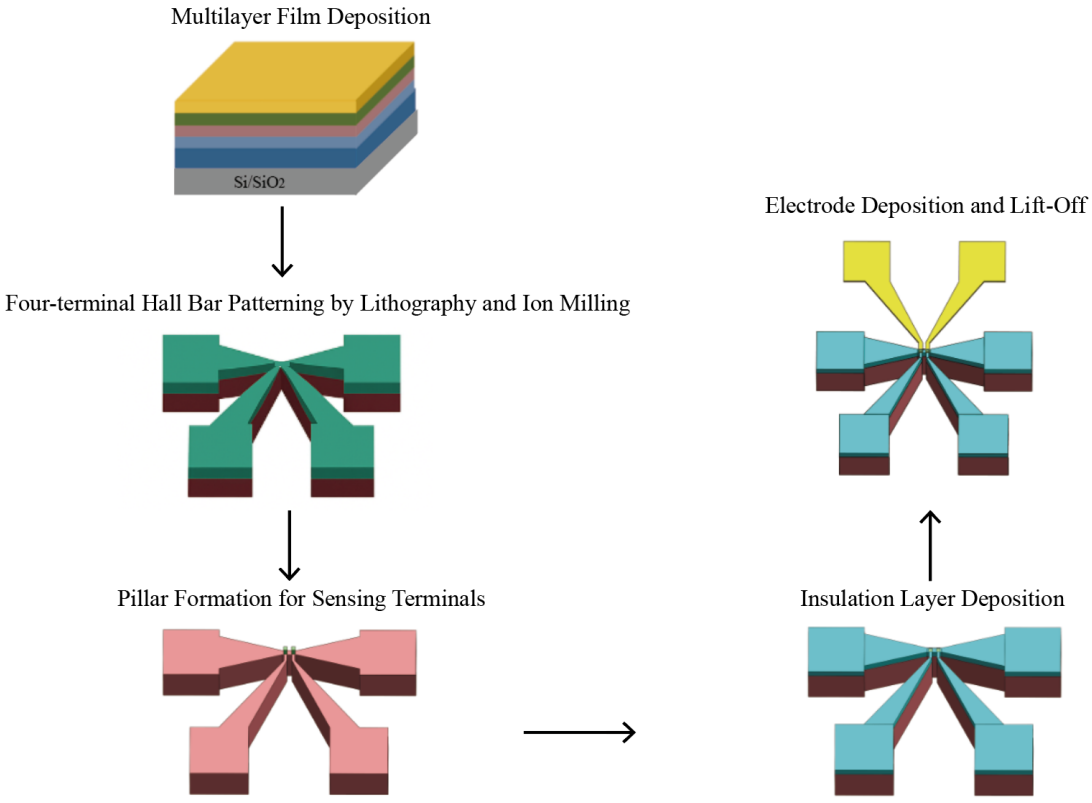

Figure 3.5. Fabrication steps of the DSH sensing device: film deposition, Hall bar patterning, pillar formation, insulation layer deposition, and electrode lift-off.

Subsequently, two square-shaped photoresist masks with $w = 40$ μm were defined on the Hall bar at the locations of the two Hall terminals using the same PMGI/OFPR bilayer process. These masks were used to create sensor pillars. Ion milling was then performed again, this time with controlled milling duration to stop precisely at the BiSb surface, thus leaving pillars composed of interlayer/CoFe/cap layers atop the BiSb track.

To calibrate the ion milling depth for precise pillar formation, we conducted a two-step verification using XRF and AFM. First, we prepared a test sample and monitored the reduction of element-specific peak intensities (Bi) as a function of milling time using XRF. As shown in Figure 3.6, the Bi signal originating from the bottom BiSb layer, remains relatively high for short milling durations and drops

significantly beyond 80 seconds. The optimal etching window was identified between 80-95 seconds, ensuring complete removal of the upper layers while preserving the underlying BiSb.

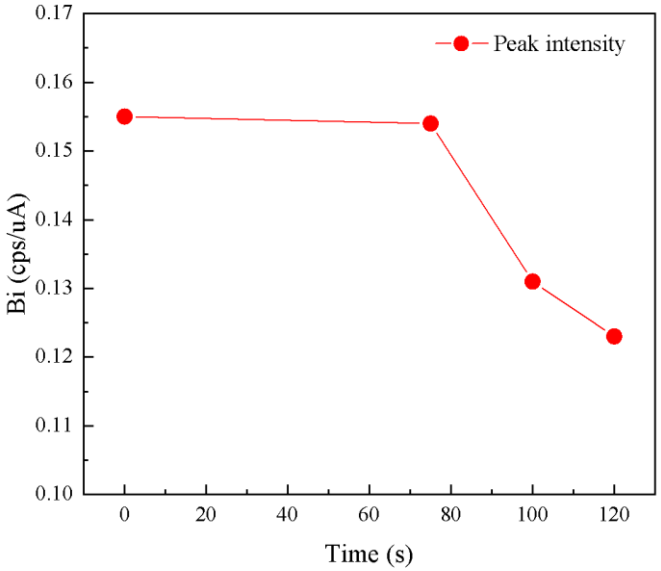

Figure 3.6. XRF Bi peak intensity as a function of milling time.

To further evaluate the etch depth and ensure consistent removal of the capping and ferromagnetic layers, we fabricated reference test structures consisting of an array of 5 μm × 5 μm square mesas, as shown in Fig. 3.7 (a). These mesas were etched using a controlled ion milling process with durations ranging from 80 to 100 s in 5 s increments. AFM was then performed to assess the remaining stack thickness after etching. A representative line profile from a 100-second-etched sample is presented in Fig. 3.7 (b), showing a step height of approximately 6.5 nm. Given that the designed ferromagnetic layer is located ~ 6 nm beneath the capping layer, this result confirms that the 100-second etching condition is sufficient to completely remove both the cap and ferromagnetic layers, providing clean exposure of the underlying topological insulator surface.

(a) (b)

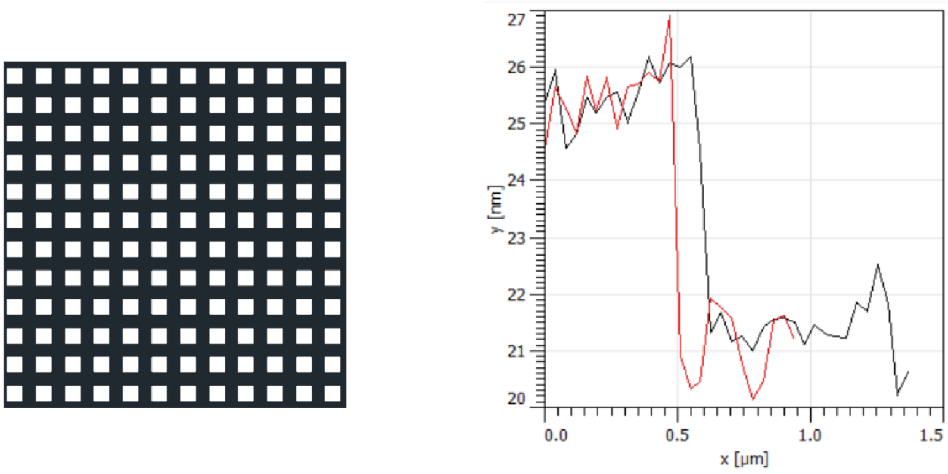

Figure 3.7. (a) Optical image of the fabricated array of 5 µm × 5 µm mesas designed for AFM calibration. (b) AFM line profile after 100 s ion milling, showing a ~6.5 nm step height, confirming complete removal of the capping and ferromagnetic layers.

After pillar milling, an insulating layer was formed by spin-coating a negative OMR photoresist, which was baked at 90 °C for 20 minutes prior to exposure, followed by a hard bake at 150 °C for 5 minutes after development. Finally, Ta (20 nm)/Pt (10 nm) electrodes were deposited via sputtering and patterned by lift-off using the same PMGI/OFPR photoresists.

Figures 3.8 (a) and 3.8 (b) show an optical image and the schematic structure of the final DSH device. In operation, a DC current I_{DC} is applied along the x-axis. Due to the spin Hall effect in BiSb, spin accumulation occurs at the BiSb/interlayer/CoFe interface, resulting in an interfacial electrochemical potential difference that is sensitive to the magnetization direction of the CoFe layer. When an external magnetic field H_y aligns the magnetization along +y or −y, the corresponding spin alignment leads to a measurable interface voltage V_{DSH}. This voltage is recorded between the top electrode on the pillar and the bottom BiSb layer while sweeping H_y.

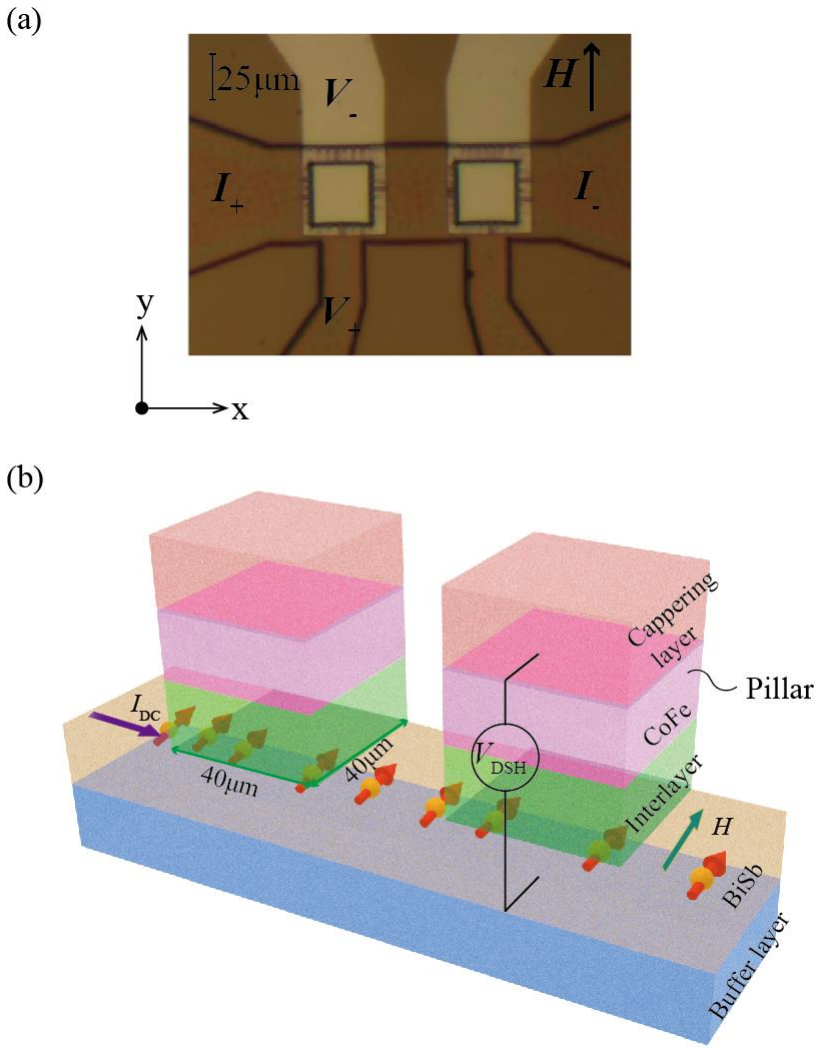

Figure 3.8. Schematic illustration of (a) An optical image of a fabricated DSH device. (b) the direct spin Hall sensor device structure and the measurement setup.

3.3. Experimental Results and Analysis

3.3.1. Evaluation of Spin Hall Angle from Second Harmonic Hall Measurements

Figure 3.9 presents an optical image of the fabricated Hall bar device, along with the schematic of the second harmonic Hall measurement setup. The external magnetic field H was applied either along the x-axis or z-axis, corresponding to in-plane (H_x) and out-of-plane (H_z) configurations, respectively.

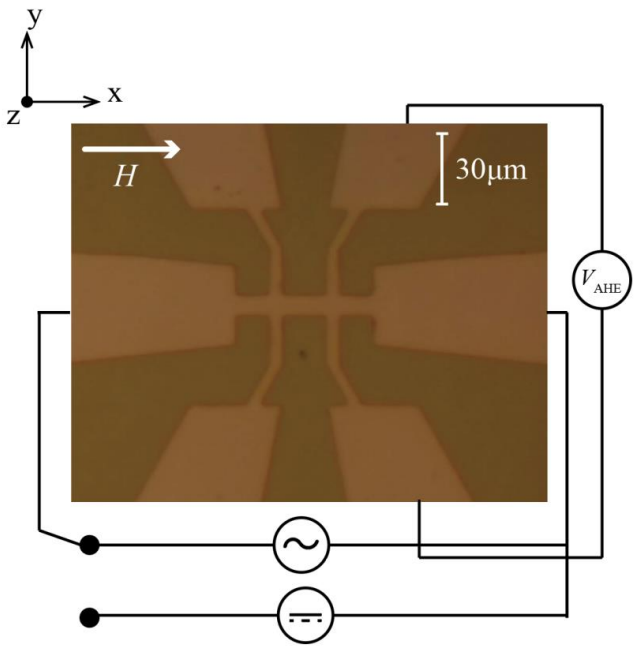

Figure 3.9. Optical microscope image of the Hall bar device and schematic of the second harmonic Hall measurement. The coordinate system and in-plane magnetic field H // x are indicated.

To characterize the magnetic properties of the device, we first measured the anomalous Hall resistance R_{AHE} under a sweeping H_z, as shown in Fig. 3.10. The resulting curve displays a clear saturation behavior, from which we determined the anomalous Hall resistance R_{AHE} = 2Ω and the effective anisotropy field H_k = 7 kOe.

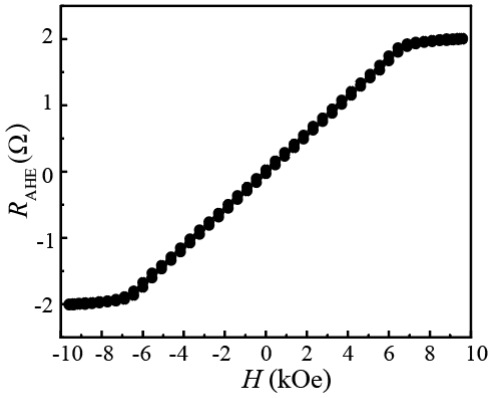

Figure 3.10. The anomalous Hall resistance measured with a perpendicular external magnetic field.

Next, we performed the second harmonic Hall measurements to quantify the damping-like SOT arising from the absorption of SHE-generated spin current in the BiSb layer. An AC current (259.68 Hz)

was applied while sweeping H_x between ±9 kOe, and the corresponding second harmonic Hall resistance $R_H^{2\omega}$ was recorded, as shown in Fig. 3.11. The signal was fitted using the standard second harmonic model, which includes parasitic thermoelectric terms originating from the ordinary Nernst effect (ONE), the ANE, and the spin Seebeck effect (SSE), allowing the extraction of the anti-damping-like effective field H_{AD}.

Figure 3.12 summarizes H_{AD} as a function of J_{BiS}. A linear fit yields an effective spin Hall angle $\theta_{SH}^{eff} = \frac{2e}{\hbar} t_{FM} M_S \frac{\partial H_{AD}}{\partial J_{BiSb}} \sim 3.5$ based on the relation:

$$R_H^{2\omega} = \frac{R_{AHE}}{2} \frac{H_{AD}}{H_x + H_k} + R_{ONE} H_x + R_{ANE+SSE} \quad (3.1)$$

where R_{AHE} is the anomalous Hall resistance amplitude, t_{FM} = 0.8 nm is the CoFe thickness, and M_S = 1850 emu/cm^3 is the saturation magnetization.

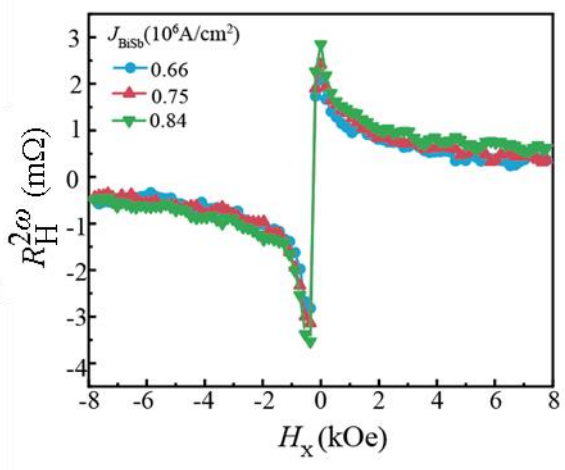

Figure 3.11. The second harmonic Hall resistance measured by different BiSb current densities J_{BiSb}.

To estimate J_{BiSb}, we initially assumed the conductivity of BiSb as σ_{BiSb} = 1.5×10^5 Ω^{-1}m^{-1}, corresponding to a sheet resistance R_{BiSb}^{sheet} = 666 Ω for a 10-nm-thick stand-alone BiSb layer. Then, the current flowing into the BiSb layer was estimated by $I_{BiSb} = I_{bias} * \left(\frac{R_{stack}^{sheet}}{R_{BiSb}^{sheet}}\right)$. The uncertainty in this estimation originates from R_{BiSb}^{sheet}, as the actual sheet resistance of BiSb embedded in the multilayer stack may differ from that of the stand-alone BiSb. To reduce this uncertainty, we fabricated a reference stack with the same layer structure but excluding the BiSb layer and used the sheet resistance of this reference to indirectly evaluate the embedded BiSb sheet resistance.

The result shows that the effective conductivity of the BiSb layer in the actual stack is σ_{BiSb} = 1.3×10^5 $\Omega^{-1}m^{-1}$, corresponding to a sheet resistance of R_{BiSb}^{sheet} = 777 Ω, which is slightly different from the value for stand-alone BiSb. We have estimated the effective spin Hall angle θ_{SH}^{eff} based on this corrected value, as shown in Fig. 3. 12.

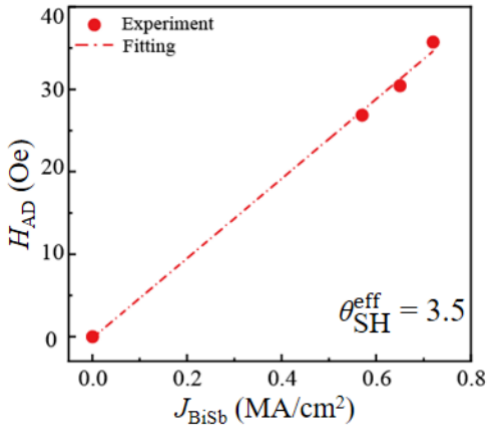

Figure 3.12. The extracted antidamping-like field H_{AD} as a function of J_{BiSb}.

3.3.2. Direct and Inverse Spin Hall Measurements: Signal Analysis and Spin Hall Angle Estimation

We now evaluate the performance of the DSH sensing device shown in Figure 3.8. Figure 3.13 shows a representative DSH resistance, defined as R_{DSH} = V_{DSH} / I_{DC}, measured at room temperature under a DC current of I_{DC} = 0.6 mA while sweeping an in-plane magnetic field H_y. A large resistance of R_{DSH} = 0.27 Ω was obtained, which is three orders of magnitude greater than the expected anomalous Hall resistance (~0.14 mΩ) for an in-plane H_y. This further confirms that the observed signal does not originate from conventional Hall effects.

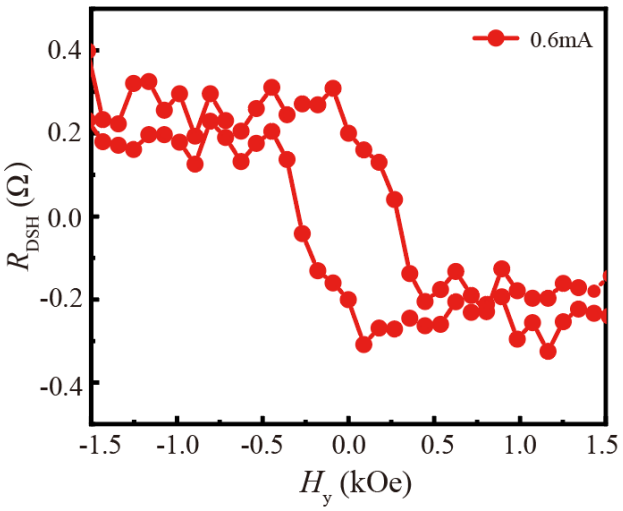

Figure 3.13. DSH resistance $R_{DSH} = V_{DSH}/ I_{DC}$ measured with I_{DC} = 0.6 mA at room temperature.

Figure 3.14 demonstrates the linear dependence of the output voltage V_{DSH}, confirming that the observed signal does not originate from thermomagnetic effects such as the anomalous Nernst effect.

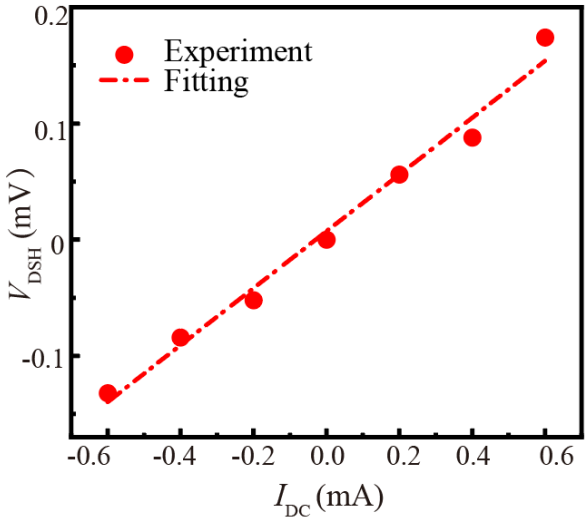

Figure 3.14. The relationship between the V_{DSH} and the bias current I_{DC}.

To further verify the spin-related origin of the signal, we examined the reciprocity between DSH and ISH measurements. Figures 3.15 (a) and 3.15 (b) compare the DSH resistance R_{DSH} and ISH resistance $R_{ISH} = V_{ISH} / I_{DC}$, obtained by injecting current perpendicularly through the pillar from the top electrode and detecting the voltage in the BiSb layer. For both cases, I_{DC} = 0.2 mA was applied, and both measurements yielded comparable resistances of R_{DSH}~R_{ISH}~0.27 Ω, confirming the reciprocal relation between DSH and ISH responses.

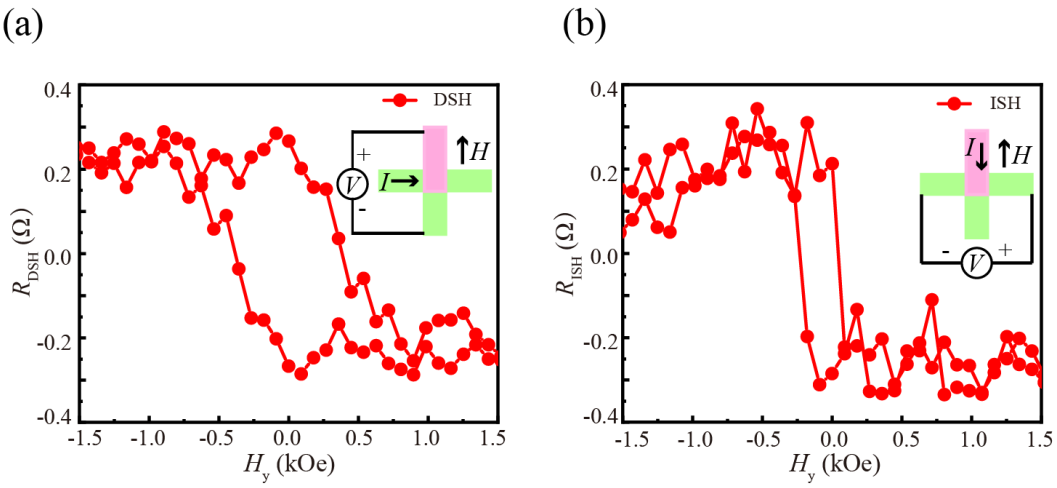

Figure. 3.15. (a) and (b) Comparison between R_{DSH} and ISH resistance R_{ISH} at I_{DC} = 0.2 mA.

The observed resistance is also consistent with previous ISH measurements performed on 20 μm-wide CoFe (5 nm)/MgO (2 nm)/BiSb (10 nm) stacks, where R_{ISH} ranged from 0.1~1 Ω. However, our present devices exhibit significantly higher noise levels, which we attribute to dominant spin-transfer noise, as will be discussed in Section 3.3.6. Nevertheless, the output resistance in our BiSb-based devices significantly surpasses that reported in Ta/MgO/CoFeB and Pt/MgO/CoFe devices[20], underscoring the potential advantage of BiSb in SOT-based magnetic sensors. The switching-field difference between the DSH and ISH configurations is discussed in detail in Section 3.3.10.

To estimate the intrinsic spin Hall angle θ_{SH} from the output resistance R_{DSH} of the device, we follow the model in Ref. 21, where the DSH resistance is expressed as:

$$R_{DSH} = \frac{V_{DSH}}{I_{BiSb}} = \frac{\theta_{SH} P R_{BiSb}^{sheet}}{w} \lambda_{sf} \tanh\left(\frac{t_s}{2\lambda_{sf}}\right) \tag{3.2}$$

where: t_s is the thickness of the surface conduction layer, λ_{sf} is the spin diffusion length of BiSb, P is the spin polarization of the FM layer, w is the width of the pillar.

Here, we consider that the two-dimensional topological surface states dominate conduction in 10 nm-thick BiSb[15, 22], and only the top surface contributes to the DSH signal. The current flowing through the BiSb layer beneath the pillar, I_{BiSb}, is calculated by the following equation:

$$I_{BiSb} = \left(\frac{R_{stack}^{sheet}}{R_{BiSb}^{sheet}}\right)\left(\frac{w}{w_H}\right) I_{DC} \tag{3.3}$$

The two preceding factors in Eq. (3.3) respectively account for (i) current shunting through the other layers, represented by the ratio $\frac{R_{stack}^{sheet}}{R_{BiSb}^{sheet}}$, and (ii) geometrical current reduction due to the narrower

pillar width ($\frac{w}{w_H}$). Here, R_{stack}^{sheet} denotes the sheet resistance of the full stack, and w_H is the width of the Hall bar. Substituting this expression into Eq. (3.1) yields the actual measurable DSH resistance:

$$R_{DSH} = \frac{V_{DSH}}{I_{DC}} = \left(\frac{R_{stack}^{sheet}}{R_{BiSb}^{sheet}}\right)\left(\frac{w}{w_H}\right)\frac{\theta_{SH}PR_{BiSb}^{sheet}}{w}\lambda_{sf}\tanh\left(\frac{t_s}{2\lambda_{sf}}\right)$$
$$= \frac{\theta_{SH}PR_{stack}^{sheet}}{w_H}\lambda_{sf}\tanh\left(\frac{t_s}{2\lambda_{sf}}\right) \quad (3.4)$$

We note that Eq. (3.3) is identical in form to the expression derived for ISH resistance in Ref. [8], where voltage shunting in the BiSb layer is considered, confirming theoretical reciprocity between DSH and ISH. Using: R_{stack}^{sheet} = 178.6 Ω, w_H = 50 μm, P = 0.5, t_s = 2 nm, λ_{sf} = 2 nm, we obtain: $\theta_{SH} \approx 164$, which is nearly 50 times larger than the effective spin Hall angle θ_{SH}^{eff}~3.5 estimated from second harmonic Hall measurements in Section 3.3.1. This significant discrepancy underscores the importance of using direct measurement techniques like DSH/ISH to access the intrinsic spin-charge conversion efficiency of topological insulators.

3.3.3. Cross-Validation of Spin Hall Angle: Comparison between Second Harmonic and DSH Methods

In this section, we compare the SHA values obtained from two commonly used techniques: the second harmonic Hall method and the DSH sensor method. Although both are widely applied to evaluate spin–charge conversion in BiSb/CoFe heterostructures, the SHA extracted from second harmonic measurements is significantly smaller than that obtained using the DSH approach.

This discrepancy arises mainly from the ultrathin CoFe layer (0.8 nm) used in this study. Because the spin diffusion length of CoFe (~6.2 nm) greatly exceeds its thickness, the injected spin current cannot be fully absorbed, leading to reduced interfacial spin accumulation and an underestimation of the effective spin–orbit torque in second harmonic measurements. Consequently, the resulting SHA appears smaller than its intrinsic value.

In contrast, the DSH method directly detects the spin current through the generated transverse voltage and is less susceptible to incomplete spin absorption in the FM layer. The SHA obtained from DSH measurements therefore more accurately reflects the total spin current injected from the BiSb layer.

These results highlight that the extracted SHA strongly depends on the FM layer thickness relative to its spin diffusion length. In ultrathin FM systems, second harmonic methods tend to underestimate the actual spin Hall angle, whereas DSH provides a more faithful measure of the intrinsic spin–charge

conversion efficiency. To our knowledge, a systematic comparison of these two techniques within the same BiSb-based heterostructure has not been previously reported, and the present work offers new insight into the influence of spin absorption on SOT characterization. We will address this problem later in chapter 4.

3.3.4. Influence of Bulk Conductivity in Topological Insulators on Signal Detection

In this section, we discuss how the bulk conductivity of the TI layer affects the detection of ISH signals in BiSb-based spintronic devices. The ISH voltage in our analysis is described by the following equation:

$$\frac{V_{\mathrm{ISH}}}{I} = \frac{\theta_{\mathrm{SH}} P R_{\mathrm{sheet}}}{w} \lambda_{\mathrm{sf}} \tanh\left(\frac{t_{\mathrm{s}}}{2\lambda_{\mathrm{sf}}}\right) \tag{3.5}$$

This model assumes that the charge current flows predominantly through the topological surface states of the BiSb layer, which are responsible for converting spin current into charge current. However, in practical TI materials, bulk conduction may be non-negligible due to the presence of defects or unintentional doping. These bulk pathways do not contribute directly to the spin-to-charge conversion but instead act as shunting channels that reduce the effective voltage output.

To better understand this effect, we consider an equivalent circuit model of the TI layer, as shown in Figure 3.16. The total output signal is generated by the spin-to-charge conversion at the top surface state, while the bulk and bottom surface states act as parallel current paths with lower resistance. These shunting paths divert part of the current away from the top surface and thereby reduce the detected ISH voltage.

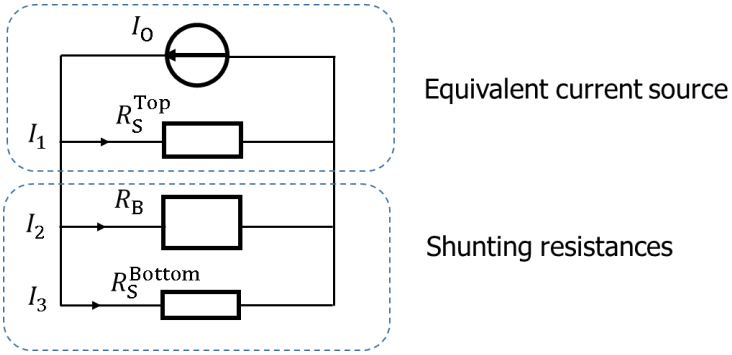

Figure 3.16. Equivalent circuit model for the topological insulator layer in the ISH sensing device. Only the top surface contributes to the ISH voltage, while the bulk and bottom surface act as shunting resistances.

In this model, the total output voltage V_O can be expressed as: $V_O = I_1 R_S^{Top} = I_2 R_B = I_3 R_S^{Bottom}$ with $I_O = I_1 + I_2 + I_3$. Here, I_O is the total injected current, and R_S^{Top}, R_B, and R_S^{Bottom} represent the resistances of the top surface, bulk, and bottom surface states, respectively. The total effective resistance of the TI layer is given by the parallel combination:

$$\frac{1}{R_{TI}} = \frac{1}{R_S^{Top}} + \frac{1}{R_B} + \frac{1}{R_S^{Bottom}} \tag{3.6}$$

From this relation, we can understand that the sheet resistance R_{sheet} used in Eq. (3.6) reflects not only the voltage-generating effect of the top surface but also the shunting effects from the bulk and bottom surface states. A more conductive bulk leads to a lower total sheet resistance, which in turn lowers the output ISH voltage, even though the spin Hall effect itself remains unchanged at the surface.

Therefore, to maintain high sensitivity and a high SNR in ISH-based sensing devices, it is essential to minimize bulk conductivity and enhance the dominance of surface-state transport. These insights also highlight the importance of material quality, especially in topological insulators with short spin diffusion lengths, such as BiSb.

3.3.5. Analysis of Parameter Uncertainty and Its Impact on Signal Estimation

In this study, the θ_{SH} was estimated from the experimentally measured spin Hall resistance R_{DSH}, based on the following expression (also denoted as Eq. (3.7) in the main text):

$$R_{DSH} = \frac{\theta_{SH} P R_{BiSb}^{sheet}}{w} \lambda_{sf} \tanh\left(\frac{t_s}{2\lambda_{sf}}\right) \tag{3.7}$$

where P denotes the spin polarization of CoFe, R_{BiSb}^{sheet} is the sheet resistance of the BiSb layer, w is the width of the pillar, λ_{sf} is the spin diffusion length, and t_s is the thickness of the topological surface states in BiSb.

To account for current shunting through the full multilayer stack, the expression was modified as follows:

$$R_{DSH} = \frac{\theta_{SH} P R_{stack}^{sheet}}{w_H} \lambda_{sf} \tanh\left(\frac{t_s}{2\lambda_{sf}}\right) \tag{3.8}$$

where R_{stack}^{sheet} and w_H are the sheet resistance and width of the full Hall track, respectively. Both of these values can be precisely measured through electrical and lithographic methods, contributing negligible uncertainty to the estimation of θ_{SH}.

However, the remaining key parameters - namely the spin polarization P, spin diffusion length λ_{sf}, and surface state thickness t_s - introduce significant uncertainty into the estimation of θ_{SH}. In the following sections, we analyze the impact of each parameter in detail.

(1) Spin Polarization P

We used a spin polarization value of $P = 0.5$ for $Co_{30}Fe_{70}$ in our analysis. This choice is supported by previous experimental data from Andreev reflection and TMR measurements[23,24]. As shown in Fig. 3.17, our sample's composition (Fe = 70%) matches well with those prior studies, where spin polarization values close to 0.5 were consistently reported.

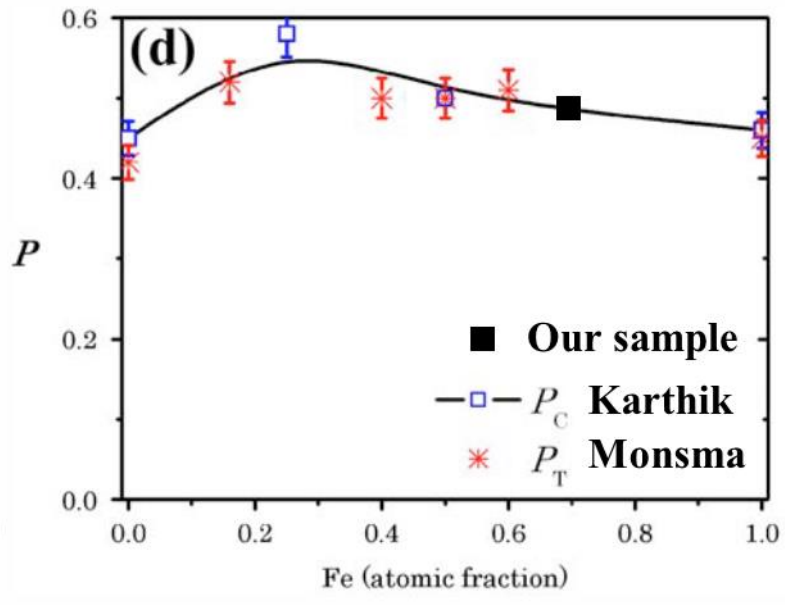

Figure 3.17. Spin polarization *P* of CoFe alloys as a function of Fe atomic fraction. Reproduced from Ref. 23 with permission from AIP and 24 with permission from AIP.

Temperature-dependent TMR measurements by Karthik et al. demonstrate that the spin polarization decreases from $P \approx 0.50$ at 8 K to $P \approx 0.45$ at room temperature, reflecting the expected thermal

suppression of interfacial spin asymmetry[23]. Based on this observation, we estimate an uncertainty of approximately ±10% in the spin polarization at room temperature. Since θ_{SH} is inversely proportional to P, this variation would result in a corresponding uncertainty in θ_{SH}. Importantly, by using the maximum reasonable value of $P = 0.5$, our estimation of θ_{SH} serves as a lower bound within the range $P = 0.45$~0.5.

(2) Spin Diffusion Length λ_{sf} and Surface State Thickness t_s

The spin diffusion length λ_{sf} and the surface state thickness ts of BiSb both appear in the nonlinear term $\lambda_{sf}\tanh\left(\frac{t_s}{2\lambda_{sf}}\right)$, which complicates the estimation. In this work, we assume a maximum possible value t_s = 2 nm based on the study of Bi thin films by Hou et al.[25]. Since BiSb has a larger band gap than elemental Bi, its topological surface states are expected to be equal to or thinner than 2 nm. Assuming a smaller t_s would increase the extracted θ_{SH} for the same experimental R_{DSH}, and thus t_s = 2 nm provides a conservative upper bound.

The estimation of λ_{sf} is more involved due to its appearance in the same nonlinear term. BiSb is a topological insulator with an enlarged quantum-size-induced band gap of approximately 200 meV at a thickness of 10 nm[20], which prevents spin diffusion into the bulk. Therefore, we impose the physical constraint $\lambda_{sf} \leq t_s$. We numerically calculated the term $\lambda_{sf}\tanh\left(\frac{t_s}{2\lambda_{sf}}\right)$ for several combinations of t_s and λ_{sf} within this boundary, as shown in Fig. 3.18. The results show that $\lambda_{sf}\tanh\left(\frac{t_s}{2\lambda_{sf}}\right)$ decreases as t_s and λ_{sf} decrease, meaning that its maximum value is obtained when both parameters take their largest physically allowed values.

Consequently, by adopting $t_s = 2$ nm and $\lambda_{sf} = 2$ nm, the extracted θ_{SH} in this work should be regarded as a conservative lower bound, valid for all physically reasonable combinations of $t_s \leq 2$ nm and $\lambda_{sf} \leq t_s$.

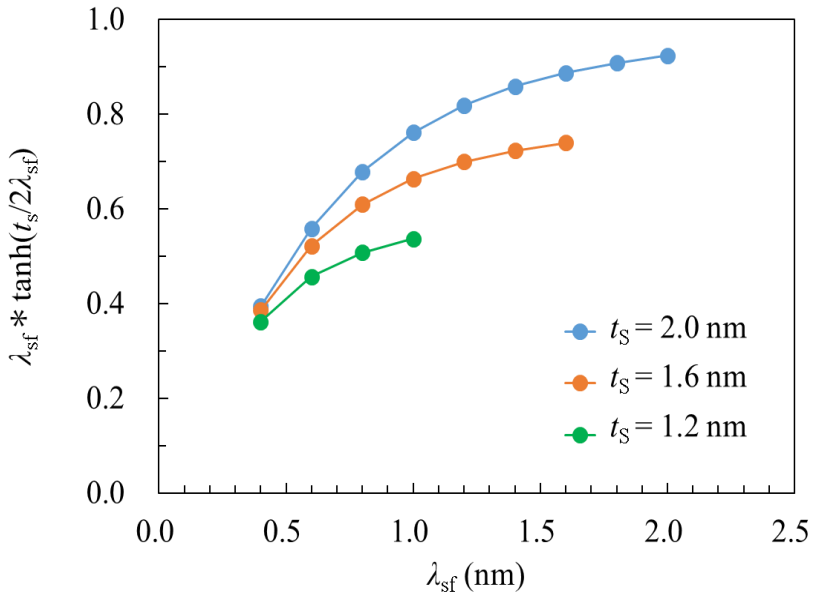

Fig. 3.18. Calculated value of $\lambda_{sf}\tanh\left(\frac{t_s}{2\lambda_{sf}}\right)$ with various $t_s \leq 2$ nm and $\lambda_{sf} \leq t_s$.

The calculated curves show that the term $\lambda_{sf}\tanh\left(\frac{t_s}{2\lambda_{sf}}\right)$ increases monotonically with both t_s and λ_{sf}. Therefore, by adopting the maximum physically reasonable values t_s = 2nm and λ_{sf} = 2nm, the extracted θ_{SH} represents a conservative lower bound within the full parameter space allowed by $t_s \leq 2$nm and $\lambda_{sf} \leq t_s$.

In summary, the uncertainties in the parameters P, λ_{sf}, and t_s directly influence the estimation of the spin Hall angle. By conservatively assuming their maximum values, we ensure that the calculated θ_{SH} serves as a lower bound of the true value. This approach allows us to make meaningful comparisons with previously reported values in the literature, even in the absence of precise knowledge for each parameter.

3.3.6. Noise Analysis in Spin Hall Magnetic Field Sensor

Noise fundamentally limits the detectivity of spin Hall magnetic field sensors. In this section, we briefly analyze the primary noise sources relevant to the devices studied in this work and clarify their implications for device performance.

(1) Johnson–Nyquist Thermal Noise

All resistive sensors are subject to Johnson–Nyquist noise, which originates from the thermal motion of charge carriers and sets an intrinsic lower bound for voltage fluctuations. The root-mean-

square voltage fluctuation is given by: $V_n = \sqrt{4k_B T R_{pillar} \Delta f}$, where k_B is the Boltzmann constant, T is the absolute temperature, R_{pillar} denotes the resistance of the effective sensor pillar that contributes to the detected voltage signal, and Δf is the measurement bandwidth. For our DSH sensing device, $R_{pillar} \approx 1$ kΩ. At room temperature (T = 300 K) and Δf = 1 Hz, the resulting Johnson–Nyquist thermal noise voltage is $V_n \approx 4.1\times10^{-9}$ V, which is much lower than the experimentally observed fluctuation, indicating that other noise sources dominate.

(2) Spin-Transfer Torque Noise

A key difference between DSH and ISH sensors is that the DSH configuration drives a spin current directly into the FM CoFe layer: $J_s = \frac{\hbar}{2e}\theta_{SH} J_{BiSb}$, where θ_{SH} is the spin Hall angle and J_{BiSb} is the in-plane charge current density in the BiSb layer. In our devices, the combination of a very large $\theta_{SH} \sim 164$ and an ultra-thin CoFe layer (0.8 nm) produces a pure spin current that exceeds the charge current by more than two orders of magnitude. The FM layer absorbs this spin current, and at high bias current and high spin Hall angle, the resulting SOT drives magnetization instabilities, manifesting as pronounced spin-transfer noise with a $1/f$ spectral characteristic. This mechanism is absent in ISH sensors because their spin Hall layer is nonmagnetic.

(3) Magnetic noise and amplifier noise.

These two noises are not different between the DSH and ISH sensors.

These analyses indicate that Johnson–Nyquist thermal noise is not the limiting factor in our devices. Instead, the dominant contributions arise from spin-transfer torque noise—enhanced by the ultra-thin CoFe layer (0.8 nm) and large spin Hall angle.

In addition to these intrinsic noise sources, the magnetization reversal mechanism also plays a critical role. The observed square-like switching behavior, rather than smooth magnetization rotation, results in domain-wall nucleation and depinning events, producing Barkhausen noise that further increases the low-frequency noise level. These abrupt domain-wall jumps lead to discontinuous changes in magnetization, which are directly translated into Hall-voltage fluctuations, thereby amplifying the 1/f-type noise component. Although both DSH and ISH devices in our experiments exhibit relatively high noise levels (Fig. 3.16), the DSH configuration inherently introduces spin-transfer noise because of the direct torque on the FM layer, whereas ISH sensors avoid this mechanism and thus have the potential for higher intrinsic SNR. These observations reinforce the discussion in Chapter 1 (Section 1.4.1), where

smooth magnetization rotation is emphasized as a key requirement for achieving low-noise performance in HDD read-head sensors.

3.3.7. Role of Magnetization Reversal Mode in Determining Linearity and Noise Performance

As discuessed in Chapter 1 (Section 1.4.1), smooth magnetization rotation is a key requirement for achieving stable, low-noise magnetic field sensing in high-density HDD read-head applications. In our DSH sensors, however, the CoFe layer reverses predominantly via discontinuous domain-wall–mediated switching, which contributes significantly to the enhanced low-frequency noise identified in Section 3.3.6 due to the associated Barkhausen-type magnetization jumps. Because the reversal mechanism directly determines both the linearity and the noise floor of spin-Hall-based sensors, this section examines how different switching modes influence device performance and discusses engineering strategies to promote smooth or quasi-coherent rotation in DSH devices.

The CoFe layer in our devices exhibits a square-like switching profile, indicative of domain-wall–mediated reversal rather than coherent rotation. This reversal mode leads to significant drawbacks: (1) large hysteresis due to irreversible domain-wall jumps, (2) nonlinear response near zero field arising from abrupt nucleation events, and (3) enhanced low-frequency Barkhausen noise, consistent with the observations in Section 3.3.6. These characteristics are incompatible with the requirements of HDD read heads, where linearity, reversibility, and low coercivity are essential for achieving high SNR during high-speed readout.

In contrast, smooth or quasi-coherent magnetization rotation enables a continuous and reversible response to small fields. This behavior reduces hysteresis, expands the linear sensing range, and suppresses Barkhausen fluctuations, thereby improving both signal fidelity and noise performance.

To realize smooth rotation, several engineering approaches can be adopted: reducing magnetic anisotropy via material tuning or CoFe thinning, replacing CoFe with a softer alloy (e.g., NiFe), optimizing the device geometry to promote single-domain–like behavior, applying a stabilizing bias field, and minimizing interfacial roughness to reduce pinning sites. These strategies directly target the reversal mechanism and form a practical pathway toward high-SNR DSH sensors compatible with HDD requirements. The following sections build upon this discussion by comparing DSH, ISH, and TMR devices under these performance criteria.

3.3.8. Comparison with TMR Sensors and Parameter Optimization for Noise Reduction

This section presents a detailed comparison between TMR sensors and DSH sensors, focusing on the trade-off between signal output and noise. We also discuss the geometric and material parameters that can be optimized to improve the SNR of DSH sensors.

(1) Comparison with TMR and ISH Sensors

TMR sensors are known for their high output due to large magnetoresistance ratios. However, in sensing applications, SNR, not absolute output, is the most critical factor. For instance, the Deep Space Network can detect signals as weak as -160 dBm (~1×10^{-19} W) from Voyager, thanks to its extremely low system noise. This highlights the importance of noise suppression over raw signal amplitude.

The output voltage of a TMR sensor is approximately proportional to the applied bias voltage: $\Delta V \sim V_{\text{bias}} * \text{TMR}$. However, scaling down the TMR device leads to increasing thermal and magnetic noise:

Thermal noise is given by:

$$N_{\text{th}} = \sqrt{4k_{\text{B}}TR_{\text{MTJ}}f} \tag{3.9}$$

where R_{MTJ} is the resistance of the magnetic tunnel junction.

Magnetic noise is described by:

$$N_{\text{mag}} = \Delta V \sqrt{\frac{4\mu_0 k_{\text{B}} T\alpha f}{\gamma H_{\text{stiff}}^2 M_{\text{s}} V_{\text{vol}}}} \tag{3.10}$$

where V_{vol} is the volume of the sensing layer, and H_{stiff} is the stiffness field.

Additionally, the reference/pinning layer stack in TMR devices imposes a lower bound on stack thickness and limits down-track resolution. Although dual-free-layer (DFL) structures (Fig. 3.19) have been introduced to eliminate the antiferromagnetic pinning layer, noise still increases as the device scales.

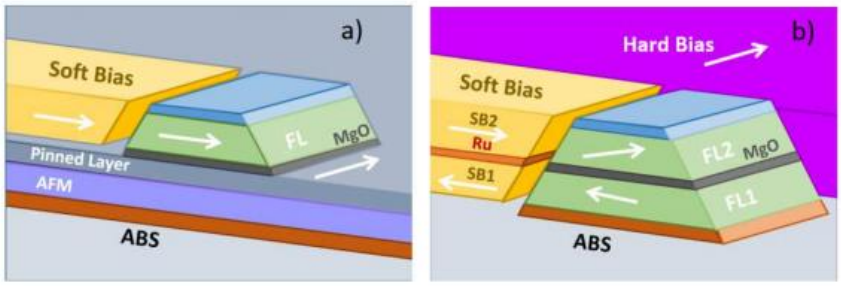

Fig. 3.19. (a) Conventional TMR sensor stack and (b) Dual free layer stack. Adapted from Ref. 26 with permission from IEEE.

As an alternative, ISH sensors use nonmagnetic spin Hall layers to avoid spin-transfer noise. The ISH output is given by:

$$V_{\mathrm{ISH}} = \frac{\theta_{\mathrm{SH}} P R_{\mathrm{sheet}}}{w} \lambda_{\mathrm{sf}} \tanh \frac{t_{\mathrm{s}}}{2\lambda_{\mathrm{sf}}} * I_{\mathrm{bias}} \tag{3.11}$$

In this case, the thermal noise depends only on the sheet resistance of the SOT layer:

$$N_{\mathrm{th}} = \sqrt{4 k_{\mathrm{B}} T R_{\mathrm{sheet}} f} \tag{3.12}$$

As R_{sheet} increases, output voltage scales linearly while noise increases sub-linearly: $V_{\mathrm{ISH}} \sim R_{\mathrm{sheet}}$, $N_{\mathrm{th}} \sim \sqrt{R_{\mathrm{sheet}}} \Rightarrow$ SNR improves. Experimental data from Ref. 8 (Fig. 3.20) shows that an ISH device using BiSb with $\theta_{\mathrm{SH}} \geq 16$ achieves SNR > 28 dB at only 50 μA of bias current.

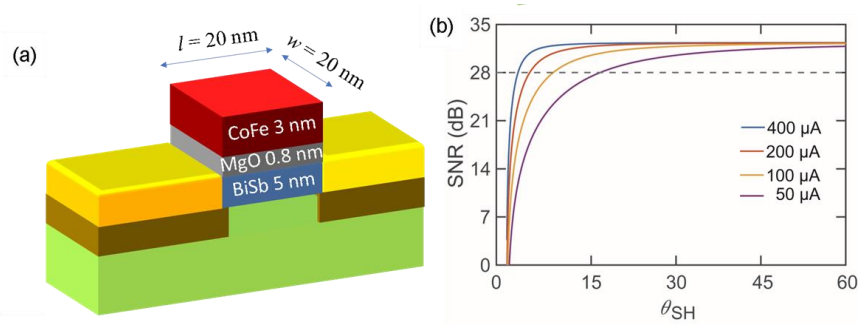

Fig. 3.20. (a) Model of a 20 nm × 20 nm inverse spin Hall sensor device with the stack of CoFe (3 nm)/MgO (0.8 nm)/BiSb (5 nm). Some insulating layers, magnetic bias layers and top magnetic shield are omitted for simplicity. (b) Relationships between the SNR and θ_{SH} for the device in (a) at different applied bias current I of 400, 200, 100, and 50 μA. Adapted from Ref. 8 with permission from AIP.

(2) Optimization of SNR in Direct Spin Hall Sensors

In contrast to the ISH structure, the DSH sensor developed in this study involves a FM layer directly interfaced with the spin Hall layer, resulting in STT effects. These effects introduce additional noise sources and lead to inherent trade-offs when optimizing the SNR.

To optimize SNR, both output enhancement and noise reduction must be considered simultaneously.

(1) Output Enhancement

The resistance change of the DSH sensor is expressed as:

$$R_{\mathrm{DSH}} = \frac{\theta_{\mathrm{SH}} P R_{\mathrm{BiSb}}^{\mathrm{sheet}}}{w} \lambda_{\mathrm{sf}} \tanh\left(\frac{t_{\mathrm{s}}}{2\lambda_{\mathrm{sf}}}\right) \tag{3.13}$$

where θ_{SH} is the spin Hall angle of the BiSb layer, P is the spin polarization of the FM layer, $R_{\mathrm{BiSb}}^{\mathrm{sheet}}$ is the sheet resistance of the BiSb layer, w is the pillar width, t_{st} is the spin Hall layer thickness, and λ_{sf} is the spin diffusion length.

Considering current shunting through other layers, the effective output resistance becomes:

$$R_{\mathrm{DSH}} = \frac{\theta_{\mathrm{SH}} P R_{\mathrm{stack}}^{\mathrm{sheet}}}{w_{\mathrm{H}}} \lambda_{\mathrm{sf}} \tanh\left(\frac{t_{\mathrm{s}}}{2\lambda_{\mathrm{sf}}}\right) \tag{3.14}$$

where $R_{\mathrm{stack}}^{\mathrm{sheet}}$ is the sheet resistance of the entire multilayer stack and w_{H} is the Hall track width.

The following strategies are identified to increase the output signal:

① Increase $R_{\mathrm{stack}}^{\mathrm{sheet}}$: This can be achieved using buffer, interlayer, or capping layers with higher resistivity, which increases the voltage drop within the spin Hall layer.

② Use high-spin-polarization ferromagnets: Half-metallic ferromagnets are promising candidates to enhance P.

③ Improve spin Hall angle θ_{SH}: This can be achieved by promoting BiSb (012) orientation and suppressing Sb diffusion into the FM layer through interface engineering.

④ Increase bias current I_{bias}: Within thermal and reliability limits, higher bias currents increase the output linearly.

(2) Noise Reduction

The SNR also depends on minimizing intrinsic and extrinsic noise contributions, including thermal noise, magnetic noise, and spin-transfer noise.

① Thermal Noise

The thermal noise is given by:

$$N_{\mathrm{th}} = \sqrt{4 k_{\mathrm{B}} T R_{\mathrm{pillar}} f} \tag{3.15}$$

where R_{pillar} is the pillar resistance and f is the measurement bandwidth. Reducing R_{pillar} decreases thermal noise, which would suggest using low-resistivity layers. However, this directly conflicts with output enhancement strategies, as increasing resistance (e.g., via high-resistivity interlayers) improves

the signal. In practice, the signal gain (~R) can outpace the thermal noise increase (~$\sqrt{R}$), resulting in a net SNR benefit when moderate resistance increases are allowed.

② Magnetic Noise

The magnetic noise can be expressed as:

$$N_{\mathrm{mag}} = \Delta V \sqrt{\frac{4\mu_0 k_{\mathrm{B}} T \alpha f}{\gamma H_{\mathrm{stiff}}^2 M_{\mathrm{s}} V_{\mathrm{vol}}}} \tag{3.16}$$

where α is the Gilbert damping constant, H_{stiff} is the stiffness field, M_{s} is the saturation magnetization, and V_{vol} is the FM sensing volume. This indicates that extremely thin FM layers increase magnetic noise due to reduced volume. Therefore, while ultrathin FM layers are often used to maximize spin-orbit torque efficiency, they must not be reduced excessively, as this compromises magnetic stability and increases low-frequency fluctuations.

③ Spin-Transfer Noise

The DSH architecture is particularly susceptible to spin-transfer noise because the spin Hall layer (BiSb) has an exceptionally large spin Hall angle (θ_{SH} ~ 164). The spin current density injected into the FM layer is:

$$J_{\mathrm{s}} = \frac{\hbar}{2e} \theta_{\mathrm{SH}} J_{\mathrm{BiSb}} \tag{3.17}$$

which exceeds the charge current by over two orders of magnitude. As a result, even a modest bias current of I_{bias} = 0.6 mA (corresponding to a current density of 2.7 × 10^4 A/cm^2) produces strong spin torque on the FM layer. This is particularly problematic for ultra-thin FM layers (e.g., 0.8 nm CoFe), where magnetization becomes dynamically unstable, leading to chaotic behavior and enhanced 1/f noise.

This phenomenon was confirmed experimentally (Fig. 3.21), where devices with high θ_{SH} BiSb and thin CoFe layers exhibited substantial low-frequency noise fluctuations.

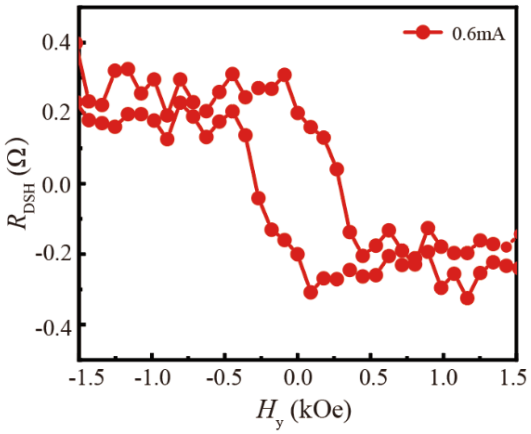

Fig. 3.21. DSH resistance $R_{DSH} = V_{DSH} / I_{DC}$ measured with I_{DC} = 0.6 mA at room temperature.

To mitigate this, we fabricated devices with thicker CoFe (2 nm) and reduced spin Hall angle (θ_{SH} < 1), resulting in a significant reduction in spin-transfer noise (Fig. 3.22 (a) and (b)).

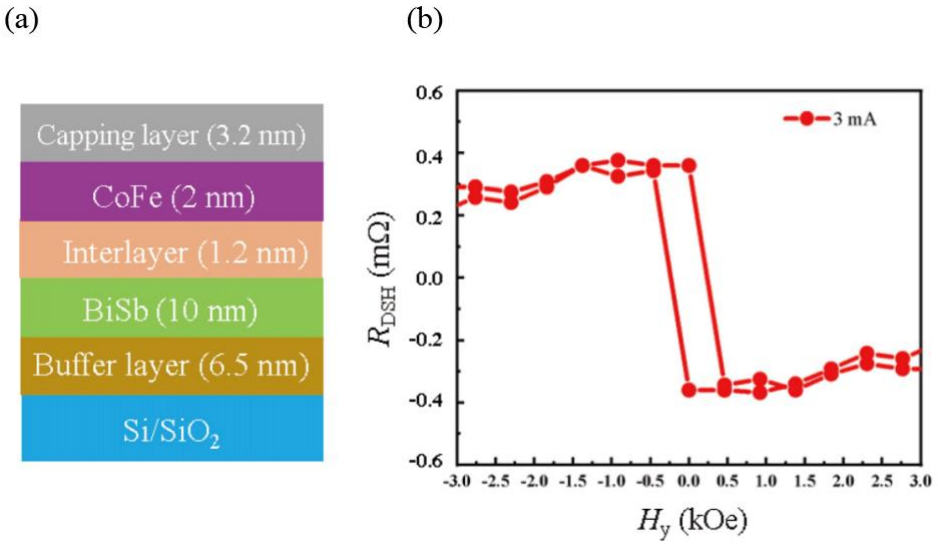

Fig. 3.22. (a) Stacking structure and (b) R_{DSH} curve of a device using a thicker CoFe (2 nm) and BiSb with lower θ_{SH} (<1) to reduce the spin-transfer noise.

④ Trade-offs and Design Considerations

The optimization of SNR in DSH sensors is nontrivial because strategies for output enhancement often exacerbate noise sources:

1) Increasing R_{sheet} and I_{bias} improves signal but raises thermal and spin-transfer noise;

2) Thinning the FM layer reduces thermal noise but increases magnetic noise;

3) Enhancing θ_{SH} amplifies spin torque noise, limiting the maximum bias current.

Ultimately, a balanced approach is required, involving moderate θ_{SH}, thicker FM layers for magnetic stability, and interface engineering to maintain acceptable output without triggering dynamic instabilities.

In summary, while DSH sensors offer a structurally simple and scalable architecture, their SNR optimization involves inherent trade-offs between output enhancement and noise suppression. The results in Fig. 3.21 demonstrate that reducing θ_{SH} and increasing CoFe thickness effectively suppress spin-transfer noise, highlighting the importance of material selection and device geometry in achieving high SNR.

3.3.9. Comparative Scaling Analysis of TMR, DSH, and ISH Sensing Devices

To evaluate the scaling potential of different magnetic field sensing devices for future high-density magnetic recording, we compare the performance of TMR, DSH, and ISH sensors. A key assumption in this comparison is that the bias voltage is fixed for all devices, which is the typical operating condition for magnetic read heads. Under this assumption, the scaling behavior in both the track-width direction (X scaling) and the read-gap direction (Z scaling) is analyzed.

(1) Scaling Model

Figure 3.23 shows a schematic of the ISH sensor viewed from the air bearing surface (ABS). For DSH sensors, the positions of the current source and the voltmeter are exchanged. The scaling analysis focuses on the rectangular area highlighted by dashed lines, where the length (X direction) corresponds to the track width of the HDD medium and the height (Z direction) corresponds to the bit length. We refer to these as “X scaling” and “Z scaling” respectively.

Because X scaling shrinks the sensor only in the transverse direction (perpendicular to the current flow), the voltage drop along the current path remains unchanged, and therefore the intrinsic signal level of TMR and DSH devices does not change under X-direction scaling.

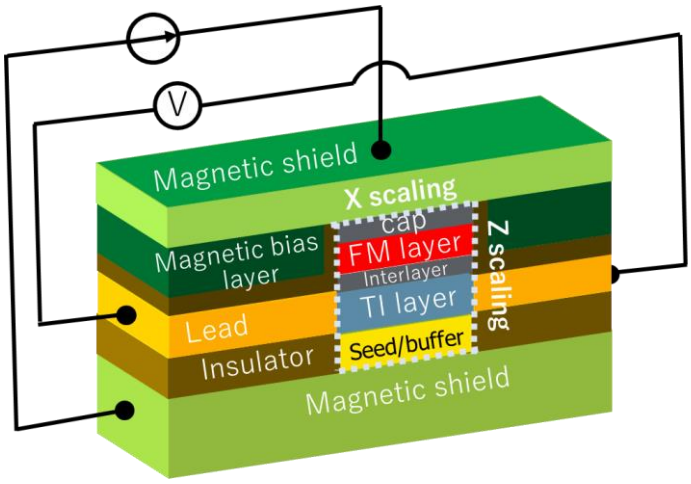

Fig. 3.23. Schematic drawing of an ISH sensing device as seen from the air bearing surface. The Table below summarizes how the signal voltage and the noise changes with scaling in TMR, ISH, and DSH sensing devices. We also compare the margin of increasing the bias voltage devices.

Table 3.1 summarizes how the signal, noise, and available bias voltage margin change with scaling for each sensor type.

Device	Properties	X scaling	Z scaling
TMR	Signal	→	N/A
	Noise	↑	N/A
	V_{bias} margin	Small	N/A
ISH	Signal	↓	↑
	Noise	→	↑
	V_{bias} margin	Large	Large
DSH	Signal	→	→
	Noise	↑	↓
	V_{bias} margin	Medium	Medium

(2) Device-Specific Scaling Behavior

① TMR Sensors

For X scaling, at a constant bias voltage the signal output remains unchanged, but the resistance of the MTJ increases, resulting in higher thermal noise. The bias current density in TMR sensors is already high, and further increasing the bias voltage is limited by spin-transfer torque noise. Consequently, the available bias margin is small, and the SNR decreases with X scaling. Z scaling of TMR sensors is already approaching fundamental limits due to the thickness of the multilayer stack, and therefore is not considered in this analysis.

② ISH Sensors

For X scaling, a constant bias voltage leads to a reduced bias current due to the increased pillar resistance, resulting in a lower output signal. The noise, however, remains determined by the sheet resistance of the TI layer and is not significantly affected by the pillar resistance. Consequently, the SNR decreases with X scaling.

However, ISH sensors do not suffer from spin-transfer torque noise because the spin Hall layer is nonmagnetic, providing ample margin to increase the bias voltage/current to recover signal and SNR. For example, as shown in Ref. 8, an ISH sensor with a spin Hall angle of 2 requires a bias current density of 1×10^8 A/cm^2 for SNR = 28 dB in a 20×20 nm^2 pillar, which can be reduced to 2.5×10^7 A/cm^2 when the spin Hall angle is increased to 5. Experimentally, we achieved $\theta_{SH} \sim 61$, resulting in an even lower required current density of 3.4×10^6 A/cm^2. This wide bias margin justifies our assumption of constant bias current in previous ISH analyses.

For Z scaling, reducing the TI layer thickness decreases the pillar resistance, thereby increasing the bias current at constant bias voltage. Meanwhile, the sheet resistance increases, resulting in a higher output voltage because: $V_{ISH} \sim R_{sheet} I_{bias}$. Although thermal noise also increases with resistance, it scales as $\sqrt{R}$ and thus grows slower than the signal. As a result, the SNR actually improves with Z scaling, making ISH sensors more resistant to scaling effects compared to TMR devices.

③ DSH Sensors

For X scaling, the signal output is largely unchanged, but the increased pillar resistance leads to higher thermal noise, resulting in a net SNR reduction. Similar to ISH devices, the bias margin of DSH devices is moderate because their required bias current density is small, allowing some increase in bias voltage to offset noise. However, unlike ISH devices, DSH sensors suffer from spin-transfer torque noise in the ferromagnetic layer, similar to TMR sensors, which limits their maximum allowable bias.

For Z scaling, reducing the TI layer thickness lowers the bias current due to increasing R_{sheet}. However, since the output voltage $\propto R_{sheet} I_{bias}$, it should remain the same. Furthermore, the pillar resistance also decreases, thereby lowering the thermal noise. As a result, the SNR actually increases.

In summary, in terms of resistance to scaling-induced SNR degradation:

ISH sensor > DSH sensor > TMR sensor

Furthermore, due to spin-transfer noise limitations, DSH sensors are unlikely to be suitable for next-generation magnetic read heads beyond areal densities of 4 Tb/in^2, whereas ISH sensors, with their superior bias margin and scalability, remain a promising alternative.

3.3.10. Switching Field Discrepancy and Comparative Evaluation between DSH and ISH Sensors

A key distinction between the DSH and ISH sensors investigated in this work lies in their noise performance and magnetic switching behavior. In the DSH sensor configuration, the bias current flows along the Hall track and injects a transverse spin current directly into the FM CoFe layer. As detailed previously in Section 3.3.8, the combination of an ultra-thin CoFe layer (0.8 nm) and a very large spin Hall angle ($\theta_{SH} \sim 161$) generates an extremely large spin current density ($J_s = \frac{\hbar}{2e}\theta_{SH} J_{BiSb}$), which leads to strong spin-transfer torque and pronounced low-frequency noise. Even under a modest bias current of 0.6 mA (2.8×10^4 A/cm^2), the FM magnetization becomes unstable, resulting in significant 1/*f*-type fluctuations.

To suppress this STT-driven noise, an optimized DSH structure with a thicker CoFe layer (2 nm) and reduced θ_{SH} (< 1) was fabricated. As shown in Fig. 3.22, this device exhibits substantially lower noise even at higher bias current, although the output decreases to ~0.35 mΩ. These results emphasize the intrinsic trade-off of the DSH architecture: higher θ_{SH} and thinner FM layers enhance output but simultaneously amplify spin-transfer noise, whereas thicker FM layers and lower θ_{SH} improve noise stability at the cost of reduced sensitivity.

Another notable difference between DSH and ISH sensors is the coercive field observed in their resistance hysteresis loops. The ISH configuration exhibits a smaller coercive field due to stronger local Joule heating, as the perpendicular current directly heats the pillar region. In contrast, Joule heating in the DSH sensor occurs mainly along the Hall track, resulting in a higher effective coercive field in the resistance loop.

We also verified the reciprocal relationship between the DSH and ISH effects by comparing their voltage responses under identical bias current conditions (I_{DC} = 0.2 mA), as shown in Fig. 3.15. Both configurations yield similar magnitudes ($|R_{DSH}| \approx |R_{ISH}| \approx 0.27$ Ω for a 40-μm-wide pillar), confirming the expected reciprocity. This behavior is consistent with our previous ISH devices based on CoFe (5 nm)/MgO (2 nm)/BiSb (10 nm), which exhibited $|R_{ISH}| \sim 0.1$–1 Ω for 20-μm-wide pillars. Furthermore, the output of BiSb-based devices significantly exceeds that of conventional Ta/MgO/CoFeB or Pt/MgO/CoFeB SOT sensors, illustrating the advantage of using BiSb as the spin Hall material.

Although both DSH and ISH devices exhibit non-negligible noise due to measurement limitations, the ISH architecture inherently avoids spin-transfer torque and therefore possesses a fundamentally higher potential SNR under optimized conditions. In contrast, DSH sensors benefit from a simpler in-plane current geometry and scalable design.

Overall, these results clarify the switching-field discrepancy in Fig. 3.15 and highlight the contrasting physical origins of noise and switching behavior in DSH versus ISH structures. A quantitative noise analysis was presented in the previous sections to evaluate the implications for magnetic sensing performance.

3.4. Summary of Novelty and Key Contributions

This work presents a novel approach to magnetic field sensing for HDD read heads by utilizing the DSHE. The main differences and contributions compared to previously published studies are summarized below.

(1) Distinct Physics and Device Structures

Unlike previously reported works, the present study focuses on a DSHE-based magnetic field sensor specifically designed for HDD read head applications, rather than SOT-MRAM devices or ISHE-based sensors. Before, Huy et al. reported an ISHE-based magnetic field sensor[8] while Zhang et al. investigated DSHE phenomena but aimed at SOT-MRAM rather than sensing application.[27].

Here, this work applies DSHE physics to HDD reader sensors, which differs both in device geometry and operational objectives. Table 3.2 highlights the distinction between previous works and the present study.

Table 3.2. Comparison between previous studies and this work.

	DSHE	ISHE
H. H. Huy *et al.* Appl. Phys. Lett. 122 (2023) 052401		Magnetic field sensing device for HDD reader
R. Zhang *et al.* Appl. Phys. Lett. 124 (2024) 072402	SOT-MRAM	
This work	Magnetic field sensing device for HDD reader	

(2) Verification of Reciprocity between DSHE and ISHE

This work confirms the reciprocal relation between DSHE and ISHE within the same device structure. This was achieved by employing an interfacial layer engineered to be transparent to both: Pure spin currents (essential for DSHE measurements), and Spin-polarized charge currents (required for ISHE measurements). In contrast, the device structure in Huy et al., which included a 2 nm-thick MgO interlayer optimized for ISHE[8], blocked pure spin current diffusion and therefore could not verify this reciprocity experimentally.

(3) Cross-Validation of Spin Hall Angle Determination

The device platform developed in this study also allows multiple techniques to be employed on the same device for evaluating the spin Hall angle, including: DSHE-based electrical measurements, and Second harmonic Hall measurements. This enables direct comparison of spin Hall angle values obtained from independent methods, which is particularly valuable for device engineering. In the work of Huy et al., such cross-validation was not possible because the MgO barrier suppressed pure spin current transport, preventing DSHE or spin pumping measurements[8].

(4) Noise Mechanism Analysis in DSHE vs. ISHE Sensors

This work reveals that the noise origins in DSHE-based sensors differ fundamentally from those in ISHE-based sensors: In DSHE sensors, spin-transfer noise is a dominant contributor, especially when a high spin Hall angle material such as BiSb is used. In ISHE sensors, no net spin torque acts on the ferromagnetic layer, and such spin-transfer noise is absent. This insight is critical for practical design because it identifies an intrinsic trade-off in DSHE-based magnetic field sensing: high sensitivity (enabled by large spin Hall angle) versus increased spin-transfer noise.

In summary, this work provides: (1) A DSHE-based magnetic field sensor specifically tailored for HDD reader applications, differing in both physics and device design from previous studies, (2) The first experimental confirmation of the reciprocity between DSHE and ISHE in the same device, (3) a methodology enabling cross-validation of spin Hall angle measurements within a single device platform, and (4) a detailed analysis of noise origins, revealing the presence of spin-transfer noise in DSHE sensors and its absence in ISHE sensors. These findings not only demonstrate the novelty of the present approach but also provide important guidelines for the future development of spin Hall effect-based magnetic field sensors.

Collectively, these contributions establish DSHE-based sensing as a promising and scalable candidate for next-generation magnetic read heads, particularly when implemented using high-efficiency spin Hall materials such as BiSb.

3.5. Reference

1 S. Fukami, T. Anekawa, C. Zhang, and H. Ohno, Nat. Nanotechnol. 11, 621 (2016).

2 K. Garello, C. O. Avci, I. M. Miron et al., Appl. Phys. Lett. 105, 212402 (2014).

3 C. Zhang, S. Fukami, H. Sato, F. Matsukura, and H. Ohno, Appl. Phys. Lett 107, 012401 (2015).

4 C. O. Avci, A. Quindeau, C.-F. Pai, M. Mann, L. Caretta, A. S. Tang, M. C. Onbasli, C. A. Ross, and G. S. D. Beach, Nat. Mater. 16, 309 (2017).

5 S. Manipatruni, D. E. Nikonov, C.-C. Lin, T. A. Gosavi, H. Liu, B. Prasad, Y.-L. Huang, E. Bonturim, R. Ramesh, and I. A. Young, Nature 565, 35 (2019).

6 V. T. Pham, I. Groen, S. Manipatruni, W. Y. Choi, D. E. Nikonov, E. Sagasta, C. C. Lin, T. A. Gosavi, A. Marty, L. E. Hueso, I. A. Young, and F. Casanova, Nat. Electron. 3, 309 (2020).

7 Q. Le, B. R. York, X. Liu, S. T. Le, C. Hwang, M. Gribelyuk, X. Xu, K. S. Ho, H. Takano, J. Sakaki et al., US Patent No. 11875827 (2022).

8 H. H. Huy, J. Sasaki, N. H. D. Khang, S. Namba, P. N. Hai, Q. Le, B. York, C. Hwang, X. Liu, M. Gribelyuk et al., Appl. Phys. Lett. 122, 052401 (2023).

9 A. R. Mellnik, J. S. Lee, A. Richardella, J. L. Grab, P. J. Mintun, M. H. Fischer, A. Vaezi, A. Manchon, E.-A. Kim, N. Samarth et al., Nature 511, 449 (2014).

10 H. Wu, P. Zhang, P. Deng, Q. Lan, Q. Pan, S. A. Razavi, X. Che, L. Huang, B. Dai, K. Wong et al., Phys. Rev. Lett. 123, 207205 (2019).

11 X. Lin, W. Yang, K. L. Wang, and W. Zhao, Nat. Electron. 2, 274 (2019).

12 M. Lang, M. Montazeri, M. C. Onbasli, X. Kou, Y. Fan, P. Upadhyaya, K. Yao, F. Liu, Y. Jiang, W. Jiang et al., Nano Lett. 14, 3459 (2014).

13 C. Tang, C.-Z. Chang, G. Zhao, Y. Liu, Z. Jiang, C.-X. Liu, M. R. McCartney, D. J. Smith, T. Chen, J. S. Moodera et al., Sci. Adv. 3, e1700307 (2017).

14 T. Shirokura and P. N. Hai, Appl. Phys. Lett. 122, 232404 (2023).

15 T. Fan, M. Tobah, T. Shirokura, N. H. D. Khang, and P. N. Hai, Jpn. J. Appl. Phys., Part 1 59, 063001 (2020).

16 T. Fan, N. H. D. Khang, S. Nakano, and P. N. Hai, Sci. Rep. 12, 2998 (2022).

17 N. H. D. Khang, Y. Ueda, and P. N. Hai, Nat. Mater. 17, 808 (2018).

18 M. Hayashi, J. Kim, M. Yamanouchi, and H. Ohno, Phys. Rev. B 89, 144425 (2014).

19 Q. Le, C. Hwang, B. R. York, T. A. Nguyen, Z. Gao, K. S. Ho, and P. N. Hai, US Patent 11694713 (2023).

20 L. Liu, C. T. Chen, and J. Z. Sun, Nat. Phys. 10, 561 (2020).

21 C. O. Avci, K. Garello, A. Ghosh, M. Gabureac, and S. F. Alvarado, P. Gambardella Nat. Phys. 11, 570 (2015).

22 Y. Ueda, N. H. D. Khang, K. Yao, and P. N. Hai, Appl. Phys. Lett. 110, 062401 (2017).

23 S. V. Karthik *et al.* [J. Appl. Phys. 105, 07C916 (2009)..

24 D. J. Monsma and S. S. P. Parkin, Appl. Phys. Lett. 77, 720–722 (2000).

25 D. Hou, Z. Qiu, K. Ando, Y. Kajiwara, and E. Saitoh, Appl. Phys. Lett. 101, 042403 (2012).

26 X. Liu, D. Marui, G. Albuquerque, C. Shang, L. Wang, Z. Diao, Y. Zheng, C.-C. Hu, Y.-H. Wang, H. Liu, G. Li, A. Roy, C. J. Chien, M. Mao, J. Freitag, Y. Okada, Y. Li, 2022 IEEE 33rd Magnetic Recording Conference (TMRC) (2022),

27 X. Zhang, Y. Zhang, H. Liu, J. Wang, Y. Xu, T. Ma, Y. Zhang, G. Wang, B. Wu, W. Zhang, and K. L. Wang, Appl. Phys. Lett. 124, 072402 (2024).

Chapter 4 Comparison of Spin Hall angles measured by Spin Accumulation, Spin–Orbit Torque, and Spin Hall Magnetoresistance in BiSb/Interlayer/CoFe Heterostructures

In this chapter, we present a systematic comparison of θ_{SH} in BiSb/CoFe heterostructures determined by three methods: (1) SOT-based second harmonic Hall analysis, (2) SMR, and (3) direct spin accumulation measurement. To further elucidate how temperature influences spin current generation in BiSb and the sensitivity of each measurement method to different physical mechanisms (e.g., bulk conduction vs. surface states), the comparison was performed across a wide temperature range from room temperature down to cryogenic conditions. Our results reveal that θ_{SH} generally increases with decreasing temperature, but remains consistently higher when extracted from SA measurements than from either SOT or SMR analyses. We conclude this chapter with a discussion on the implications of these findings for interpreting the physical meaning of θ_{SH} as determined by different measurement techniques.

4.1. Introduction and Motivation

The realization of efficient spin - charge interconversion lies at the core of modern spintronics research, underpinning both fundamental studies and device-level applications[1,2]. Traditionally, HM/FM heterostructures have served as primary platforms for generating and detecting spin currents through the spin Hall effect, with typical θ_{SH} on the order of 0.1[3-5]. However, such small θ_{SH} values require high current densities ($> 5 \times 10^6$ A/cm^2) to achieve SOT switching of magnetic layers with PMA, thereby limiting their scalability and energy efficiency for practical devices, such as SOT-MRAM[6-8].

Recently, TI/FM heterostructures have emerged as promising alternatives, owing to their substantially larger θ_{SH} and efficient spin current conversion at room temperature[9-14]. Among various TI materials, BiSb has attracted particular interest due to its high conductivity, large θ_{SH}, and compatibility

with industrial sputtering processes[15,16]. Our previous studies have demonstrated fully sputtered BiSb heterostructures exhibiting θ_{SH} values significantly exceeding those of conventional heavy metals, indicating strong potential for next-generation SOT-based devices[17-20]. In addition, BiSb/FM heterostructures with in-plane magnetization have been applied to magnetic field sensing devices that utilize the ISHE and the DSHE, which are promising candidates for next-generation high-density magnetic recording readers (4 Tbit/in^2)[21-24].

Despite these advances, a key issue remains unresolved: the physical interpretation of the giant θ_{SH} observed in TI/FM heterostructures often depends on the measurement technique employed. Conventional θ_{SH} estimation techniques include second harmonic Hall ($R_H^{2\omega}$) analysis, which determines the effective SOT acting on the adjacent magnetic layer[25], spin-torque ferromagnetic resonance (ST-FMR)[26], and loop-shift methods[12]. These techniques differ in their underlying principles, measurement sensitivity, and applicability to various material systems. Details of the ST-FMR approach will be discussed later in this section, along with other complementary methods. Building on this, the evaluation of θ_{SH} across different material systems has been extensively explored using a wide range of techniques based on distinct physical principles. These include spin Hall effect tunneling spectroscopy (SHT), ST-FMR, spin valves, spin pumping, and the spin Seebeck effect, each offering unique advantages and limitations.

SHT provides a direct means to probe the spin-dependent density of states at FM/I/NM interfaces, although the method typically requires the fabrication of high-quality tunnel junctions. Nakagawara et al. employed SHT combined with weak-antilocalization (WAL) analysis to accurately determine the θ_{SH} of Pt. As shown in their device schematic (Fig. 4.1 in Ref. 27), the use of both ISHE and DSHE configurations allows suppression of spurious contributions from the AHE and AMR, ensuring that the extracted SHT signals originate purely from the spin Hall effect. By independently determining the spin relaxation length via WAL, they reported a robust θ_{SH} of approximately 4% at room temperature. This approach eliminates magnetic proximity effects and parallel conduction paths, although it still requires precise control of tunnel barrier quality and accurate evaluation of the spin relaxation length.

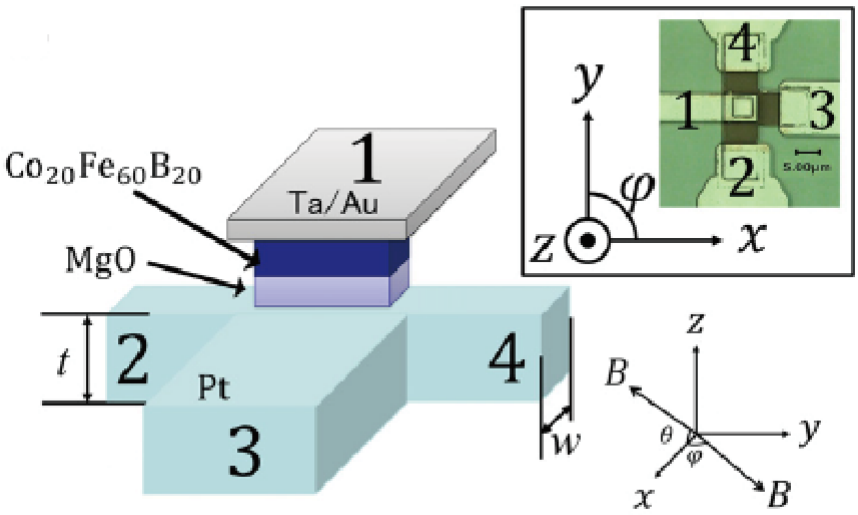

Figure 4.1. Schematic illustration of the SHT device structure. The FM/I/HM tunnel junction enables suppression of magnetic proximity and parallel conduction effects. Figure adapted from Ref. 27 with permission from AIP.

ST-FMR is a widely used and nominally self-calibrating method for determining the spin Hall angle in heavy-metal/ferromagnet bilayers. In this technique, a radio-frequency charge current drives magnetization precession in the ferromagnet via both the spin Hall torque and the accompanying RF Oersted field, and the resulting oscillatory anisotropic magnetoresistance generates a measurable DC mixing voltage. Wang et al. performed ST-FMR measurements on $Pt/Ni_{81}Fe_{19}$ bilayers with varying ferromagnet thicknesses and extracted an intrinsic spin Hall angle of $\theta_{SH} \approx 0.068$ for Pt at room temperature by explicitly accounting for spin diffusion in the Py layer. Their device configuration (Fig. 4.2 in Ref. 28) enables frequency-resolved measurements, and the authors further demonstrated that θ_{SH} remains nearly constant over a broad temperature range from 13 K to 300 K. While ST-FMR is compatible with standard microfabrication and provides in-situ calibration through the ratio of symmetric and antisymmetric voltage components, the method requires careful modeling of spin diffusion and can be influenced by interfacial spin scattering and spin pumping contributions.

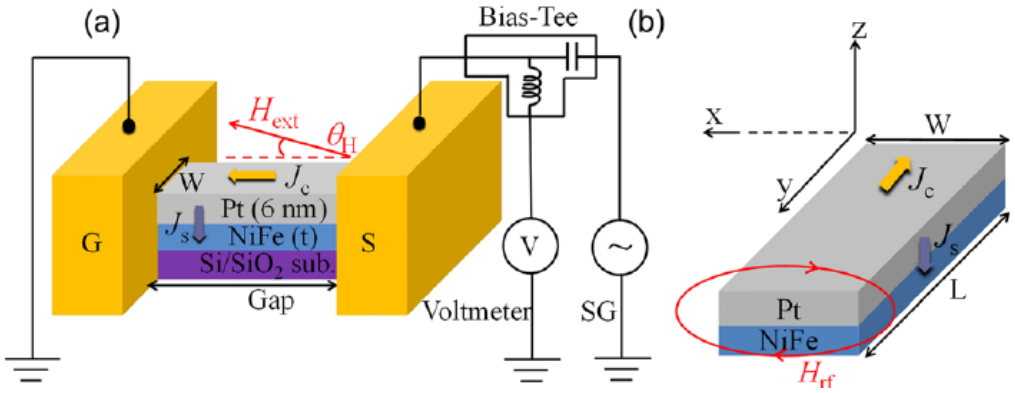

Figure 4.2. (a) The schematic diagram of the ST-FMR measurement configuration. (b) The Pt/Py microstrip with the charge current J_c, spin current J_s, RF Oersted field (H_{rf}). Figure adapted from Ref. 28 with permission from AIP.

Spin valves provide an established route for evaluating the spin Hall angle, particularly through the spin absorption method implemented in lateral nonlocal geometries. In this configuration, a pure spin current is generated by electrical spin injection from a ferromagnetic electrode into a Cu channel and is partially absorbed into a transition-metal wire, where the inverse spin Hall effect produces a measurable charge voltage. Isasa et al. employed Py/Cu lateral spin valve (LSV) incorporating Pt and Au absorption wires to extract both the spin diffusion length and the spin Hall angle over a wide temperature range.[29] As shown in their device schematics (Fig. 4.3 in Ref. 29), the reduction of the nonlocal spin-valve signal yields the spin diffusion length via the spin absorption analysis, while the ISHE configuration enables determination of the spin Hall conductivity after correcting for current shunting and the effective spin current. Their results revealed that Pt exhibits a predominantly intrinsic spin Hall mechanism, whereas Au is governed by extrinsic scattering, with a clear additional contribution from phonon-induced skew scattering due to its low residual resistivity. The spin-valve approach offers straightforward DC-based spin-current transport characterization without requiring high-frequency excitation, although the extracted θ_{SH} is sensitive to the accuracy of the spin diffusion length and interfacial spin transparency.

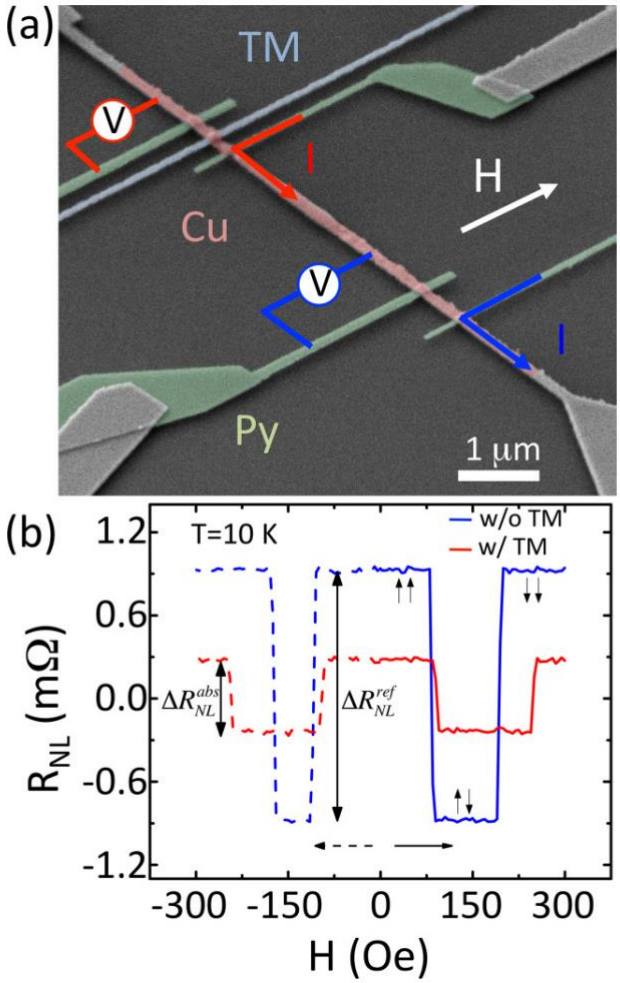

Figure 4.3. (a) Schematic of the LSV geometry used by Isasa et al. to evaluate θ_{SH} via the spin absorption method. A pure spin current is injected from a ferromagnetic electrode into a nonmagnetic channel[29]. (b) ISHE measurement configuration in Pt/Au absorption wires for determining spin Hall conductivity and θ_{SH}. Figure adapted from Ref. 29 with permission from APS.

Spin pumping employs ferromagnetic resonance in a ferromagnet/heavy-metal bilayer to generate a pure spin current, which is subsequently converted into a transverse charge voltage through the inverse spin Hall effect in the heavy metal. Azevedo et al. investigated spin pumping in NiFe/Pt bilayers and demonstrated that the measured dc voltage under FMR consists of two distinct contributions: the spin-pumping-induced ISHE voltage and an AMR mixing voltage arising from microwave-induced rf currents. As illustrated in their measurement configuration (Fig. 4.4 in Ref. 30), systematic separation of the symmetric (spin pumping) and AMR Lorentzian components enables quantitative extraction of the spin mixing conductance, spin-diffusion length, and the spin Hall angle of Pt.[30] The method offers the advantages of contactless spin-current generation and straightforward device preparation; however,

accurate determination of θ_{SH} requires careful modeling of damping enhancement, interface spin-mixing conductance, and suppression of spurious thermoelectric contributions.

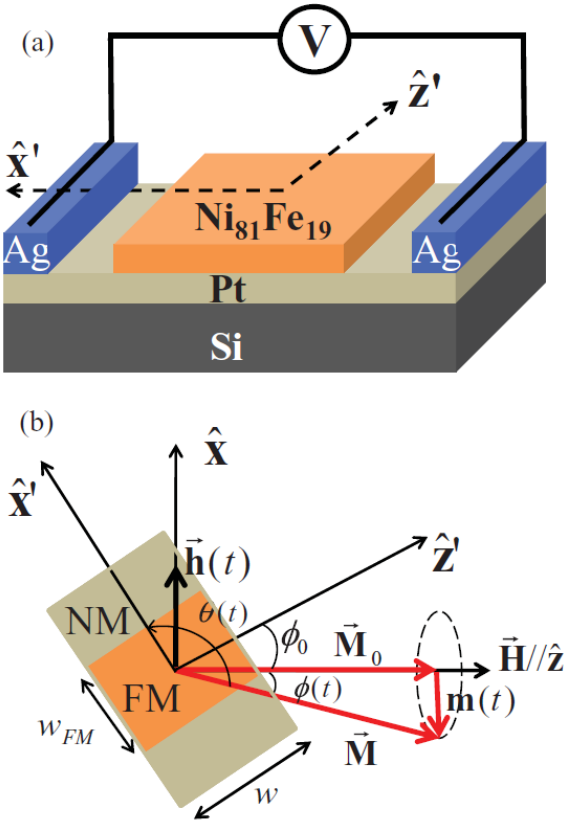

Figure 4.4. (a) Spin pumping measurement setup for NiFe/Pt bilayers. FMR is driven by microwave excitation, generating a spin current into Pt. (b) Detection of the ISHE voltage in Pt as a function of microwave frequency and power for extracting θ_{SH}. Figure adapted from Ref. 30 with permission from APS.

SSE provides a thermally driven route for generating spin currents in magnetic insulators, which can be detected in an adjacent metal layer through the inverse spin Hall effect. In a typical longitudinal SSE geometry, a temperature gradient applied across a ferromagnetic insulator such as YIG drives a magnon-mediated spin current toward the interface, where it is converted into a transverse electric field in the metal via the ISHE. Uchida et al. first demonstrated this mechanism using Pt and Nb wires deposited on a YIG slab, and the corresponding device structure is illustrated in Fig. 4.5[31]. They showed that the opposite-sign SSE voltages in these metals can be exploited to construct a Pt/Nb spin-Hall thermopile with an order-of-magnitude enhancement in the detected ISHE voltage[31]. Subsequent studies by Weiler et al. and Miao et al. confirmed that SSE-induced ISHE voltages can be used to qualitatively assess spin–charge conversion efficiency in heavy metals such as Pt, with reported θ_{SH} values on the

order of 0.02–0.03[32,33]. While SSE enables contactless and thermally driven spin-current generation, quantitative determination of θ_{SH} remains challenging due to uncertainties in thermal gradients, interfacial heat flow, and parasitic thermoelectric effects such as the ANE[34].

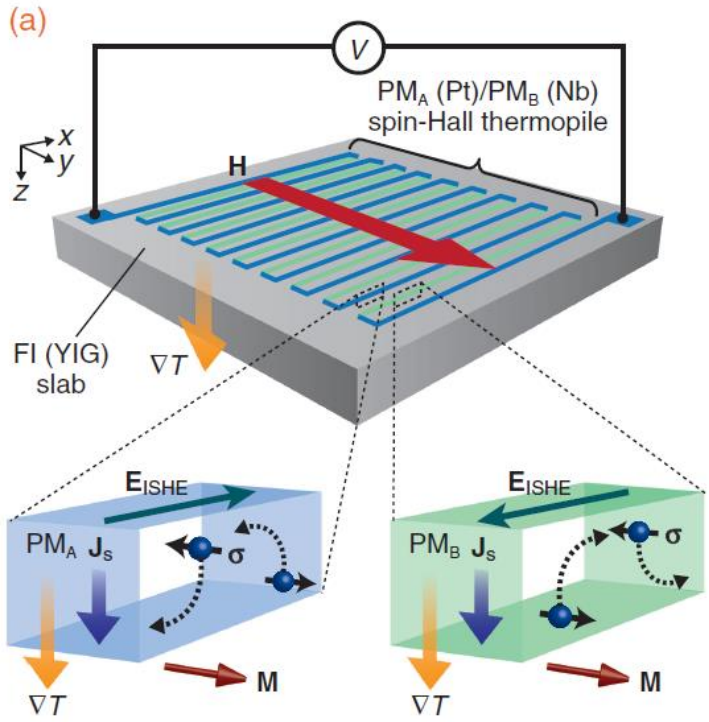

Figure 4.5. Schematic of the longitudinal SSE configuration in YIG/heavy-metal bilayers. A temperature gradient applied across the YIG layer drives a magnon-mediated spin current, which is converted into a transverse voltage via the ISHE in the heavy metal layer. Figure adapted from Ref. 31 with permission from IOP Publishing.

These complementary approaches have collectively advanced the understanding of θ_{SH} and its dependence on material properties and external parameters such as temperature. A concise summary of these techniques, including their principles, advantages, limitations, and representative studies, is provided in Table 4.1.

Table 4.1. Summary of representative techniques for evaluating the θ_{SH}.

Method	Principle	Advantages	Limitations
SHT	Tunneling junction detects spin-dependent DOS; ISHE/DSHE suppress AHE and AMR	Eliminates magnetic proximity and parallel conduction; robust over wide T	Complex tunnel junction fabrication; requires accurate spin relaxation length
ST-FMR	RF current excites magnetization precession; DC mixing voltage from AMR	In situ calibration; frequency-resolved; compatible with microfabrication	Sensitive to FM thickness; requires spin diffusion modeling; interfacial effects
Spin valves	Nonlocal spin injection into NM channel; ISHE in absorber	Direct spin current transmission; no RF needed	Complex multilayer interfaces; θ_{SH} depends on spin diffusion length
Spin pumping	FMR-driven spin current; ISHE in HM layer	Contactless spin injection; simple device fabrication	Requires accurate spin mixing conductance; thermoelectric artifacts possible
SSE	Thermal gradient drives magnon spin current; ISHE detection	Avoids electrical excitation artifacts; probes spin-thermal coupling	Susceptible to ANE and other thermal artifacts; careful calibration needed

As summarized in Table 4.1, each method offers distinct benefits and challenges, and the choice of technique often depends on the specific material system and experimental objectives.

Alternatively, the direct detection of SA at the interface provides another route, which we have previously implemented using a DSH sensor architecture. This approach directly measures the electrochemical potential difference between the spin–orbit material and the adjacent magnetic layer under in-plane current injection.

In our earlier work using a $Bi_{0.85}Sb_{0.15}$/interlayer/$Co_{0.3}Fe_{0.7}$ heterostructure, θ_{SH} was evaluated by both second harmonic Hall analysis and SA measurement, yielding vastly different results: $\theta_{SH} \sim 3.5$

from the second harmonic measurement, compared with $\theta_{SH} \sim 164$ from SA analysis. This discrepancy raises fundamental questions about the physical meaning of θ_{SH} values derived from different experimental approaches.

This systematic review of established techniques, together with the introduction of the direct spin Hall sensor approach, provides the methodological foundation for the experimental investigation presented in the following sections. In the next section, we describe the device fabrication, measurement setup, and experimental procedures employed for evaluating θ_{SH} in BiSb/CoFe heterostructures, which form the basis for the comparative analysis discussed later in this chapter.

4.2. Experimental Methods

4.2.1. Sample Fabrication and Structure Characterization

Figure 4.6 (a) presents the schematic layer structure of the fabricated sample. The multilayer stack consisted of a buffer layer (3.6 nm)/BiSb (10 nm)/interlayer (1.2 nm)/CoFe (1.5 nm)/NiFeGe (4 nm) capping layer, which was deposited on thermally oxidized silicon substrates using magnetron sputtering. The buffer layer was introduced to promote the growth of the BiSb (012) orientation, following the procedure reported in Ref. 35. The TI layer consisted of BiSb with a nominal composition of $Bi_{85}Sb_{15}$.

Figure 4.6 (b) shows the XRD patterns of the BiSb layer in this work and the previous study (Ref. 22). The BiSb layer exhibits predominant (012) orientation with a minor (001) component. Compared to the previous work, the (012) peak intensity is reduced, indicating a weaker BiSb (012) texture.

The FM layer was a CoFe alloy composed of 30% Co and 70% Fe. The interlayer was designed as a hybrid NiFeGe (0.9 nm)/MgO (0.3 nm) bilayer, serving as a diffusion barrier to suppress Sb out-diffusion from the TI layer. The high-resistivity capping layer was employed to protect the CoFe layer from oxidation and to avoid shunting of the in-plane bias current.

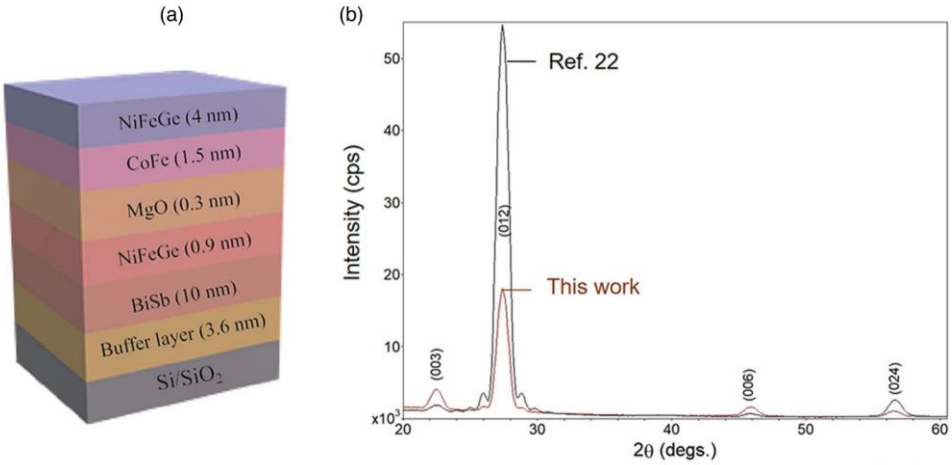

Figure 4.6. (a) Schematic illustration of the sample used in this work. (b) XRD patterns of the BiSb layer in this work and the previous work (Ref. 22).

4.2.2. Device Design for SOT, SMR, and SA Measurements

Two types of devices were patterned from the same film stack to separately investigate SOT, SMR, and SA effects. For SOT and SMR measurements, six-terminal Hall bar devices with lateral dimensions of 10 μm × 25 μm were fabricated using photolithography and Ar-ion milling, as shown in Fig. 4.7.

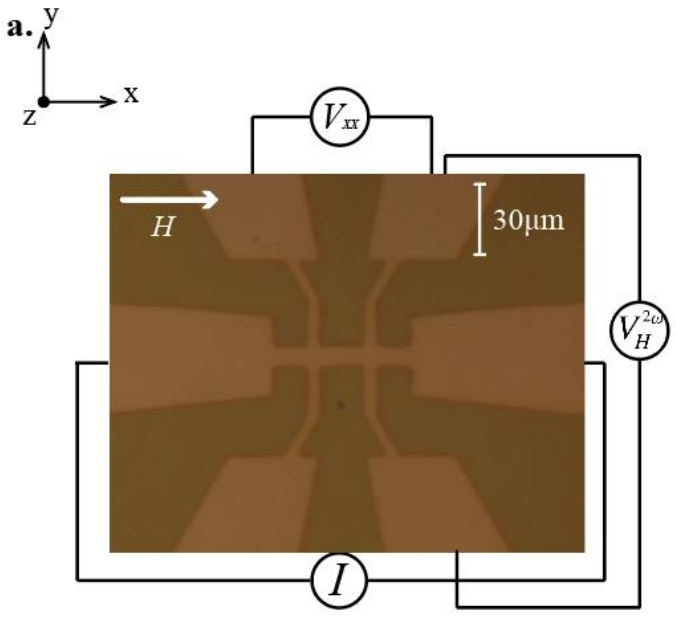

Figure 4.7. Optical micrograph and wiring configuration of the Hall bar device used for SOT and SMR measurements. The in-plane magnetic field *H* was applied along the x-direction, while the longitudinal voltage V_{XX} and second-harmonic transverse voltage $V_H^{2\omega}$ were simultaneously measured under an applied current *I*.

For SA measurements, a distinct four-terminal planar device was fabricated (Fig. 4.8). The fabrication process began with defining a 50 μm-wide channel using photolithography and ion milling, followed by the formation of two 50 μm × 50 μm CoFe/capping layer pillars through an additional ion milling step down to the BiSb surface. An OMR negative photoresist was applied as an insulating layer, after which Ta (20 nm)/Pt (10 nm) electrodes were deposited on the pillars to form top contacts.

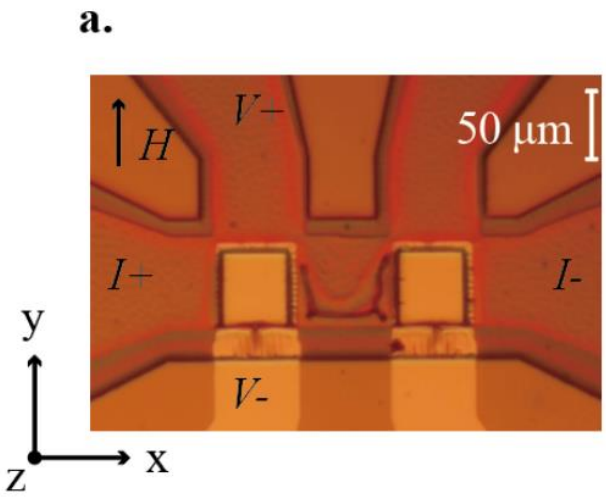

Figure 4.8. Optical micrograph of the planar device for SA measurements. The top electrodes (V_+, V_-) and current leads (I_+, I_-) are indicated.

To investigate angle-dependent magnetoresistance, the magnetic field was rotated in three orthogonal planes (yz, xz, and xy), enabling separation of SMR[36-38] and AMR contributions, as illustrated in Fig. 4.9.

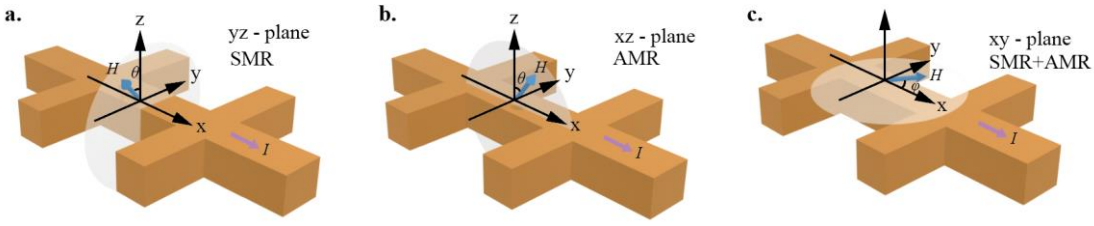

Figure 4.9. Schematic illustration of angle-dependent magnetoresistance measurements in three rotation planes: (a) yz-plane, where the magnetic field *H* is rotated by an angle *θ* with respect to the z-axis to probe SMR; (b) xz-plane, where *H* is rotated by an angle *θ* with respect to the x-axis to probe AMR; and (c) xy-plane, where *H* is rotated by an angle *φ* with respect to the x-axis to simultaneously capture SMR and AMR contributions.

4.3. Results

4.3.1. Second Harmonic Hall Measurement of Spin–Orbit Torque

The SOT efficiency of the BiSb/CoFe heterostructures was first evaluated using the second harmonic Hall (2ω) measurement technique. Figure 4.7 shows an optical micrograph of the fabricated Hall bar device, along with the defined coordinate axes and the measurement configuration. This geometry enables the characterization of both the AHE and the second harmonic Hall resistance, which are essential for the SOT analysis.

Figure 4.10 presents the anomalous Hall resistance R_{AHE} of the device, measured with a direct current of 0.1 mA applied along the xx-direction, while sweeping a perpendicular magnetic field H_z from +15 kOe to –15 kOe. From the R_{AHE}–H_z loop, R_{AHE} = 2 Ω and the magnetic anisotropy field H_k = 11.7 kOe were extracted. These parameters are used in the subsequent SOT evaluation.

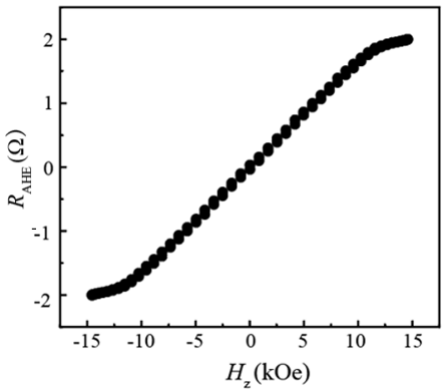

Figure 4.10. The anomalous Hall resistance measured with a perpendicular magnetic field.

Second harmonic Hall voltage measurements were then performed using an alternating excitation current of 259.68 Hz, while sweeping an in-plane magnetic field H_x along the x-direction from + 10 kOe to - 10 kOe to extract the damping-like SOT component. Figure 4.11 shows the measured second harmonic Hall resistance $R_H^{2\omega}$ at different excitation currents, which were fitted using the following expression[25]:

$$R_H^{2\omega} = \frac{R_{AHE}}{2} \cdot \frac{H_{AD}}{H_x + H_K} + R_{ONE} H_x + R_{ANE+SSE} \tag{4.1}$$

Here, H_{AD} is the effective damping-like SOT field, while R_{ONE} and $R_{ANE+SSE}$ represent the contributions from the ONE and the combined ANE and SSE, respectively.

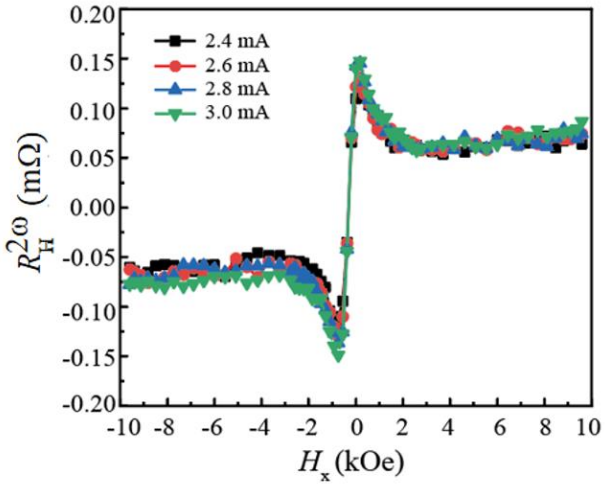

Figure 4.11. The second harmonic Hall resistance measured with various a.c. at room temperature.

Figure 4.12 shows the extracted H_{AD} as a function of the BiSb current density J_{BiSb}. The effective spin Hall angle for SOT, θ_{SH}^{SOT}, was calculated according to:

$$\theta_{SH}^{SOT} = \frac{2e}{\hbar} \cdot \frac{M_S t_{FM} H_{AD}}{J_{BiSb}} \tag{4.2}$$

where e is the elementary charge, $\hbar$ is the reduced Planck constant, t_{FM} = 1.5 nm is the thickness of the CoFe layer, M_s = 1850 emu/cm^3 is the saturation magnetization of CoFe, and J_{BiSb} is the current density in the BiSb layer.

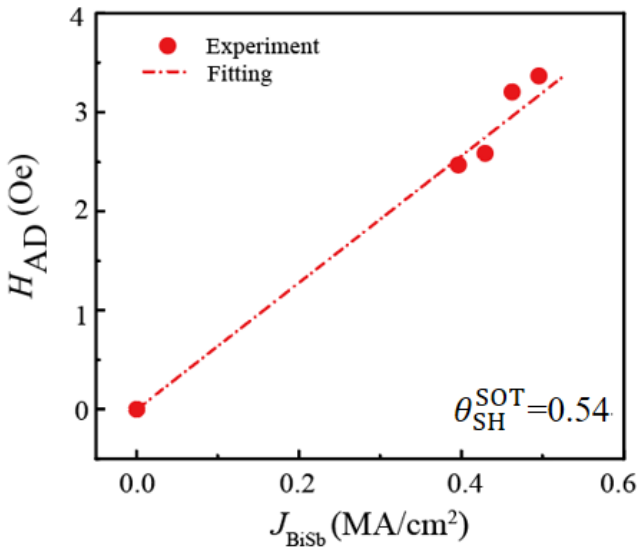

Figure 4.12. The antidamping-like field H_{AD} as a function of the current density J_{BiSb}.

For the present sample, θ_{SH}^{SOT} was estimated to be approximately 0.54 at room temperature (300 K), which is smaller than θ_{SH}^{SOT} ~ 3.5 observed in our previous work. It has been demonstrated that θ_{SH}^{SOT} strongly depends on the surface roughness and the the BiSb (012) texture of the BiSb layer[24,39]. The smaller θ_{SH}^{SOT} of this sample can be explained by the larger surface roughness (9.9 Å) and the weaker BiSb (012) texture comparing with those in the previous work[22].

Additional measurements were conducted at lower temperatures from 300 K down to 50 K. However, due to the slight increase of H_k at low temperatures and the dominant $R_{ANE+SSE}$ contribution, the second harmonic signal originating from SOT (first term in Eq. 4.1) becomes too weak below 200 K. Consequently, reliable extraction of θ_{SH}^{SOT} was only possible down to 200 K.

In summary, the second harmonic Hall measurement provides a reliable estimation of θ_{SH}^{SOT} in BiSb/CoFe heterostructures at temperatures above 200 K, yielding a value of approximately 0.54 at room temperature. However, the increasing magnetic anisotropy field and the dominant thermoelectric contributions at lower temperatures limit the applicability of this method in the cryogenic regime. To complement the SOT-based analysis and further investigate the origin of the large spin Hall angle in BiSb, we employed direct SA measurements, as described in the following section.

4.3.2. Spin Accumulation Voltage Measurement

The spin Hall angle of the BiSb/CoFe heterostructures was further evaluated using the SA method. For the device shown in Fig. 4.8, a direct current I_{SA} = 0.2 mA was applied along the x-direction while an external magnetic field was swept along the y-direction. The spin accumulation voltage V_{SA} was measured between the top electrode and the bottom BiSb layer.

Figure 4.13 shows the spin accumulation resistance $\Delta R_{SA} = \Delta V_{SA}/I_{SA}$ as a function of temperature from 300 K down to 50 K, where Δ denotes the amplitude (half of the peak-to-peak signal) of the hysteresis curves. A monotonic increase in ΔR_{SA} was observed with decreasing temperature: ΔR_{SA} increased from approximately 1.3 mΩ at 300 K to 2.8 mΩ at 50 K.

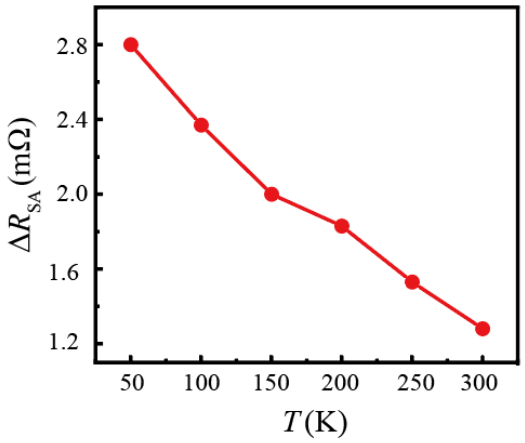

Figure 4.13. Temperature dependence of the spin accumulation resistance.

Figures 4.14 (a) and 4.14 (b) present representative ΔR_{SA} hysteresis loops measured at 300 K and 50 K, respectively. It is worth noting that a sample with a relatively low spin Hall angle was intentionally chosen for this work, resulting in reduced spin-orbit torque noise in the ΔR_{SA} hysteresis curves compared with devices exhibiting a giant spin Hall angle reported in our previous studies.

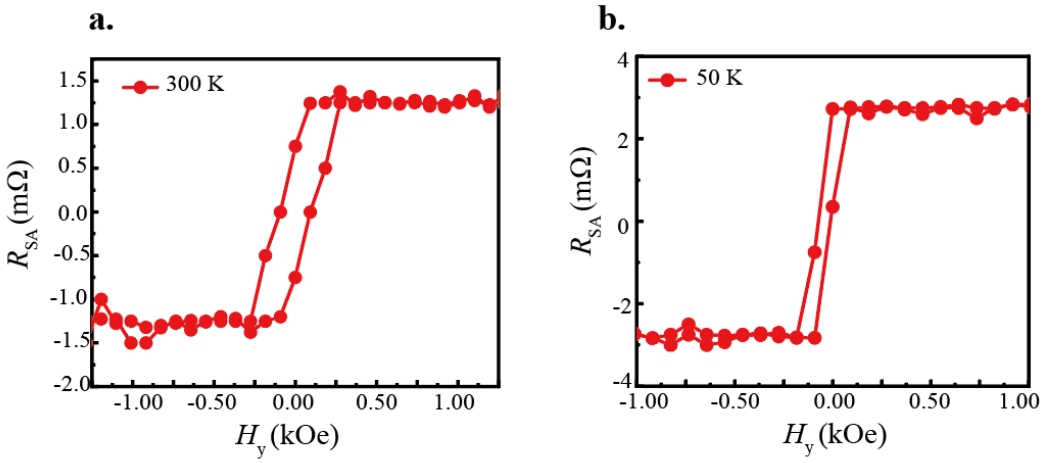

Figure 4.14. (a), (b) Spin accumulation resistance hysteresis curves at 300 K and 50 K, respectively.

The spin Hall angle θ_{SH}^{SA} was extracted from the SA measurements using the following relation[22,40]:

$$\Delta R_{SA} = \frac{\Delta V_{SA}}{I_{SA}} = \frac{\theta_{SH}^{SA} P R_{sheet}^{stack}}{w} \lambda_{sf} \tanh\left(\frac{t_S}{\lambda_{sf}}\right) \tag{4.3}$$

where P = 0.5 is the spin polarization of CoFe, R_{sheet}^{stack} is the sheet resistance of the full stack at each temperature, w = 50 μm is the device width, $t_S \sim \lambda_{sf}$ = 2 nm represents the topological surface thickness and spin diffusion length of BiSb[41], respectively. For low-temperature measurements, λ_{sf} was assumed

to be constant, which is reasonable because the resistivity (or momentum relaxation time) of the surface-dominated conduction in 10 nm - thick BiSb is nearly temperature-independent over the range 4 - 300 K.

In summary, the SA method reveals a monotonic increase in θ_{SH}^{SA} with decreasing temperature, consistent with enhanced spin-orbit coupling and surface-dominated transport in BiSb at low temperatures. Compared with the second harmonic Hall analysis, the SA measurement provides a larger θ_{SH} value due to its direct detection of spin accumulation at the interface. To further cross-validate these observations and assess the spin Hall angle from a different perspective, we performed SMR measurements, as described in the following section.

4.3.3. Spin Hall Magnetoresistance Measurement

The SMR of the BiSb/CoFe heterostructures was measured using the Hall bar device. The magnetic field angular dependence of the longitudinal resistance variation ΔR_{xx} was characterized under three magnetic field rotation configurations:

(i) yz-plane rotation (SMR-dominant),

(ii) xz-plane rotation (AMR-dominant), and

(iii) xy-plane rotation (combined SMR and AMR contributions).

Figure 4.9 schematically illustrates the experimental configuration used to evaluate the angular dependence of the longitudinal resistance variation ΔR_{xx} under three magnetic-field rotation planes: yz-plane (SMR dominant), xz-plane (AMR dominant), and xy-plane (combined SMR and AMR contributions). The external magnetic field was fixed at $H_k = 9$ kOe during the measurement. Figure 4.15 presents a representative angular dependence of ΔR_{xx} measured at 300 K. The resistance changes were 0.33 Ω, 0.24 Ω, and 0.013 Ω for the xy-, yz-, and xz-plane scans, respectively.

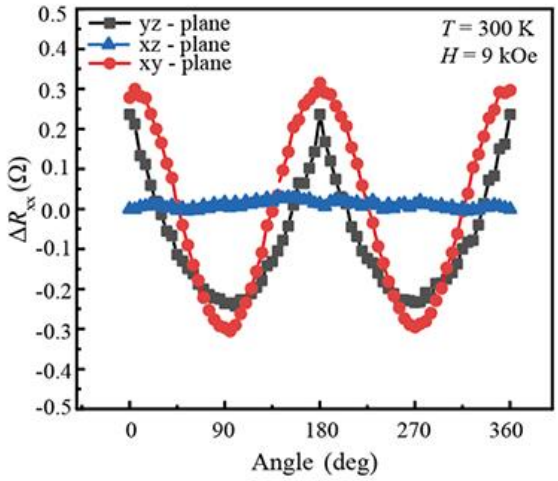

Figure 4.15.

Figure 4.15. Angular dependence of the longitudinal resistance variation ΔR_{xx} measured at $T = 300$ K under an external magnetic field of $H = 9$ kOe for magnetic-field rotations in the xy, yz, and xz planes.

In the ideal case of full magnetization saturation, the SMR and AMR components satisfy the additive relation[42]:

$$\Delta R_{xx}(xy) = \Delta R_{xx}(yz) + \Delta R_{xx}(xz) \tag{4.4}$$

and the SMR amplitude is directly given by $\Delta R_{xx}(yz)$.

However, since the magnetic anisotropy field of the sample is H_k = 11.7 kOe at 300 K, which is larger than the maximum available rotation field (H = 9 kOe), full saturation along the z-direction could not be achieved. As a result, $\Delta R_{xx}(yz)$ does not represent the intrinsic SMR signal. The angular dependence of SMR in the unsaturated regime can be expressed as：

$$\Delta R_{SMR}\left(1 - m_y^2\right) = \Delta R_{SMR} m_z^2 \tag{4.5}$$

When the magnetic field is not strong enough to saturate the magnetization along the z direction, the maximum of the SMR curve only reaches:

$$\Delta R_{SMR}\left(1 - m_y^2\right) = \Delta R_{SMR} m_z^2 = \Delta R_{SMR}\left(\frac{H}{H_k}\right)^2 \tag{4.6}$$

Using H = 9 kOe and H_k = 11.7 kOe, we obtain a scaling factor $(9/11.7)^2 \approx 0.591$. Therefore, the intrinsic SMR value is estimated as: $\Delta R_{SMR} = \frac{\Delta R_{xx}(yz)}{0.591}$. Figure 4.16 shows the temperature dependence of ΔR_{xx} for the three rotation planes and the extracted ΔR_{SMR}. As the temperature decreases from 300 K to 50 K, all ΔR_{xx} values show an upward trend. However, the change of $\Delta R_{xx}(xz)$, i.e., the AMR component, is much smaller compared with those of $\Delta R_{xx}(yz)$, $\Delta R_{xx}(xy)$, and the calculated ΔR_{SMR}. Specifically,

ΔR_{xx}(yz) increases from 0.24 to 0.37 Ω, ΔR_{xx}(xy) from 0.30 to 0.52 Ω, and ΔR_{SMR} from 0.4 to 0.6 Ω. This enhancement of SMR at low temperatures indicate that the spin Hall effect from the topological surface states becomes more dominant at lower temperatures.

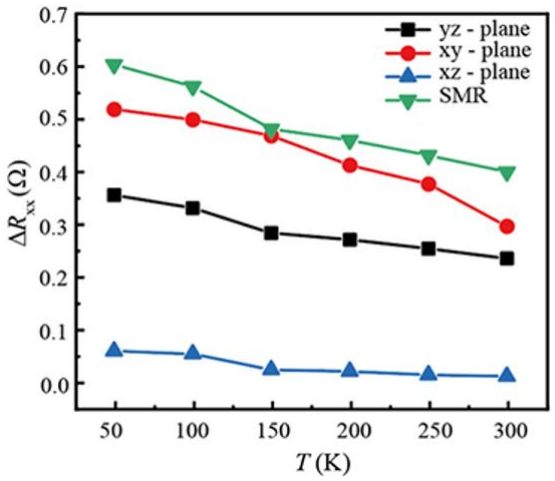

Figure 4.16. Temperature dependence of the longitudinal resistance variation ΔR_{xx} for magnetic-field rotations in the yz, xz, and xy planes, together with the extracted SMR contribution.

The spin Hall angle θ_{SMR}^{SH} was evaluated from the SMR data using the following relation:

$$\frac{2\Delta R_{SMR}}{R_{xx}^{0}} = \theta_{SH}^{2}\frac{\lambda_{sf}}{t_s}\frac{\tanh^2\left(\frac{t_s}{2\lambda_{sf}}\right)}{1+\xi}\left[\frac{g_R}{1+g_R\coth\left(\frac{t_s}{\lambda_{sf}}\right)}-\frac{g_F}{1+g_F\coth\left(\frac{t_s}{\lambda_{sf}}\right)}\right] \tag{4.7}$$

where R_{xx}^{0} is the minimum longitudinal resistance of the Hall bar, and $\xi = \frac{\rho_{other}t_{BiSb}}{\rho_{BiSb}t_{other}}$ is the current shunting factor between the BiSb layer and the other layers. Here, ρ_{BiSb} and t_{BiSb} are the resistivity and thickness of the BiSb layer, and ρ_{other}, t_{other} are those of the other layers. g_R and g_F correspond to the transverse and longitudinal spin absorption factors, respectively, with $g_R = 2\rho_s\lambda_{sf}Re[g_{mix}^{\uparrow\downarrow}]\coth\left(\frac{t_s}{\lambda_{sf}}\right)$, and $g_F = \frac{(1-P^2)\rho_s\lambda_{sf}\coth\left(\frac{t_s}{\lambda_{sf}}\right)}{\rho_F\lambda_F\coth\left(\frac{t_F}{\lambda_F}\right)}$. The first term in the bracket of Eq. (4.7) represents transverse spin current absorption, whereas the second term corresponds to longitudinal spin absorption by the CoFe layer. We can rewrite Eq. (4.7) as:

$$\frac{2\Delta R_{SMR}}{R_{xx}^{0}} = \theta_{SH}^{2}\frac{\lambda_{sf}}{t_s}\frac{\tanh^2\left(\frac{t_s}{2\lambda_{sf}}\right)}{1+\xi}\left[1-\frac{1}{\coth\left(\frac{t_s}{\lambda_{sf}}\right)}\right]\left[\frac{G_R}{1+G_R}-\frac{G_F}{1+G_F}\right] \tag{4.8}$$

where $G_R = g_R \coth\left(\frac{t_S}{\lambda_{sf}}\right)$, $G_F = g_F \coth\left(\frac{t_S}{\lambda_{sf}}\right)$. Under the condition of $G_R \gg 1$, Eq. (4.8) can be further simpilifer to:

$$\frac{2\Delta R_{SMR}}{R_{xx}^{0}} = \theta_{SH}^{2}\frac{\lambda_{sf}}{t_s}\frac{\tanh^2\left(\frac{t_s}{\lambda_{sf}}\right)}{1+\xi}\left[1-\frac{1}{\cosh\left(\frac{t_s}{\lambda_{sf}}\right)}\right]\frac{1}{1+G_F} \tag{4.9}$$

This form is equivalent to the conventional SMR model with an additional correction factor 1/ (1 + G_F) that accounts for longitudinal spin current absorption by the CoFe layer.

To evaluate the G_F as a function of temperature, the following material parameters for CoFe were used[43]: $\rho_F(300\ K) = 31.4\ \mu\Omega\cdot cm$, $\rho_F(T) = \rho_F(300\ K)\ [1+\alpha(T\text{-}300\ K)]$, with $\alpha = 1.67 \times 10^{-3}\ K^{-1}$. This diffiuction length was set to $\lambda_F(300\ K) = 10$ nm, $\lambda_F(T)/\lambda_F(300\ K) = \rho_F(300\ K)/\rho_F(T)$ based on the Eillott-Yafet spin flip mechanism. The spin polarization P was assumed to increas linearly from 0.5 at 300 K to 0.9 at 50 K[37,44,45].

For BiSb, the measured values were $\rho_{BiSb} = 777\ \mu\Omega\cdot cm$ and $\rho_s = 311\ \mu\Omega\cdot cm$, which are nearly temperature independent for 10 nm thick BiSb due to surface-state-dominated trasport[44]. The current shunting factor ξ was obtained from the measured full-stack resistivity at low temperatures.

4.3.4. Comparative Analysis and Temperature Dependence of Spin Hall Angles measured by SA, SMR and SOT

Figure 4.17 presents the temperature dependence of the normalized spin accumulation resistance $\Delta R_{SA}/\Delta R_{SA}(300\ K)$ and normalized spin Hall magnetoresistance $\Delta R_{SMR}/\Delta R_{SMR}(300\ K)$ in BiSb/CoFe heterostructures over the range of 50 - 300 K. Both quantities increase monotonically as the temperature decreases, indicating an enhanced spin Hall angle at lower temperatures.

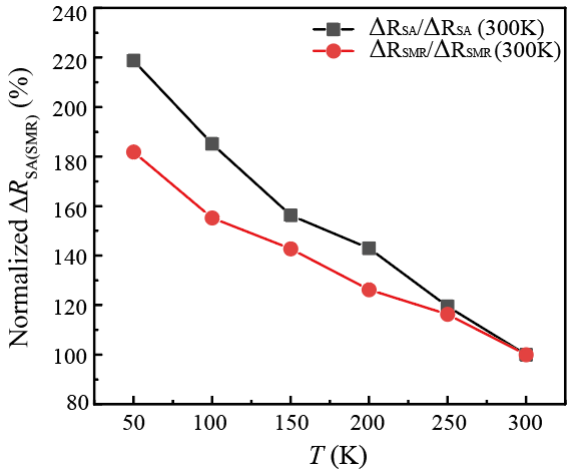

Figure 4.17. Temperature dependence of the normalized spin accumulation resistance $\Delta R_{SA}/\Delta R_{SA}$(300 K) and spin Hall magnetoresistance $\Delta R_{SMR}/\Delta R_{SMR}$(300 K) for BiSb/CoFe heterostructures. Both quantities increase as temperature decreases, indicating an enhanced spin Hall angle at lower temperatures.

Figure 4.18 summarizes the temperature dependence of the effective spin Hall angle θ_{SH} determined by the three experimental techniques: SA, SOT, and SMR. All three methods show a clear increase in θ_{SH} with decreasing temperature, consistent with the spin Hall effect dominated by topological surface states.

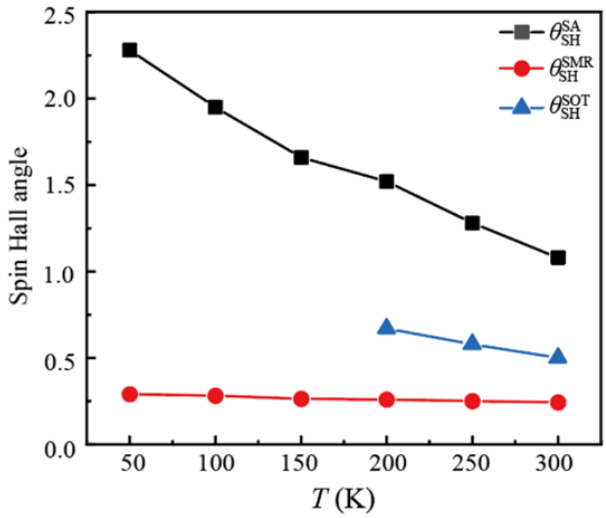

Figure 4.18. Temperature dependence of the spin Hall angle θ_{SH} in BiSb/CoFe heterostructures determined by SA, SOT, and SMR measurements. The SA-derived θ_{SH} values are consistently the largest and exhibit the strongest temperature dependence, followed by SOT, with SMR yielding the smallest values.

Among the three techniques, the SA method yields the largest θ_{SH} values and exhibits the strongest temperature dependence, increasing from approximately 1.1 at 300 K to 2.3 at 50 K. The SMR-derived

θ_{SH}^{SMR} also increases with decreasing temperature, but its rate of change is smaller than that of SA, ranging from approximately 0.22 at 300 K to 0.26 at 50 K. The SOT-derived θ_{SH}^{SOT} values lie between those obtained from SA and SMR.

Overall, θ_{SH}^{SA} remains consistently higher than θ_{SH}^{SMR} and θ_{SH}^{SOT} when using the same spin diffusion length parameter λ_{sf} = 2 nm in Eqs. (4.3) and (4.4). This systematic difference highlights the intrinsic discrepancies among the techniques, which are likely associated with their different sensitivities to interfacial transparency, spin backflow, and surface-dominated conduction.

To provide a concise summary of the quantitative results and their temperature dependence, Table 4.2 compares the spin Hall angles obtained from SA, SOT, and SMR measurements at representative temperatures. The table highlights the relative magnitudes, absolute values, and variation trends for each method, serving as a compact reference for the comparative analysis.

Table 4.2. Comparison of spin Hall angle θ_{SH} determined by different measurement techniques in BiSb/CoFe heterostructures.

Method	θ_{SH} at 300 K	θ_{SH} at 50 K	Temperature Dependence	Relative Magnitude
SA	~1.1	~2.3	Strong increase with decreasing T	Highest
SOT	~0.54	~1.1	Moderate increase with decreasing T	Intermediate
SMR	~0.22	~0.26	Weak increase with decreasing T	Lowest

In summary, the spin Hall angle of BiSb/CoFe heterostructures was evaluated using three complementary methods: SOT-based second harmonic Hall analysis, direct SA measurement, and SMR measurement. All three approaches consistently demonstrate an enhancement of θ_{SH} at lower temperatures, in agreement with spin-orbit coupling effects governed by the topological surface states of BiSb. Among them, the SA method yields the largest θ_{SH} values, followed by SOT, with SMR producing the smallest values. This trend underscores the importance of the measurement technique in determining θ_{SH} and suggests that the apparent magnitude of the spin Hall angle depends strongly on the specific physical mechanism probed by each method.

The comparative results obtained from SA, SOT, and SMR measurements provide important insight into the influence of experimental methodology on the extracted spin Hall angle. In the next section, we

discuss the physical origins of these discrepancies, focusing on the roles of interfacial spin transparency, bulk versus surface contributions, and possible extrinsic effects.

4.4. Discussion

4.4.1. Origin of the Discrepancy among SA-, SOT-, and SMR-derived Spin Hall Angles

The discrepancy in θ_{SH}^{SA}, θ_{SH}^{SOT}, and θ_{SH}^{SMR} arises from the distinct spin-transport boundary conditions and interface physics probed by each technique. A consistent way to compare them is to use a conductance-based description of interlayer/interface spin transmission.

1. SOT measurement and interlayer/interface transparency

For the SOT method, θ_{SH}^{SOT} depends on the fraction of spin current absorbed by the FM layer from the SOT layer through the interlayer. This value can be smaller than the intrinsic spin Hall angle θ_{SH}, and can be expressed as $\theta_{SH}^{SOT} = T_{IST} * \theta_{SH}$, T_{IST} (≤ 1) is the interlayer spin transparency. The spin current must first transport through the interlayer, where its transmission depends on the spin transport time τ_t.[47,48] Upon reaching the interlayer/FM interface, a portion of the spins may be lost via spin-flip scattering or may be transferred into the FM layer. This process is represented by the spin mixing time $\tau_{mix} \sim \frac{1}{g_{mix}^{\uparrow\downarrow}}$, where $g_{mix}^{\uparrow\downarrow}$ is the mixing conductance at the interface.

The spin transparency factor can be approximated as $T_{IST} \sim \frac{1}{\tau_t + \tau_{mix}}$, where a shorter τ_{mix} leads to higher spin absorption in the FM layer.[23,49] In practical terms, insulating interlayers with higher barrier heights tend to yield smaller θ_{SH}^{SOT}, as observed when the MgO interlayer was replaced by $Mg_{1-x}Ti_xO$ with higher TiO composition. In addition, if the FM layer is too thin compared to its spin diffusion length, the spin current reaching the FM interface may not be fully absorbed, with the residual spin current diffusing into the capping layer. Consequently, θ_{SH}^{SOT} is often an underestimated value of the intrinsic θ_{SH}. Nevertheless, θ_{SH}^{SOT} remains a valuable parameter for evaluating the effective torque acting on the FM layer and is critical for device applications such as SOT-MRAM or spin-torque oscillators.

2. SMR and spin reflection

SMR originates from the modulation of spin reflection at the NM/interlayer/FM interface as the magnetization direction varies. The longitudinal resistivity of the NM (SOT) layer can be expressed approximately as[37]:

$$\frac{\Delta\rho}{\rho} \approx -\theta_{SH}^{2}\left(\frac{2\lambda}{t_{NM}}\right)\tanh^{2}\left(\frac{t_{NM}}{2\lambda}\right)\frac{2\lambda\rho G_r}{\left[1+2\lambda\rho G_r \coth\left(\frac{t_{NM}}{\lambda}\right)\right]^{2}+\left[2\lambda\rho G_i \coth\left(\frac{t_{NM}}{\lambda}\right)\right]^{2}} \tag{4.11}$$

where G_r and G_i are the real and imaginary parts of the interfacial spin-mixing conductance.

Compared with SOT, several key differences arise.

(1) The SMR signal scales quadratically with the spin Hall angle θ_{SH}, so any uncertainty in G_r, λ, or ρ leads to a strong underestimation of θ_{SH}^{SMR} during parameter extraction.

(2) SMR is governed by spin reflection, whereas SOT originates from spin transmission (absorption). Although both effects share interfacial parameters ($g^{\uparrow\downarrow}$, G_{ext}), they involve different boundary conditions for spin current flow.

(3) Because of the strong parameter sensitivity and saturation of the reflection term, experimentally extracted θ_{SH}^{SMR} is typically smaller than θ_{SH}^{SOT}.

This can be understood physically as follows: when the magnetization vector is perpendicular to the spin polarization ($m \perp s$), spin absorption at the NM/interlayer/FM interface is maximized and spin reflection is minimized, resulting in the largest longitudinal resistivity modulation. Conversely, when $m \parallel s$, spin absorption is minimized, reflection is maximized, and the resistivity modulation becomes smaller. The SMR signal is therefore determined by the contrast in spin reflectivity between these two magnetization configurations, rather than by the transmitted spin current.

Interlayer properties play a critical role in controlling this reflectivity contrast. A high-resistance interlayer or one with a short spin diffusion length attenuates the spin current and suppresses both the reflected and transmitted spin components. This leads to a smaller overall SMR signal and makes the extracted θ_{SH}^{SMR} extremely sensitive to the assumed model parameters. Conversely, an optimized interlayer with appropriate thickness and spin transparency can enhance spin reflection contrast while minimizing spin-flip scattering losses, resulting in a clearer modulation signal and more reliable evaluation of θ_{SH}.

In short, while SOT measures the absorbed spin current, SMR probes the reflected component. The balance between these two channels is determined by the interface spin mixing conductance and interlayer properties, which directly dictates the magnitude and accuracy of the measured θ_{SH}^{SMR}.

3. SA measurement and intrinsic spin Hall angle

The SA technique provides a direct probe of the interfacial spin chemical potential at the surface of the SOT layer. It operates under an open spin-current boundary condition, j_s (z = 0) ≈ 0, meaning no transverse spin current is transmitted into the FM layer. As a result, the spin accumulation builds up at the interface, maximizing μ_s (z = 0). Under this condition, the measured θ_{SH}^{SA} closely approximates the intrinsic spin Hall angle of the SOT layer[35,48].

When the magnetization is parallel to the spin polarization, interfacial absorption is minimized, and the measurement becomes insensitive to $g^{\uparrow\downarrow}$, interlayer transparency, or FM thickness. Typically, the hierarchy is $\theta_{SH}^{SA} \geq \theta_{SH}^{SOT} \geq \theta_{SH}^{SMR}$.

Experimental implementation: In this work, SA signals are measured using nonlocal voltage detection between top and bottom electrodes. Because SA does not rely on spin transmission, it is far less sensitive to interfacial imperfections, providing a more intrinsic evaluation of the spin Hall effect.

4. Summary and implications

The three techniques reflect different physical processes:

Method	Physical process	Boundary condition	Interface dependence	Typical value
SOT	Spin transfer (absorption)	Partial transmission	Strong (via T_{IST})	Intermediate
SMR	Spin reflection contrast	Partial reflection	Strong and nonlinear	Lower
SA	Spin accumulation	Open circuit (j_s = 0)	Weak	Highest (intrinsic)

θ_{SH}^{SOT} is most relevant for device applications (e.g., SOT-MRAM).

θ_{SH}^{SMR} reflects interface reflection but often underestimates the true value.

θ_{SH}^{SA} best reflects the intrinsic spin Hall conversion in the SOT layer.

4.4.2. Interface Effects and Spin Transparency in BiSb/Interlayer/CoFe Heterostructures

The difference in the spin Hall angles obtained from SA, SOT, and SMR measurements is closely related to interface spin transparency and spin loss mechanisms in the BiSb/interlayer/CoFe heterostructures. Figures 4.19 schematically illustrate the fundamental physical processes involved.

(1) Spin loss in the interlayer and spin-flip scattering

When spin current propagates through the interlayer, part of the spin polarization is lost due to bulk spin-flip scattering inside the interlayer, characterized by a spin-diffusion length λ_s^{IL}, as shown in Fig. 4.19[36,50].

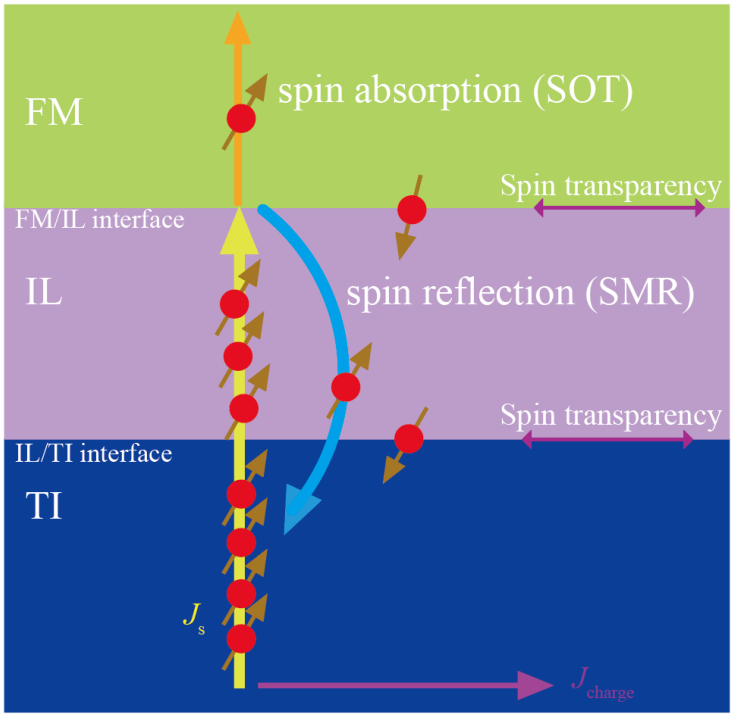

Figure 4.19. Schematic illustration of spin current generation, transmission, absorption, and reflection in a TI/interlayer/FM heterostructure.

For thin interlayers ($t_{IL} < \lambda_s^{IL}$), the spin loss is small, whereas for thick interlayers ($t_{IL} > \lambda_s^{IL}$), the spin current experiences exponential attenuation, and beyond approximately 2 - 3 λ_s^{IL}, almost no spin reaches the FM layer. Each spin-flip event destroys part of the spin polarization, resulting in a net reduction of spin current as it travels across the interlayer. This process imposes a fundamental limit on interface spin transparency and consequently suppresses the effective spin Hall angle extracted from SOT and SMR measurements.[51,52]

(2) Spin transparency at the interfaces

The spin transparency (T_{int}) at the interlayer (IL)/TI and FM/IL interfaces determines how much spin current is transmitted into the FM layer. A lower T_{int} leads to larger spin reflection and reduced spin transfer, thereby lowering the effective spin Hall angle in SOT and SA measurements. In contrast, for SMR, stronger spin reflection can enhance the detected resistance modulation, resulting in a larger

apparent θ_{SH}.[51] For SOT measurements, the spin current flows once across the IL/TI and FM/IL interfaces, leading to single-pass spin loss. For SMR measurements, because the spin current is reflected at the FM/IL interface, it traverses the interlayer twice—forward and backward—thus experiencing double-pass spin loss. In contrast, in SA measurements, the spin current does not penetrate the FM layer; instead, it accumulates at the IL/FM interface. Consequently, the spin loss only occurs within the TI and interlayer region, and no additional loss arises in the FM layer.[53]

(3) Relation to the magnitude of θ_{SH} for different measurement techniques

This difference in the number of spin-loss paths directly explains the relative magnitude of the spin Hall angles obtained by the three measurement methods:

$$\theta_{SH}^{SA} > \theta_{SH}^{SOT} > \theta_{SH}^{SMR}.$$

Spin accumulation[54,55] at the interface is observed in the SA method, as illustrated in Fig. 4.20: SA corresponds to a spin open-circuit boundary condition ($M \parallel \pm\sigma$), where no spin torque acts on the FM layer. As a result, the absorbed spin current J_s^{abs} is essentially zero, the interfacial spin accumulation is maximized, and the spin loss is minimal. Therefore, SA yields the largest spin Hall angle, closest to the intrinsic θ_{SH} of the BiSb layer.

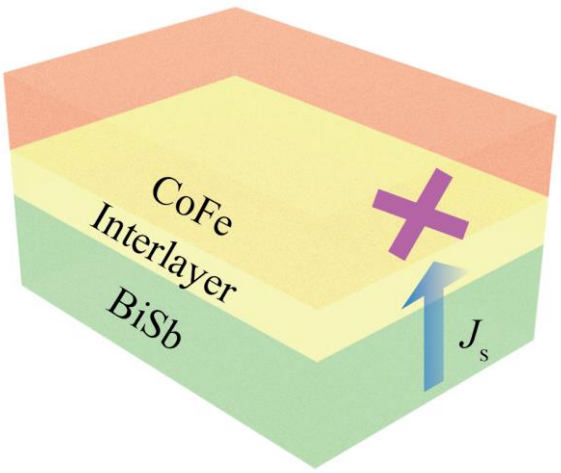

Figure 4.20. Schematic illustration of spin accumulation at the IL/FM interface under SA measurement (spin open-circuit condition).

In the SOT measurement, the magnetization is perpendicular to the spin polarization ($M \perp \sigma$), and the spin current must be absorbed by the FM layer, resulting in single-pass spin loss across the TI/IL and IL/FM interfaces. Thus, the extracted θ_{SH}^{SOT} reflects the effective torque efficiency, which is lower than the intrinsic value.

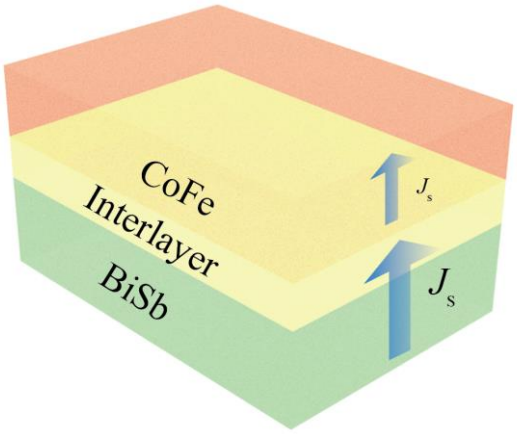

Figure 4.21. Schematic illustration of spin absorption during SOT measurement, where spin current flows across the interlayer and into the FM layer.

Spin loss at the interface is observed in the SMR method, as illustrated in Fig. 4.21:

In SMR, most of the spin current is reflected at the FM/IL interface with minimal absorption. When $M \parallel \sigma$, the SMR signal originates from the difference between the spin reflection in parallel and perpendicular magnetization configurations. Because the spin current traverses the interlayer twice, the effective spin Hall angle θ_{SH}^{SMR} is the smallest among the three.

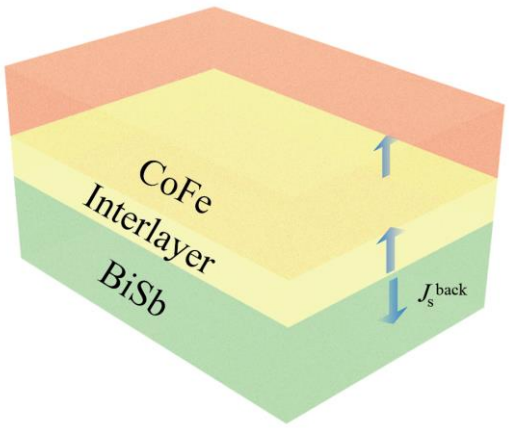

Figure 4.22. Schematic illustration of spin reflection during SMR measurement, where spin current is partially reflected at the IL/FM interface, resulting in backflow.

(4) Impact of interlayer engineering

(4.1) Physical origins of spin loss and interface control

These results highlight that the interlayer thickness, material properties, and interface quality (roughness, barrier height, chemical composition) have a critical impact on the effective spin transparency T_{IST} and consequently on the measured θ_{SH}. Optimizing the interlayer to minimize spin-flip scattering and maximize interface transparency is therefore an effective strategy to enhance the measurable spin Hall signals in SOT and SMR measurements. In TI/FM stacks based on BiSb, direct contact with the FM can induce interdiffusion (notably Sb → FM) and partial suppression of the TI surface states; inserting a proper interlayer prevents this chemical intermixing and thus preserves the intrinsic θ_{SH} of the TI layer while stabilizing the interface.[55]

Spin loss at interfaces originates primarily from three mechanisms: 1) spin-flip scattering due to magnetic or structural disorder at the interface, which randomizes spin orientation; 2) spin-memory loss associated with interfacial spin–orbit coupling, which causes partial dephasing of the spin current; and 3) mismatch of spin impedance between layers, which leads to spin backflow. These mechanisms not only attenuate the spin current amplitude but also reduce the net spin accumulation at the FM interface.[56-58] Beyond these generic channels, the interlayer also tunes two key dynamical time scales governing spin passage across the interface: the spin-transmission (tunneling/diffusion) time τ_t and the spin-mixing time τ_{mix} that is linked to the interfacial spin-mixing conductance $g_{\uparrow\downarrow}^{mix}$.

To control and minimize spin loss, interface engineering plays a decisive role. For example, using atomically smooth and chemically sharp interfaces reduces spin-flip scattering; inserting optimized spacer layers (e.g., ultrathin MgO or other insulating barriers) can suppress spin-memory loss while maintaining sufficient transparency; and matching the spin impedance between layers by tuning the interlayer thickness or conductivity can suppress spin backflow. Additionally, post-growth annealing and surface treatment can further improve interface order and reduce interfacial spin disorder. Practically, metallic interlayers (e.g., NiFeGe) tend to yield short τ_t and efficient spin transfer but may suffer from larger τ_{mix} due to interfacial disorder; oxide interlayers (e.g., MgO) introduce a tunneling barrier that increases τ_t yet provide cleaner interfaces with shorter τ_{mix}; hybrid metal–oxide designs (e.g., NiFeGe/MgO) combine both advantages—short τ_t and short τ_{mix}—and thereby maximize T_{IST} and the effective SOT efficiency.[26,59,60] Together, these approaches provide a powerful route to enhance spin transparency and approach the intrinsic spin Hall angle of the TI layer.

While the above discussion clarifies the physical origins of spin loss and the role of interlayer engineering, a quantitative evaluation of the effective spin transparency and spin loss remains nontrivial, particularly when comparing results obtained from different measurement schemes.

(4.2) Quantitative evaluation of spin transparency and spin loss across different measurement schemes

As discussed in the previous section, interlayer engineering plays a decisive role in determining the efficiency of spin transmission across TI/IL/FM heterostructures by controlling spin loss and interface transparency. However, experimentally extracted spin Hall angles often show noticeable differences depending on the measurement technique, such as SOT, SMR, and SA measurements. This raises an important question of whether these discrepancies originate from distinct spin-generation mechanisms or simply reflect different spin-transport pathways and detection sensitivities.

To address this issue, we introduce a simplified but physically consistent framework that quantitatively relates the results obtained from different measurement schemes. We assume that all three methods probe the same intrinsic spin Hall angle of the TI layer, and that the observed differences arise from spin loss in the interlayer and finite spin transparency at the IL/FM interface. Two effective parameters are introduced: the spin transparency T of the IL/FM interface, which characterizes the efficiency of spin absorption by the ferromagnetic layer, and the spin loss factor L, which represents the fractional spin-current attenuation during a single transport through the interlayer.

Within this framework, the spin accumulation measurement provides a direct estimate of the intrinsic spin Hall angle θ_{SH}^{SA}, as it does not require spin-current transmission into the ferromagnetic layer. In contrast, the SOT measurement involves a single transport through the interlayer followed by partial spin transmission across the IL/FM interface, yielding an effective spin Hall angle given by $\theta_{SH}^{SOT} = T(1-L)\theta_{SH}^{SA}$.

For the SMR measurement, the signal originates from the difference in reflected spin current between the spin-open circuit and spin-absorbing magnetization configurations. As the spin current transports through the interlayer twice and the signal reflects the difference between spin-open and spin-absorbing configurations, the corresponding SMR effective spin Hall angle becomes $\theta_{SH}^{SMR} = T(1-L)^2\theta_{SH}^{SA}$.

By applying these relations to the experimentally obtained values of θ_{SH}^{SA}, θ_{SH}^{SOT}, and θ_{SH}^{SMR}, we extract a spin loss of approximately $L = 40\%$ per transport through the interlayer and an effective IL/FM spin transparency of $T = 80\%$ under the spin-absorbing configuration. These values are consistent with

the interfacial spin-loss mechanisms discussed in Section (4), including spin-flip scattering, spin-memory loss, and spin backflow, and fall within the range reported for metallic and hybrid interlayers in previous studies.

Importantly, this analysis demonstrates that the quantitative differences among the three measurement schemes do not indicate inconsistent spin Hall physics, but rather reflect different spin-transmission pathways and detection sensitivities. The framework therefore provides a unified interpretation of SOT, SMR, and SA measurements and offers a practical method to quantitatively evaluate the impact of interlayer engineering on effective spin transparency and measurable spin Hall signals.

4.4.3. Implications for Intrinsic vs. Effective Spin Hall Angle Evaluation

Our comparative analysis of θ_{SH} from SA, SOT, and SMR measurements indicates that θ_{SH}^{SA} is the closest representation of the intrinsic spin Hall angle of BiSb, as it is minimally influenced by interlayer transparency and FM thickness. In contrast, θ_{SH}^{SOT} and θ_{SH}^{SMR} represent effective values that depend on the ability of the FM layer to absorb or reflect spin currents.

This distinction is crucial for both fundamental studies and device applications. For instance, the effective spin Hall angle from SOT measurements is highly relevant for evaluating switching efficiency in SOT-MRAM devices, whereas the intrinsic spin Hall angle from SA measurements provides deeper insight into the spin–orbit physics of the SOT material.

In conclusion, careful consideration of the measurement technique is essential when interpreting θ_{SH} values. The SA method offers the most direct evaluation of intrinsic θ_{SH}, while SOT and SMR provide effective values that are critical for device performance evaluation. Understanding these differences is key to optimizing both the material properties and device designs of BiSb/interlayer/CoFe heterostructures.

4.5. Summary

In this chapter, the temperature dependence of the spin Hall angle in BiSb/interlayer/CoFe heterostructures was systematically examined using three complementary techniques: SA, SOT second harmonic Hall measurement, and SMR.

All three methods revealed a consistent trend: the spin Hall angle increases with decreasing temperature, which is attributed to the enhanced contribution of topological surface states in BiSb at low temperatures. Among the techniques, the SA method consistently produced the largest spin Hall angle values and exhibited the strongest temperature dependence. In contrast, the SOT and SMR methods yielded smaller spin Hall angles with weaker temperature dependence.

These differences are rooted in the distinct physical sensitivities of each method. The SOT and SMR measurements depend on spin-transfer or spin-reflection processes at the interlayer/FM interface and are strongly influenced by the details of spin transport across the interlayer and interface. The SA method, in comparison, detects spin accumulation under a spin-current open-circuit condition, making it less affected by the interfacial transparency and FM thickness.

This comprehensive analysis highlights the importance of selecting the appropriate measurement technique based on the intended purpose, SA for intrinsic property evaluation, SOT for torque efficiency analysis, and SMR for spin reflection behavior.

Building on these findings, the next chapter will summarize the key results of the entire thesis, present overarching conclusions, and discuss future directions for the development of BiSb-based spintronic devices.

4.6. Reference

1 A. Hoffmann, IEEE Trans. Magn. 49, 5172 (2013).

2 J. C. R. Sánchez, L. Vila, G. Desfonds, S. Gambarelli, J. P. Attané, J. M. D. Teresa, C. Magén, and A. Fert, Nat. Commun. 4, 2944 (2013).

3 L. Liu, C.-F. Pai, Y. Li, H. W. Tseng, D. C. Ralph, and R. A. Buhrman, Science 336, 555 (2012).

4 C.-F. Pai, L. Liu, Y. Li, H. W. Tseng, D. C. Ralph, and R. A. Buhrman, Appl. Phys. Lett. 101, 122404 (2012).

5 L. Liu, O. J. Lee, T. J. Gudmundsen, D. C. Ralph, and R. A. Buhrmam, Phys. Rev. Lett. 109, 096602 (2012).

6 S. Fukami, T. Anekawa, C. Zhang, and H. Ohno, Nat. Nanotechnol. 11, 621 (2016).

7 K. Garello, C. O. Avci, I. M. Miron, M. Baumgartner, A. Ghosh, S. Auffret, O. Boulle, G. Gaudin, and P. Gambardella, Appl. Phys. Lett. 105, 212402 (2014).

8 C. Zhang, S. Fukami, H. Sato, F. Matsukura, and H. Ohno, Appl. Phys. Lett. 107, 012401 (2015).

9 A. R. Mellnik et al., Nature 511, 449 (2014).

10 Y. Wang, D. Zhu, Y. Wu, Y. Yang, J. Yu, R. Ramaswamy, R. Mishra, S. Shi, M. Elyasi, and K.-L. Teo, Nat. Commun. 8, 1364 (2017).

11 H. Wu et al., Phys. Rev. Lett. 123, 207205 (2019).

12 P. N. Hai, J. Magn. Soc. Jpn. 44, 137 (2020).

13 N. H. D. Khang, Y. Ueda, and P. N. Hai, Nat. Mater. 17, 808 (2018).

14 H. Wu et al., Nat. Commun. 12, 6251 (2021).

15 Y. Ueda, N. H. D. Khang, K. Yao, and P. N. Hai, Appl. Phys. Lett. 110, 062401 (2017).

16 T. Fan, M. Tobah, T. Shirokura, N. H. D. Khang, and P. N. Hai, Jpn. J. Appl. Phys. 59, 063001 (2020).

17 T. Fan, N. H. D. Khang, T. Shirokura, H. H. Huy, and P. N. Hai, Appl. Phys. Lett. 119, 082403 (2021).

18 T. Fan, N. H. D. Khang, S. Nakano, and P. N. Hai, Sci. Rep. 12, 2998 (2022).

19 N. H. D. Khang, T. Shirokura, T. Fan, M. Takahashi, N. Nakatani, D. Kato, Y. Miyamoto, and P. N. Hai, Appl. Phys. Lett. 120, 152401 (2022).

20 Z. Ruixian et al., Appl. Phys. Lett. 124, 072402 (2024).

21 H. H. Huy et al., Appl. Phys. Lett. 122, 052401 (2023).

22 M. Liu et al., Appl. Phys. Lett. 125, 242401 (2024).

23 Q. Le et al., J. Appl. Phys. 137, 123903 (2025).

24 Q. Le et al., Jpn. J. Appl. Phys. 64, 043001 (2025)

25 M. Hayashi, J. Kim, M. Yamanouchi, and H. Ohno, Phys. Rev. B 89, 144425 (2014).

26 L. Liu, T. Moriyama, D. C. Ralph, and R. A. Buhrman, Phys. Rev. Lett. 106, 036601 (2011).

27 K. Nakagawara, S. Kasai, J. Ryu, S. Mitani, L. Liu, M. Kohda, and J. Nitta, Appl. Phys. Lett. 115, 162403 (2019).

28 Y. Wang, P. Deorani, X. Qiu, J. H. Kwon, and H. Yang, Appl. Phys. Lett. 105, 152412 (2014).

29 M. Isasa, E. Villamor, L. E. Hueso, M. Gradhand, and F. Casanova, Phys. Rev. B 91, 024402 (2015).

30 A. Azevedo, L. H. Vilela-Leão, R. L. Rodríguez-Suárez, A. F. Lacerda Santos, and S. M. Rezende, Phys. Rev. B 83, 144402 (2011).

31 T. Uchida, T. Nonaka, T. Yoshino, T. Kikkawa, D. Kikuchi, and E. Saitoh, Appl. Phys. Express **5**, 093001 (2012).

32 M. Weiler, M. Althammer, F. D. Czeschka, H. Huebl, M. S. Wagner, M. Opel, R. Gross, and S. T. B. Goennenwein, Phys. Rev. Lett. 108, 106602 (2012).

33 B. F. Miao, S. Y. Huang, D. Qu, and C. L. Chien, Phys. Rev. Lett. 111, 066602 (2013).

34 C. M. Jaworski, J. Yang, S. Mack, D. D. Awschalom, J. P. Heremans, and R. C. Myers, Nat. Mater. 9, 898 (2010).

35 Q. Le et al., US Patent No 11875827 (2022).

36 H. Nakayama et al., Phys. Rev. Lett. 110, 206601 (2013).

37 Y.-T. Chen, S. Takahashi, H. Nakayama, M. Althammer, S. T. B. Goennenwein, E. Saitoh, and G. E. W. Bauer, Phys. Rev. B 87, 144411 (2013).

38 J. Kim, P. Sheng, S. Takahashi, S. Mitani, and M. Hayashi, Phys. Rev. Lett. 116, 097201 (2016).

39 J. Sasaki et al., IEEE Trans. Magn. 58, 3200404/1 (2022).

40 C. O. Avci, K. Garello, A. Ghosh, M. Gabureac, S. F. Alvarado, and P. Gambardella, Nat. Phys. 11, 570 (2015).

41 D. Hou et al., Appl. Phys. Lett. 101, 042403 (2012).

42 J. Liu, T. Ohkubo, S. Mitani, K. Hono, and M. Hayashi, Appl. Phys. Lett. 107, 232408 (2015).

43 Y. T. Chen, S. U. Jen, Y. D. Yao, J. M. Wu, G. H. Hwang, T. L. Tsai, Y. C. Chang, and A. C. Sun, J. Magn. Magn. Mater. 304, e71 (2006).

44 K. Ueda et al., Appl. Phys. Lett. 100, 202407 (2012).

45 M. Zhu, C. L. Dennis, and R. D. McMichael, Phys. Rev. B 81, 140407(R) (2010).

46 T. Shirokura and P. N. Hai, Appl. Phys. Lett. 122, 232404 (2023).

47 S. Zhang and A. Fert, Phys. Rev. B 94, 184423 (2016).

48 H. Isshiki, P. Muduli, J. Kim, K. Kondou, and Y. Otani, Phys. Rev. B 102, 184411 (2020).

49 H. He et al., Phys. Rev. B 104, L220407 (2021)

50 J.-C. Rojas-Sánchez, N. Reyren, P. Laczkowski, W. Savero, J.-P. Attané, C. Deranlot, M. Jamet, J.-M. George, L. Vila, H. Jaffrès, Phys. Rev. Lett. **112**, 106602 (2014).

51 Althammer et al., Phys. Rev. B 87, 224401 (2013).

52 Cheng, J. Xiao, Q. Niu, and A. Brataas, Phys. Rev. B 87, 224401 (2013).

53 K.-W. Kim, Phys. Rev. B 99, 224415 (2019).

54 L. Zhu, D. C. Ralph, and R. A. Buhrman, Phys. Rev. Lett. 123, 057203 (2019).

55 T. Ando, Sci. Technol. Adv. Mater. 15, 013201 (2014).

56 Y. Tserkovnyak, A. Brataas, and G. E. W. Bauer, Phys. Rev. Lett. 88, 117601 (2002).

57 E. Saitoh, M. Ueda, H. Miyajima, and G. Tatara, Appl. Phys. Lett. 88, 182509 (2006).

58 J. Xiao, G. E. W. Bauer, K. Uchida, E. Saitoh, and S. Maekawa, Phys. Rev. B 81, 214418 (2010).

59 K. Kondou, H. Sukegawa, S. Mitani, K. Tsukagoshi, and S. Kasai, Appl. Phys. Express 5, 073002 (2012).

60 M. Obstbaum, M. Härtinger, H. G. Bauer, T. Meier, F. Swientek, C. H. Back, and G. Woltersdorf, Phys. Rev. B 89, 060407 (2014).

Chapter 5 Summary, Conclusions, and Outlook

We have presented a comprehensive investigation of spin–orbit phenomena in BiSb/interlayer/CoFe heterostructures, covering the research motivation, objectives, experimental methodology, and results from both room-temperature and temperature-dependent studies.

Chapter 1 outlined the research background, fundamental of spintronic phenomena, material platforms, applications, and the research objectives.

Chapter 2 described the experimental setup and device fabrication methods used in this study.

Chapter 3 demonstrated exceptionally large room-temperature output signals in BiSb-based DSH magnetic field sensing devices and discussed their application potential in high-density HDD read heads.

Chapter 4 systematically analyzed the temperature dependence of the spin Hall angles using multiple measurement techniques, clarifying the relationship between intrinsic and effective values.

Building on these findings, this chapter summarizes the key results of the thesis, draws overarching conclusions, and discusses future directions for research and application.

5.1. Summary

This thesis presented a systematic study of spin–orbit phenomena in BiSb/interlayer/CoFe heterostructures.

In Chapter 1, the motivation and objectives for this work were established by reviewing the demand for the next-generation HDD read heads with focus on magnetic field sensors using the spin Hall effect and inverse spin Hall effect. BiSb, with its giant spin Hall angle, was identified as a promising candidate for both fundamental research and practical applications of SOT magnetic field sensors.

In Chapter 2, the fabrication techniques and measurement systems essential for this study were developed. These included thin film growth, microfabrication of DSH magnetic field sensors and Hall bar devices, and the establishment of harmonic Hall, spin accumulation, and SMR measurement platforms. This infrastructure was critical for precise evaluation of spin Hall angle and device performance.

In Chapter 3, room-temperature experiments revealed exceptionally large output signals in BiSb/interlayer/CoFe DSH magnetic field sensing devices—tens of times larger than that expected from the second harmonic Hall signals and over two orders of magnitude greater than those in Pt, W, or Ta. Detailed noise analysis identified dominant sources and suggested optimization strategies to further enhance directivity. These results demonstrate the strong potential of BiSb devices for next-generation HDD read heads and magnetic field sensors.

In Chapter 4, the temperature dependence of the spin Hall angles was studied using three complementary techniques: SA, SOT, and SMR. All methods showed an increase in θ_{SH} at lower temperatures, consistent with enhanced contributions from topological surface states. SA consistently yielded the largest θ_{SH} values and strongest temperature dependence, while SOT and SMR provided smaller values with weaker temperature dependence. These differences were attributed to each method's physical sensitivity - SA being closer to the intrinsic θ_{SH}, while SOT and SMR reflect effective values relevant for device-level performance.

5.2. Conclusions

DSH magnetic field sensing devices consisting of BiSb/interlayer/CoFe in chapter 3 exhibit exceptionally large output at 300 K, exceeding heavy metals by more than two orders of magnitude. The magnitude of these signals is promising for next-generation HDD read heads. Device optimization, particularly in noise reduction, can further improve detectivity and operational stability.

From the temperature-dependent studies in Chapter 4, we found that the intrinsic θ_{SH} of BiSb increases significantly as temperature decreases, in line with enhanced surface-state contributions. SA provides a reliable estimate of intrinsic θ_{SH}, whereas SOT and SMR yield effective values determined by the interface spin transparency, spin absorption and spin reflection. The differences among techniques underline the importance of method selection: SA for intrinsic property characterization, SOT and SMR for device performance evaluation.

Overall, BiSb is confirmed as a high-performance spin-orbit material, combining large spin Hall resistance at room temperature with tunable θ_{SH} over a wide temperature range. These properties position BiSb as a strong candidate for both fundamental research and spintronic applications requiring high spin-orbit torque efficiency and sensitive magnetic field detection.

5.3. Outlook

The findings of this work open several promising directions for future research and device development:

(1) Interface Engineering

Enhance interlayer spin transparency by optimizing composition, thickness, and crystalline quality. Reduce spin loss at the BiSb/interlayer and interlayer/CoFe interfaces to maximize effective θ_{SH}.

(2) Application in Next-Generation HDD Read Heads

Integrate BiSb-based spin Hall devices into HDD reader prototypes to evaluate performance under operational conditions. Address fabrication scaling and compatibility with existing HDD manufacturing processes.

(3) Exploration of Alternative Topological Materials

Expand to other topological semimetals with better thermal stability. Design heterostructures combining BiSb with other spin-orbit materials to tailor spin transparency and torque generation.

Closing Remark

The results presented in this thesis advance the application of BiSb-based heterostructures to practical spintronic applications, in particular HDD reader. By bridging fundamental physics and application-oriented device studies, this work establishes a foundation for the development of next-generation high-density HDD read heads. The methodologies and insights developed here are expected to inspire further innovations in both materials research and device engineering, ultimately contributing to high-performance, energy-efficient HDD technologies.

Publications

- **Journal Papers**

[1] **Min Liu**, Zhang Ruixian, Quang Le, Brian York, Cherngye Hwang, Xiaoyong Liu, Michael Gribelyuk, Xiaoyu Xu, Son Le, Maki Maeda, Tuo Fan, Yu Tao, Hisashi Takano, and Pham Nam Hai, “Spin Hall magnetic field sensing device using topological insulator”, Appl. Phys. Lett. 125, 242401 (2024).

[2] Quang Le, Brian R. York, Cherngye Hwang, Xiaoyong Liu, Michael A. Gribelyuk, Son Le, Lei Xu, Jason James, Jose Ortega, Maki Maeda, Tuo Fan, Hisashi Takano, **Min Liu**, Zhang Ruixian, Shota Namba, Pham Nam Hai., "Transport and material properties of doped BiSbX topological insulator films grown by physical vapor deposition", Jpn. J. Appl. Phys., 63, 123001 (2024).

[3] **Min Liu**, Zhang Ruixian, Quang Le, Brian York, Cherngye Hwang, Xiaoyong Liu, Michael Gribelyuk, Xiaoyu Xu, Son Le, Maki Maeda, Tuo Fan, Yu Tao, Hisashi Takano, and Pham Nam Hai, "Comparison of spin Hall angles measured by spin accumulation, spin-orbit torque, and spin Hall magnetoresistance", Jpn. J. Appl. Phys., 64, 103001 (2025).

[4] Quang Le, Brian R. York, Cherngye Hwang, Xiaoyong Liu, Lei Xu, Son Le, Maki Maeda, Tuo Fan, Yu Tao, Hisashi Takano, **Min Liu**, Zhang Ruixian, Shota Namba, Pham Nam Hai, "Thermal reliability and spin Hall angle of highly textured and epitaxial Bi0.9Sb0.1(012) topological insulator", Jpn. J. Appl. Phys., 64, 043001 (2025).

[5] Quang Le, Xiaoyong Liu, Lei Xu, Brian R. York, Cherngye Hwang, Son Le, Maki Maeda, Tuo Fan, Yu Tao, Hisashi Takano, **Min Liu**, Zhang Ruixian, Shota Namba, Pham Nam Hai., "Effects of metal, oxide, and hybrid metal-oxide interlayers on spin–orbit torque in BiSb topological insulator and magnetic interfaces", Jpn. J. Appl. Phys.,137, 123903 (2025).

International Conferences

[6] **Min Liu**, Zhang Ruixian, Quang Le, Brian York, Cherngye Hwang, Xiaoyong Liu, Michael Gribelyuk, Xiaoyu Xu, Son Le, Maki Maeda, Tuo Fan, Yu Tao, Hisashi Takano, and Nam Hai Pham, IcAUMS 2025, Apr. 2025.

[7] Zhang Ruixian, Quang Le, XiaoYong Liu, Lei Xu, Brian R.York, Cherngye Hwang, Son Le, Maki Maeda, Tuo Fan, Yu Tao, Hisashi Takano, **Min Liu**, Shota Namba, Pham Nam Hai. The Magnetic Recording Conference (TMRC 2025). Poster presentation. Aug. 29, 2025.

Domestic Conferences

[8] **Min Liu**, Zhang Ruixian, Quang Le, Brian York, Cherngye Hwang, Xiaoyong Liu, Michael Gribelyuk, Xiaoyu Xu, Son Le, Maki Maeda, Tuo Fan, Yu Tao, Hisashi Takano, and Nam Hai Pham, The 72nd JSAP Spring Meeting 2025, Mar. 14, 2025.

[9] Zhang Ruixian, Quang Le, Xiaoyong Liu, Lei Xu, Brian R. York, Cherngye Hwang, Son Le, Maki Maeda, Fan Tuo, Hisashi Takano, **Min Liu**, Shota Namba, Pham Nam Hai. The 72nd JSAP Spring meeting 2025. Oral presentation. Mar. 2025.

Acknowledgments

I would like to express my deepest gratitude to my supervisor, Professor Pham. Throughout my doctoral journey, he has been not only an exceptional academic advisor but also a supportive mentor whose presence brought great reassurance to my life abroad. From my very first day in the laboratory—when he personally showed me around the campus and the unfamiliar surroundings—his kindness made me feel welcomed and grounded in a new environment. Professor Pham's patient guidance helped me overcome countless experimental challenges, and his thoughtful discussions inspired me to pursue my research with confidence and curiosity. What I appreciate most is that I always felt at ease speaking with him, whether about research questions or everyday matters. This sense of comfort and trust made my years of study far less solitary, and I am truly grateful to have had a mentor with whom I could openly share ideas, concerns, and small moments of progress. His encouragement, understanding, and steady support have shaped not only the outcomes of my research but also my personal growth. I feel genuinely fortunate to have learned from a mentor who offered both guidance and warmth, making my doctoral experience deeply meaningful and memorable.

I would also like to express my sincere gratitude to Dr. Takanori Shirakura, Dr. Ho Hoang Huy, and Ruixian Zhang for their warm support when I first joined the laboratory. They helped me quickly become familiar with the laboratory environment, patiently taught me how to operate various equipment, and generously supported me in daily life. They were not only senior colleagues but also friends whose kindness and guidance enabled me to acquire essential experimental skills, collaborate effectively, and adapt smoothly to a new environment. Their support greatly benefited both my research and personal growth.

I am equally grateful to my fellow laboratory members, who shared not only experiments but also countless moments of daily life with me. We were not just colleagues working on the same research projects—we were also friends who supported and encouraged one another throughout these years. Their companionship made my research life much more enjoyable and memorable.

I am also deeply grateful to Tetsuya Iwanaga, who brought warmth and color to my life abroad and offered steady companionship and encouragement during difficult times. From him, I learned how to better interact with people, and he also helped me improve my language skills. I would like to thank Tuo

Fan for his generous help and guidance, which showed me great kindness and support. My heartfelt thanks also go to Sho Kagami and Pham Van Thuan, who were not only my laboratory partners but also my close friends in Japan. We shared the challenges of research as well as many joyful moments outside the lab.

I am grateful as well to Tongshuang Huang, my dear friend whose support and understanding made my daily life much easier. I am truly thankful for his kindness and for always being there when I needed help. I would also like to thank Rei Nishiyama and Kota Sato for their support in everyday matters, which brought warmth and convenience to my life in Japan.

I would also like to express my sincere appreciation to Western Digital and to Quang Le, Brian York, Cherngye Hwang, Xiaoyong Liu, Michael Gribelyuk, Xiaoyu Xu, Son Le, Maki Maeda, Yu Tao, and Hisashi Takano for their generous collaboration and support. Their assistance greatly facilitated my research and played a crucial role in the successful completion of this project.

I would like to give special thanks to Zhang Siyue, whose quiet support and steady encouragement were always there whenever I made important decisions, and who was always behind me, walking with me along the way.

Finally, I would like to express my heartfelt gratitude to my family for their unconditional support and for always being my strongest backing. They have given me the greatest freedom to explore the world and to pursue whatever I am passionate about—even when they have absolutely no idea what I am doing. Their trust and non-interference have been my greatest source of strength, allowing me to follow my dreams without hesitation and devote myself wholeheartedly to my studies and research.